Thin Films of Porphyrin-Based Metal-Organic Frameworks

Grown by Liquid-Phase Epitaxy

Zur Erlangung des akademischen Grades eines

DOKTORS DER NATURWISSENSCHAFTEN

(Dr. rer. nat.)

der KIT-Fakultät für Chemie und Biowissenschaften

des Karlsruher Instituts für Technologie (KIT)

genehmigte

DISSERTATION

von

M. Eng. Wencai Zhou

aus

Jining, Shandong, P.R.China

KIT-Dekan: Prof. Dr. Willem Klopper

Referent: Prof. Dr. Christof Wöll

Korreferent: Prof. Dr. Stefan Bräse

Tag der mündlichen Prüfung: 22.07.2016

I hereby declare that this dissertation has been elaborated by me other than the sources, references and resources mentioned in the thesis. I have properly cited all the text and figures that are not my own in the thesis. I present this work with the best of my knowledge and to fulfill the requisites of the Karlsruhe Institute of Technology to ensure good scientific practices.

Karlsruhe 06. 06. 2016

Wencai Zhou

Contents

Abstract

Among the well-established metal-organic framework (MOF) thin film fabrication approaches, the liquid-phase epitaxy (LPE) method has showed great advantage of growing crystalline and highly oriented MOF thin films on functionalized solid substrates. The corresponding MOF thin films, with controllable thickness, are referred to as surface-mounted MOFs (SURMOFs). Porphyrin-based compounds have been successfully utilized across wide applications, such as dye-sensitized solar cells and photodynamic therapy, due to their central role in metabolic processes in living organism. Therefore, this thesis is focused on the growth of different kinds of porphyrin-based SURMOFs on various substrates, post-synthetic modification (PSM) of the porphyrin SURMOF and their applications.

The successful growth of several porphyrin-based SURMOFs is demonstrated and the XRD results show that the SURMOFs are highly crystalline and oriented on various substrates. This ordered structure enables the electronic structure calculation. The calculation results show that an ordered array of porphyrins in this manner forms a small dispersion of occupied and unoccupied bands leading to the formation of a small indirect band gap. The measurement results also show that the porphyrin-SURMOFs exhibit lager charge-carrier mobility and an unusually large charge-carrier generation efficiency. By assembling this porphyrin-SURMOF into photovoltaic device using fluorine-doped tin oxide (FTO) substrate as bottom electrode and I^-/I_3^- electrolyte as top electrode, a remarkable efficiency was achieved.

With regard to the practical application, the first porphyrin-MOF device need to be improved since the I^-/I_3^- liquid used as the top electrode is highly corrosive and not well suited for large scale fabrication process. In this study, a new type of porphyrin-SURMOF using a modified porphyrin linker with two diphenylamine (DPA) groups was designed and successfully synthesized. The prepared porphyrin SURMOFs were assembled to all solid state photovoltaic device using conductive polymer as top electrode, which is the first example of MOF-based solid photovoltaic device.

In order to improve the electron transport in the porphyrin-based MOF structure, an electron donor-acceptor (D-A) system was designed by loading C_{60}-fullerene into the pores of the MOF framework, where porphyrin served as electron donor and fullerene was electron acceptor. The

successful loading of C_{60}-fullerene was verified by XRD and UV-Vis measurements. After the introduction of the electron acceptor into the porphyrin SURMOF, the photocurrent was significantly enhanced.

An azido-functionalized porphyrin SURMOF was synthesized with highly crystallinity as well. The functional azide groups in the framework allow for further post-synthetic modifications (PSM) using the strain-promoted azido-alkyne cycloaddition (SPAAC) click chemistry. A conversion yield of 75% was achieved, remaining the crystalline structure after reaction. Further experiments were carried out to synthesize porphyrin surface-grafted gels (SURGELs) via cross-linking of the azido-porphyrin linkers in SURMOFs and alkyne cross-linker, followed by the removal of metal ions. The obtained porphyrin SURGELs, without cytotoxic metal ions but exhibit pronounced stability against water, have potential applications in biology and offer the opportunity to introduce other functional groups to the pores of the gels.

Mass transfer of guest molecules in nanoporous host materials, particularly in MOFs, is a crucial parameter governing the performance of their applications, for example, in molecules separation. In this thesis, the diffusion of ferrocene in vapor and in ethanolic and hexanic solution in HKUST-1 was investigated using SURMOF in combination with a quartz crystal microbalance (QCM). For the first time, liquid- and gas -phase diffusion in MOFs was compared directly in the identical sample.

Zusammenfassung

Unter den etablierten Herstellungsansätzen für dünne Schichten metallorganischer Gerüstverbindungen (*metal-organic frameworks* - MOFs) haben Flüssigphasen-Epitaxie(LPE)-Verfahren besonders großes Potenzial. Diese MOF-Dünnschichten mit kontrollierbarer Dicke werden als oberflächen-verankerte MOFs (SURMOFs) bezeichnet. Porphyrin-basierte Verbindungen haben verschiedenartige Anwendungen, als farbstoffsensibilisierte Solarzellen oder in der photodynamischen Therapie aufgrund ihrer zentralen Rolle in Stoffwechselprozessen im lebenden Organismus. Daher fokussiert diese Arbeit auf das Wachstum verschiedener Porphyrin-basierter SURMOFs auf verschiedenen Substraten, deren postsynthetische Modifikation (PSM) des Porphyrin-SURMOF und deren Anwendungen.

Das Wachstum von unterschiedlichen Porphyrin-basierten SURMOFs wird gezeigt. Die XRD-Ergebnisse zeigen, dass die SURMOFs hochkristallin und orientiert auf verschiedenen Substraten wachsen. Diese geordnete Struktur ermöglicht die Berechnung der elektronischen Struktur. Die Berechnungsergebnisse zeigen, dass die besetzten und unbesetzten Bänder eine geringe Dispersion mit einer kleinen indirekten Bandlücke haben. Die Messergebnisse zeigen auch, dass das Porphyrin-SURMOFs große Ladungsträgermobilitäten und ungewöhnlich große Ladungsträgererzeugungseffizienzen zeigen. Durch den Aufbau dieses Porphyrin-SURMOF in photovoltaischen Vorrichtungen auf FTO-Substraten (*Fluorine-doped Tin Oxide*) als untere Elektrode und I^-/I_3^--Elektrolyt als obere Elektrode wurde eine bemerkenswerte Effizienz für diese neue Klasse von Materialien erreicht.

Im Hinblick auf die praktische Anwendung muss der Aufbau des Porphyrin-MOF-Systems verbessert werden, da die verwendete I^-/I_3^--Flüssigkeit stark korrosiv und nicht für großtechnische Herstellungsverfahren geeignet ist. In dieser Arbeit wurden modifizierte Porphyrin-Linker mit zwei Diphenylamin-Gruppen (DPA) genutzt. Die hergestellten Porphyrin-SURMOFs wurden zu einem festen Photovoltaik-System mit leitfähigem Polymer als obere Elektrode zusammengebaut, was das erste Beispiel für MOF-basierte Festkörper-Photovoltaik-Anlagen ist.

Um die Effizienz zu verbessern, wurden die MOF-Poren mit C_{60}-Fulleren beladen. Somit dient Porphyrin als Elektronendonor und Fulleren als Elektronenakzeptor. Dadurch wurde der

Elektronentransport in der Porphyrin-basierten MOF-Struktur verbessert und ein Elektronen-Donor-Akzeptor (D-A)-System entwickelt. Die erfolgreiche Beladung mit Fulleren wurde durch XRD und UV-Vis-Messung nachgewiesen. Nach der Implementierung des Elektronenakzeptors in den Porphyrin-SURMOF wurde der Photostrom deutlich erhöht.

Hochkristalline Azid-funktionalisierte Porphyrin-SURMOFs wurden synthetisiert. Die funktionellen Azidgruppen ermöglichen weitere post-synthetische Modifikationen mittels *strain-promoted azido-alkyne cycloaddition* (SPAAC) „Klick"-Chemie. Dabei wurden Ausbeuten von 75% ohne Zerstörung der kristallinen Struktur nach der Reaktion erreicht. Weitere Experimente wurden durchgeführt, um die Porphyrin-SURMOFs in oberflächenverankerte Porphyrin-Gele (Porphyrin-SURGELs) umzuwandeln. Diese Gel-Filme haben keine zytotoxischen Metallionen und sind stabil gegenüber Wasser. Sie haben potenzielle Anwendungen in der Biologie und bieten die Möglichkeit, andere funktionelle Gruppen in die Poren der Gele einzulagern.

Der Stofftransport der Gastmoleküle in nanoporösen Materialien ist ein entscheidender Parameter, insbesondere für MOFs, der zum Beispiel für die Effizienz der Stofftrennung äußerst wichtig ist. In dieser Arbeit wurde die Diffusion von Ferrocen in HKUST-1 SURMOFs mittels einer Quarzkristallmikrowaage (QCM) untersucht. Dabei wurde die Diffusion des Ferrocens in verschiedenen Phasen verglichen, d.h. die Diffusion des Ferrocens als Dampf in Argon beziehungsweise die Diffusion des Ferrocenes in ethanolischer oder hexanischer Lösung wurde untersucht. Dies ist die erste Arbeit, wo Flüssigphasen- und Gasphasendiffusion eines Moleküls in einer MOF-Struktur direkt miteinander verglichen wurde.

1 Introduction

1.1 Metal-Organic Frameworks (MOFs)

Metal-Organic Frameworks (MOFs), also known as porous coordination polymers (PCPs), are a class of crystalline materials self-assembled from organic linkers and inorganic connectors of metal ions or clusters (Figure 1.1).[1-3] Although the first coordination polymers can be dated back to 1959,[4] the first MOFs constructed by organic molecular building blocks and metal ions appeared in 1990.[5] Since then, more than 20,000 MOF structures have been reported with a variety of constituents' geometry, size and functionality.[6]
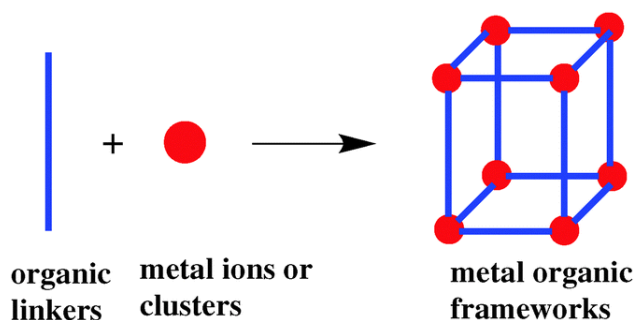
Figure 1.1 Schematic graph of MOF structure constructed by the metal nodes and organic linkers.(Taken from Ref.[7])

MOFs are constructed by joining metal-containing units with organic linkers through coordination bonds. When the organic linkers are linked to the metal-containing units, the architecturally robust crystalline MOF structures are formed. The extraordinary degree of variance in both the inorganic and organic components of their structures makes MOFs a highly flexible class of materials in terms of pore size and chemical properties compared with traditional porous materials, such as zeolites, active carbons and mesoporous silicon. The surface areas of the MOFs can range from 1000 to 10,000 m^2 g^{-1} and the density can be as low as 0.13 g cm^{-3}. Typically, the MOFs have the porosity greater than 50% of the crystal volume and the largest pore aperture is 98 Å.[6] Due to high surface area, high porosity and the tunable structure as well as functionality, MOFs have attracted considerable attention in many areas, including gas storage,[8,9] gas separation,[10-12] sensing,[13] catalysis[14-16] and drug delivery.[17]

1.1.1 Design of MOFs

In principle, MOFs can be designed with controlled pore size, structure, and functionality for specific applications by judiciously selecting the metal unit and the organic linker.[3] Generally, metal clusters which result from the initial bonding of the metal ions and the bridging ligands serve as secondary building units (SBUs), which are crucial to the design of MOFs and to the topology of the robust frameworks.[18] Yaghi et al have made a summary of metal-cluster-based SBUs, where 131 geometries along with the corresponding connectivity are described.[18] Four typical metal-cluster-based SBUs are listed in Figure 1.2, which are represented as trigonal, square planar, tetrahedral and tetragonal paddlewheel arrangements, respectively.
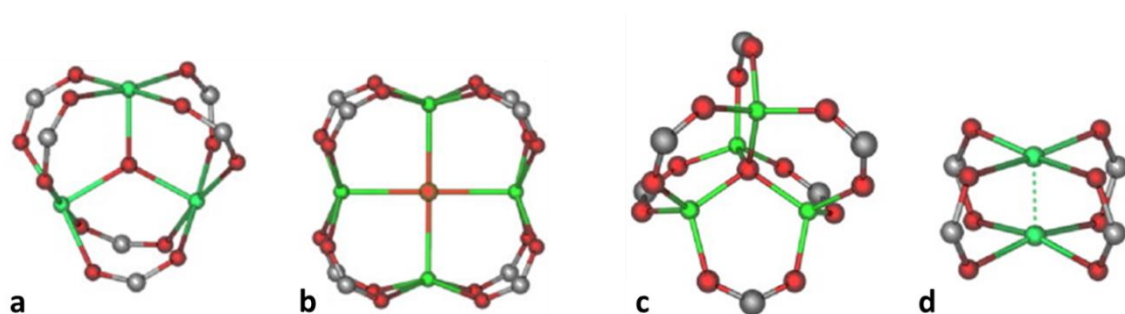
Figure 1.2 Structural representations of several SBUs. (a) trigonal planar, (b) square planar, (c) tetrahedral, and (d) tetragonal paddlewheel. (Taken from Ref.[19])

The SBUs are not isolated entities. They are formed by bridging the metal ions with the coordinating atoms of the ligands, resulting in the different geometrical orientations of the linkers.[19] The organic linkers, including ditopic or polytopic organic carboxylates or other organic anions, such as phosphonate, sulfonate, and heterocyclic compounds,[3] play an important role in controlling the orientation of the structure for a given metal ion. On the other hand, the structure of the organic SBUs seldom changes during MOF assembly. Once metal-cluster based SBUs are formed, the chemical properties of highly ordered frameworks with rigid organic linkers can be predicted.

Overall, the combination of both metal-based and organic SBUs determines the final topology of framework. However, it is difficult to achieve a well-predicted design of MOFs due to the influence of temperature, solvent, and the composition or concentration of the reactants, especially in the more complicated cases, like polytopic linkers. Nevertheless, the careful

selection of the inorganic and organic components could tune the topology and functionality for different applications. Some representative MOFs, either well characterized or widely studied because of their specific properties, are depicted in Figure 1.3. MOF-5 ($Zn_4O(BDC)_3$, BDC = 1,4-benzenedicarboxylate) has uniform microporous structure and good thermal stability.[20] HKUST-1 (HKUST = Hong Kong University of Science and Technology), firstly synthesized in 1999,[21] is one of the most widely studied MOFs due to it is easily synthesized. ZIF-8 (ZIF = zeolitic imidazolate framework) exhibits high stability against water[22] and MIL-53 (MIL = Matérial Institut Lavoisier) is featured by the breathe behavior.[23] UiO-66 (UiO = Universitetet i Oslo) retains its properties under a relative wide range of chemical and physical conditions.[24]
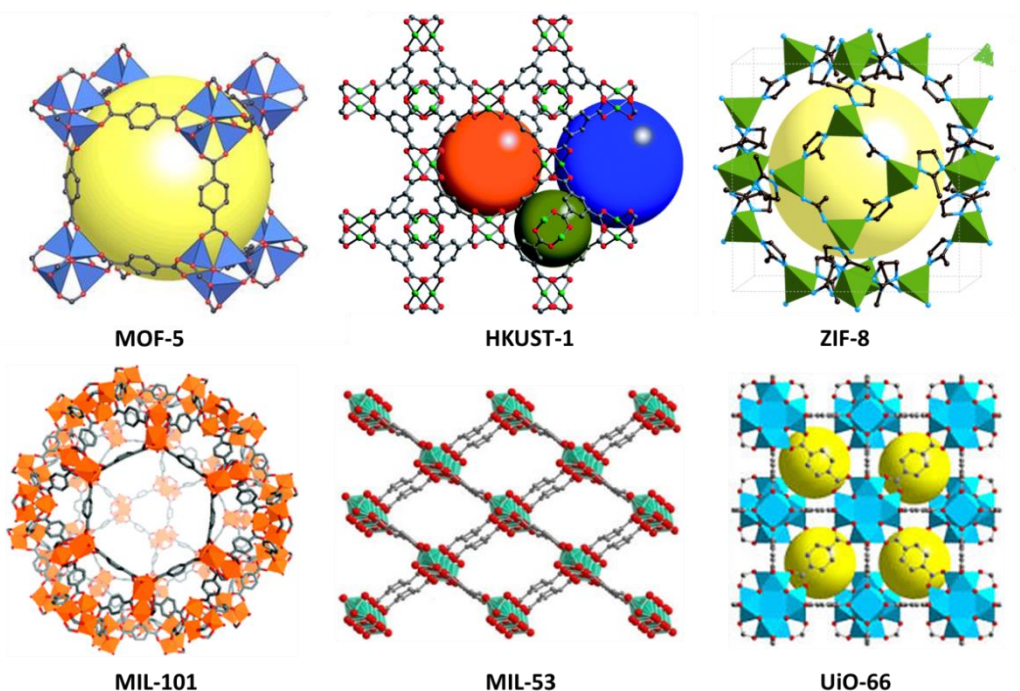
Figure 1.3 Representative MOFs (Taken from Ref.[16,25-28])

1.1.2 Synthesis of MOFs

Numerous methods or techniques for the synthesis of MOF materials have been developed for the last two decades, which are described in the following.

1.1.2.1 Conventional solvothermal synthesis

The most conventional method used to prepare MOFs is solvothermal synthesis, in which the metal salts and the linkers, sometimes accompanying with a templating agent, are dissolved in an

organic solvent or water and then placed in an autoclave or a tube to be stored at a certain temperature for several hours or days, allowing the formation of bulk MOFs.[29-31]

Although the solvothermal method is commonly used, it is limited by the long reaction time, low quantities and the cost of the involved solvents.[32] Therefore, new approaches were developed to overcome the disadvantages.

1.1.2.2 Microwave-assisted synthesis

To accelerate the organic chemical reaction, microwave-assisted method was proposed in 1986.[33,34] Since then, high-speed synthesis via the microwave irradiation has attracted considerable attention.[35,36] The rate acceleration is due to the efficient heating of materials by "microwave dielectric heating" effects, i.e. the material can absorb microwave energy and then convert it into heat.

The first microwave-assisted synthesis was established to synthesize three known MOFs, namely IRMOF-1, IRMOF-2, and IRMOF-3, by Ni and Masel.[37] The mixture of the metal precursor and the corresponding organic linker was dissolved in N, N′-diethylformamide (DEF) and then the solution mixture was heated by a microwave synthesizer for a few seconds to form the desired MOFs. This technique allows the formation of high quality uniform crystals in one minute.

1.1.2.3 Mechanochemical synthesis

Although the microwave-assisted synthesis could efficiently accelerate the formation of MOFs, it may lead to the formation of by-products and environmental contamination due to its lingering presence in the solvents. To avoid this drawback, a non-solvent approach, named mechanochemical synthesis, was proposed in 2006 by Pichon et al.[38] The metal salts or oxides are ground together with the bridging organic ligands. During the grinding, the metal ions react rapidly with the organic ligands, giving a quantitative yield of the desired MOF. Friščić and Fábián found that the addition of a small amount of solvents to the reaction mixture of ZnO and fumaric acid during the mechanochemical approach, could enable the rapid conversion of the metal oxide precursor into a variety of metal-organic architectures. The improved approach is referred to as liquid-assisted grinding (LAG). The LAG approach not only neutralizes the reactants acid-base reactants, but also drives the coordination self-assembly.[39]

1.1.2.4 Electrochemical synthesis

The first example of the electrochemical synthesis of HKUST-1 was reported by the researchers in BASF,[40] since then, the synthesis route has been expanded to other MOFs.[41,42] In this method, the metal source, which serves as the electrode, is placed in the linker solution containing the electrolyte. When an appropriate voltage or current is applied, the metal source dissolves and releases the metal ions near the surface of the electrode. Then the metal ions react with the organic linkers in the solution and the MOF is generated near the electrode surface.[43] It was found that the applied voltage, current density, solvent, electrolyte, and temperature have an impact on the quality of the resulting MOFs.[41,44-48]

Compared with other methods, the electrochemical synthesis method exhibits several advantages, like shorter synthesis time and milder synthesis conditions, giving the chance to directly control the reaction conditions during the process and allowing the formation of the MOF films without surface pretreatment.[43]

Besides the afore-mentioned processes, sonochemical synthesis,[49] catenation control,[32] post-modification synthesis[50] and liquid-phase epitaxy (LPE) process[51,52] have also been developed to synthesize MOFs. Among these processes, the LPE method plays an important role in preparing MOF films, which will be described in detail in the latter chapter.

1.1.3 Applications of MOFs

Compared with other traditional porous materials, MOFs exhibit remarkable properties, such as high porosity, high specific surface area, relatively high thermal and chemical stability and versatile chemistry. These remarkable properties enable MOFs to have potential applications in many aspects.

1.1.3.1 Gas storage

One of the most promising and widely studied applications of MOFs is gas adsorption due to their tunable pore geometries and flexible frameworks, especially the adsorption of hydrogen, methane and CO_2.

Rosi et al. first reported the adsorption of hydrogen by MOF-5 in 2003, which was able to adsorb up to 4.5 wt% of hydrogen at 78 K and 1 wt% under ambient conditions at a pressure of 20 bar.[53] Subsequently, hydrogen storage capacity of other MOFs, such as MILs,[54] ZIFs,[55]

5

DUTs,[56] NOTTs,[57] PCNs[58] and SNUs,[59] has been extensively investigated. The introduction of open metal sites and high surface area has remarkably enhanced the hydrogen uptake in MOFs, as exemplified by $Zn_3(BDC)_3[Cu(Pyen)]$ ($PyenH_2$ = 5-methyl-4-oxo-1,4-dihydro-pyridine-3-carbaldehyde)[60] and NU-100.[61]

Concerning the adsorption of methane in MOFs, it was firstly reported by Kitagawa et al. in 1997 that a coordination polymer compound ($Co_2(4,4'-bpy)_3(NO_3)_4$ $4H_2O$) was found acting as a potential material to effectively adsorb methane. It exhibited an uptake capacity of 52 cm^3 (STP) g^{-1} at 298 K and 30 bar.[62] Yaghi's group reported the methane storage capacities of a series of isoreticular MOFs in 2002,[27] where IRMOF-6 and IRMOF-1 (MOF-5) exhibited a methane uptake of 240 cm^3(STP) g^{-1} and 228 cm^3(STP) g^{-1}, respectively, at 298 K and ~36 bar. Since then, high methane storage capacities in dozens of MOFs have been exploited by various groups.

MOFs are also promising for the capture of CO_2, the major cause of greenhouse effect, from the atmosphere and combustion gases. Amounts of studies have ascertained the high affinity of some porous MOFs towards CO_2, such as MOF-200 (53.4 m mol) g^{-1} at 50 bar and 298K)[63] and MIL-101 (40.0 m mol) g^{-1} at 5 MPa and 303 K).[64]

1.1.3.2 Catalysis
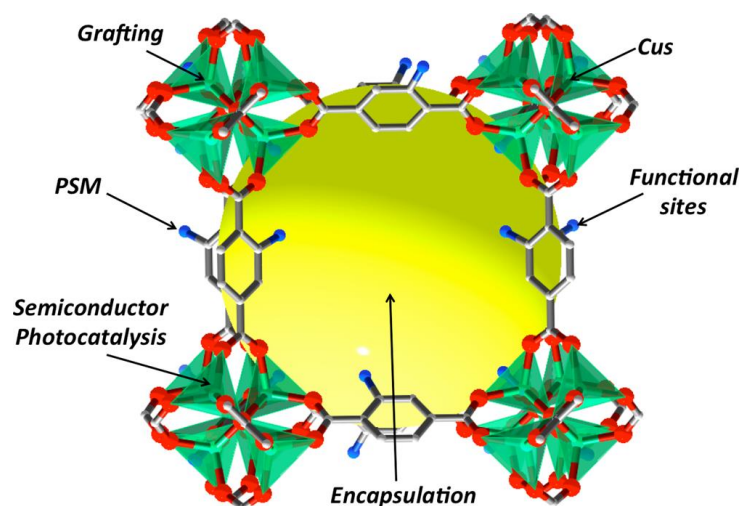
Figure1.4 Different strategies for the inclusion of catalytic moieties into a MOF scaffold (Taken from Ref.[65])

MOFs may play a decisive role in catalysis through several approaches, summarized in Figure 1.4. The catalysis function can arise from the unsaturated metal sites or functional organic sites, which can be implemented by direct synthesis or post-synthetic modification (PSM). Alternatively, the pores or channels of MOFs can afford the potential to encapsulate catalytic species (e.g., metal or metal oxide nanoparticle, metal coordination complexes or other discrete molecular species) [65,66]

Highly robust UiO-66-CAT MOF with coordinatively unsaturated active metal centers, which is formed by incorporating catechol species into the robust UiO-66 framework, can be modified as a catalyst by postsynthetic deprotection (PSD) and postsyntheticexchange (PSE).[67] The catalytic performance of Cr-metalated UiO-66 MOF was investigated for the oxidation of alcohols to ketones using a wide range of substrates. The results indicated that the catalysis could be achieved with very low metal loadings (0.5-1 mol%). Unlike zeolite-supported, Cr-exchange oxidation catalysts, the MOF-based catalysts could be reused over five catalytic runs without any significant loss in the catalytic activity.

1.1.3.3 Sensors

By incorporating appropriate signal-transduction capabilities, MOFs can be used as sensors by monitoring the optical, electrochemical and mechanical signals to realize selective detection of solvent molecules, metal ions, DNA, proteins, and other biologically important targets.[68]

A series of ZIFs, including ZIF-7, ZIF-8, ZIF-67, ZIF-68, and ZIF-70 with different pore sizes, surface areas, and functional groups, were synthesized to serve as the matrix for constructing integrated dehydrogenase-based electrochemical biosensors for in *vivo* measurement of neurochemicals, such as glucose.[69] The biosensor was formed by coating a glassy carbon electrode with methylene green/ZIFs composites and following with glucose dehydrogenase. In a continuous- flow system, the ZIF-70 based biosensor was sensitive to glucose in a linear range of 0.1-2 mM. This biosensor was capable of selectively monitoring dialysate glucose collected from the brain of guinea pigs in a near real-time pattern (Figure 1.5).

7
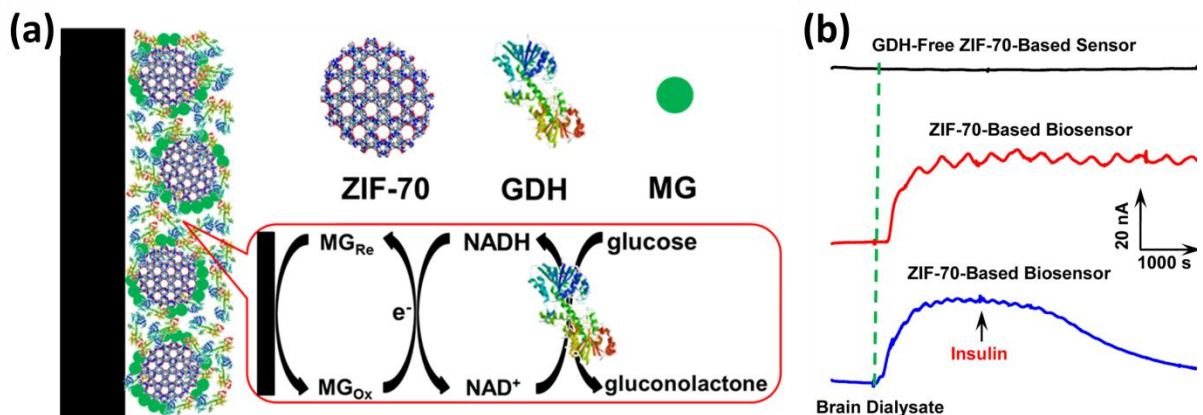
Figure 1.5 (a) The ZIF-70-based biosensor. (b) Online current−time response recorded for the brain microdialysates of guinea pig on the online detecting systems with the MG/ZIF-70-modified GC electrode (i.e., GDH-free ZIF-70-based sensor, black line) and ZIF-70-based biosensor (red and blue line) as the detector. (Taken from Ref. [69]*)*

1.1.3.4 Drug delivery

Due to regular porosity and organic functionality, MOFs are capable of optimal drug-delivery applications. The bulk MOF materials are able to uptake and release large amounts of therapeutics such as ibuprofen, procainamide, and nitric oxide. [17]

Férey and coworkers discovered the remarkable capacity for drug hosting and controlled delivery of the MIL family.[70] They explored the absorption and release of ibuprofen with MIL-100 and MIL-101. Both materials showed remarkable ibuprofen adsorption, 0.347 g ibuprofen/g MOF for dehydrated MIL-100 and 1.376 g ibuprofen/g MOF for dehydrated MIL-101, as a result of their different pore sizes. Compared with MCM-41, with a pore diameter of 36 Å, MIL-100 showed very similar ibuprofen dosage and kinetics. Interestingly, MIL-101 absorbed the drug by amount four times more than MCM-41, but released more slowly. Therefore, MIL-101 allows a higher drug dosage and a longer controlled delivery, which proves advantageous for larger pharmacological molecules.

1.2 Surface-mounted Metal-Organic Frameworks (SURMOFs)

MOF thin films are a rapidly developing field, which enable many potential applications, ranging from membrane separations over sensor techniques to potential electronic devices.[71-73] Fischer et al. distinguished the MOF thin films in two classes: polycrystalline films and surface-mounted

MOF (SURMOFs).[74] The former is generally regarded as an assembly of randomly oriented MOF crystals or particles on a surface. In some cases, the crystals prefer attaching in one particular direction with respect to each other and the surface of the substrates, which results in oriented films. The polycrystalline films can be prepared either during the reaction or from MOF powders. The approaches of these films include direct solvothermal deposition,[75] solvothermal mother solution,[76] spin-coating,[77] seeded growth,[78] electrochemical deposition[79] and Langmuir-Blodgett (LB) method.[80] The thicknesses of these films are related to the size of the MOF particles or crystallites, ranging up to micrometers. The surface-mounted MOF is a special class of MOF films, which is uniform and perfectly oriented. The SURMOFs were introduced by Wöll in 2007,[81,82] employing the liquid-phase epitaxy (LPE) approach to the MOF growth on a solid substrate. The thickness of the SURMOFs can be precisely controlled.[74] In the following, a more detailed description of SURMOFs will be provided.

1.2.1 Functionalized Surface

The first choice for the growth of MOF films is self-assembled monolayers (SAMs) on Au substrates.[76] SAMs are organic assemblies formed by the adsorption of molecular constituents from solution or the gas phase onto the surface of solids or in regular arrays on the surface of liquids.[83] Due to the relatively straightforward preparation, spontaneous assembly and diverse functionality, SAMs become an attractive interface for the MOF growth.[84]

In the case of Au substrate, three typical organothiols, 16-mercaptohexadecanoic acid (MHDA)[85], (4-(4-pyridyl)phenyl)-methanethiol (PP1)[86] and 11-mercapto-1-undecanol (MUD), are selected to assemble monolayer by carefully controlling synthesis conditions (Figure 1.6). The thiol groups react with gold following RSH + Au → RS-Au +1/2H$_2$ to form a self-assembled monolayer.

Apart from the fabrication on SAM surfaces, SURMOFs can also be deposited on other surfaces, ranging from polymer surfaces and conductive substrates over quartz glass to metal-oxide membranes, as well as multilayered SURMOF films, even differently shaped substrates, like magnetic nanoparticles.[87] Generally, the nonmetallic surface can be functionalized by plasma treatment to clean the surface and increase the hydroxyl groups on the surface. The functionalization can also be achieved by a chemical process, where the substrates are immersed in a piranha solution (98% H$_2$SO$_4$/30% H$_2$O$_2$ (3/1, v/v)) at 80 ℃ for 30 min to form -OH

9

functionalized surface.[88] The carboxyl groups can be obtained from hydroxyl by reacting with 11-(triethoxysilyl)undecanal.
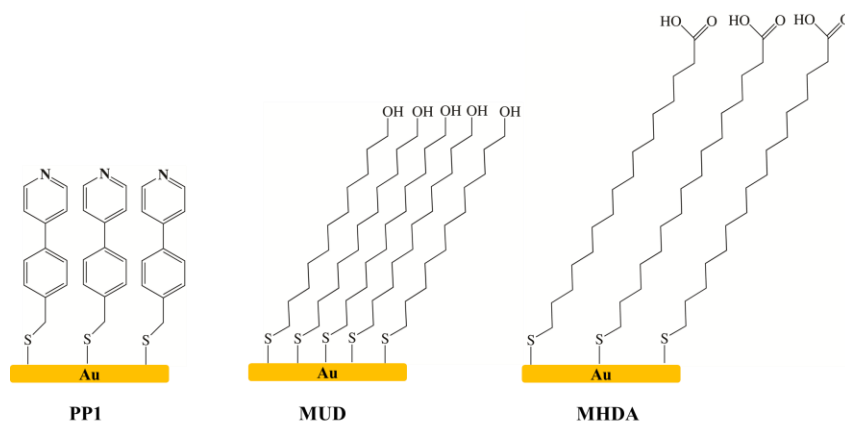
Figure 1.6 Typical SAMs on Au substrates for the growth of SURMOFs

1.2.2 Liquid phase epitaxy

Liquid-phase epitaxy (LPE) relies on the stepwise adsorption of components from the liquid phase to a surface, which is also called layer-by-layer (LbL) method. Since the early 1990s, layer-by-layer method has been developed for the construction of multi-composite films via the electrostatic attraction between oppositely charged molecules,[89] where a glass slide was alternatively immersed in solutions of positively charged and negatively charged components. Subsequently, Bell et al. synthesized Hofmann clathrate ([Ni(bpy)Pt(CN)$_4$]) layers, involving sequential adsorption of the three components of the solid from ethanol solutions.[90] The molecular building blocks were held together solely by covalent bonds.

In 2007, the LPE method was for the first time employed to grow MOF films on a surface,[81] as exemplified by HKUST-1 ([Cu$_3$(btc)$_2$]). The organic (e.g. H$_3$btc) and inorganic precursors (e.g. Cu(OAc)$_2$) were dissolved in pure ethanol and placed in separate beakers. The MHDA SAM, with a functional -COOH head group on Au substrate was immersed in the ethanolic Cu(OAc)$_2$ solution, where the metal compound chemically binds to the SAM. After rinsing with ethanol to remove any unreacted compounds, the substrate was immersed in H$_3$btc solution and the btc-linker molecules bind to the metal units, giving rise to the first layer of SURMOF. The repetition of these procedures was performed to obtain SURMOF films, see Figure 1.7. The rinsing with a solvent has been shown to be a crucial step for the oriented growth in the LPE process.[91]
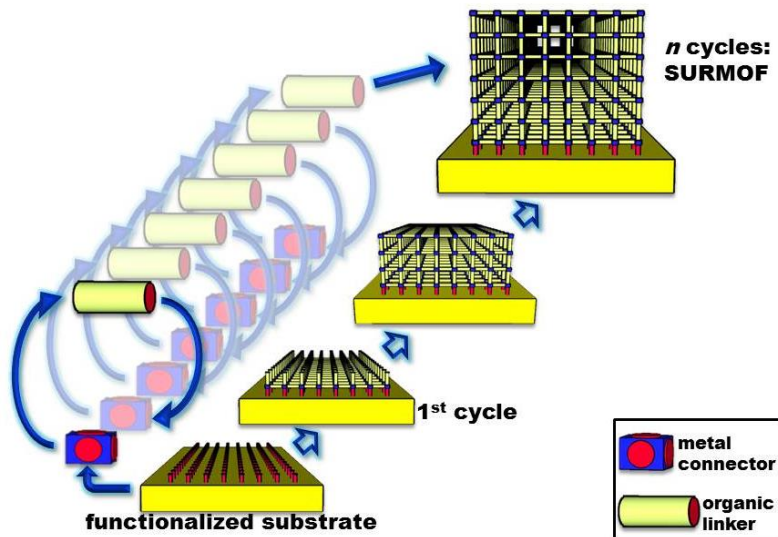
Figure 1.7 Step-by-step approach for the growth of the SURMOFs on a SAM-functionalized substrate. The approach involves repeated cycles of immersion in solutions of the metal precursor and solutions of organic ligand. Between steps the material is rinsed with solvent. (Taken from Ref.[87])

1.2.3 Techniques for the growth of SURMOFs

So far, several LPE based techniques have been established for the growth of SURMOF to achieve homogeneous morphology and high-throughput fabrication or monitor *in situ* experiments, including the dipping,[92,93]pump,[94] the spray[91] and quartz crystal microbalance (QCM)[95] methods. This method has also been extended to coat magnetite particles with SURMOFs.[96]

1.2.3.1 Dipping method

Manual-dipping is the initial method used to prepare the SURMOFs,[81] where four containers are required for solutions: (I) metal source, (II) rinsing solvent after metal precursor exposure, (III) organic ligands and (IV) rinsing solvent after ligand exposure. During the manual-dipping, the functionalized substrate is alternatively immersed into the containers with the order from I to IV. By subsequently repeating the immersion in a certain cycles, the SURMOF films with desired thickness and orientation are obtained. Generally, the soaking time in the metal and ligands precursors is tens of minutes, that is, each cycle requires 0.5-1.5 h, which consumes much time for thick films.
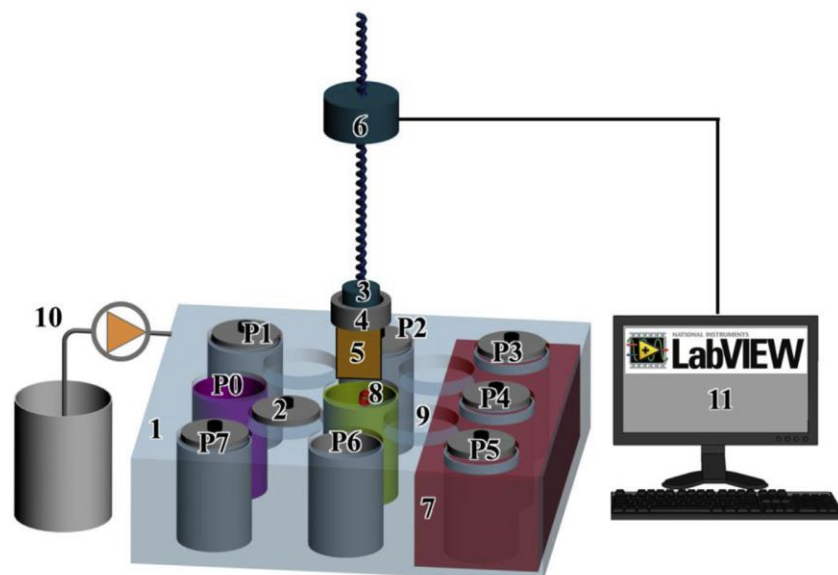
Figure 1.8 The setup of the dipping robot. P0: starting and final position for the sample holder; P1-P7: containers for immersion solutions; 1: Teflon working table; 2: container lid; 3: gripper; 4: sample holder; 5: sample; 6: position controller; 7: ultrasonic bath; 8: shower; 9: parking position of container lid; 10: pump and solution bottle for showering; 11: computer. (Taken from Ref.[93])

Recently, an automated, computer-controlled dipping robot equipped with an ultrasonic bath has been introduced to prepare homogeneous SURMOFs with low surface roughness and low defects density.[93] The setup is shown in Figure 1.8. The synthesis of HKUST-1 SURMOF growth on MHDA SAM is taken as an example. The functionalized substrate is dipped sequentially in an ethanolic copper acetate ($Cu(OAc)_2$, 1 mM) solution (P1), pure ethanol (P3), an ethanolic 1,3,5-benzenetricarboxylate (H_3btc, 0.2 mM) solution (P2) and again pure ethanol (P4) for 10 min, 2 min,15 min, 2 min, respectively. The ultrasonication is switched on during the immersion of the substrate in pure ethanol (P3 and P4). Between each step, the sample will go back to the center (8) of the table to be rinsed with the pure ethanol for typically 3 seconds to provide a more thorough rinsing. The repetitions of these dipping steps are performed to grow SURMOFs following a software (LabView) controlled protocol. It was proven that the samples prepared with the dipping robot equipped with ultrasonication have a significantly higher quality in terms of a considerably smaller surface roughness than the samples prepared without ultrasonication.[93]

12

1.2.3.2 Spray method

The spray method is regarded as a high-throughput technique, which denotes the reduction of the required time for preparing SURMOFs by more than two orders of magnitude.[91] the spray method is based on a nozzle system (Figure 1.9), where an aerosol of the reactant solutions required for the MOF synthesis is produced. There are three nozzles each for spraying the metal, ligands and pure solvent solutions, respectively. After the droplets of the aerosol impinge on the substrates, materials will be deposited at the solid-liquid interfaces and coat the surface with a thin film of the reactant.

In the spray process, separate metal and ligands solutions are sprayed alternatively on the substrates with a rinsing step in between by exposing the substrate to an aerosol produced from the pure solvent. Generally, it takes only a few hours to achieve a thickness of micrometer SURMOFs films with high quality.
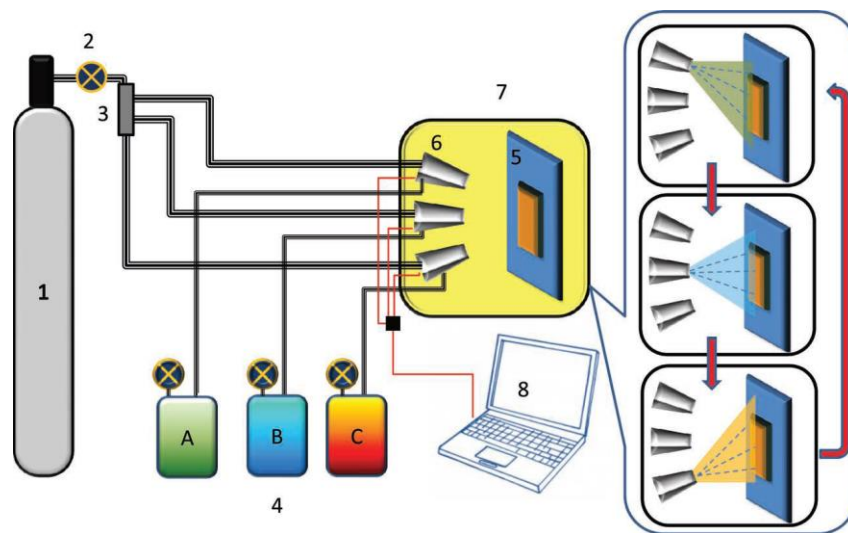
Figure 1.9 Setup employed for the fabrication of MOF thin films with the spray method: (1) Gas supply, (2) gas flow controller (3) three-way valve gas distributor (4) (A, B, C) solutions storage containers (5) sample holder (6) dosing valves, (7) spray chamber, (8) PC. (Taken from Ref. [91])

1.2.3.3 Pump method

Pump method[94] has been established to precisely control the temperature by a heating and cooling circulation system ranging from -20 to 100 ℃ during the growth of SURMOFs. The schematic diagram of the pump method for the fabrication of SURMOFs is shown in Figure 1.10.

There are four pumps. Among them, three pumps are responsible for the injection of the solution into the sample cell and the other one is used to pump the solution out of the cell. Similar to other techniques, the metal solution and organic linker solution are injected into the sample cell alternatively and in between the pure solvent is pumped through the sample cell to remove the excess reactants. The repetition of these steps produces the SURMOF thin films. All the steps are performed by a Labview program.
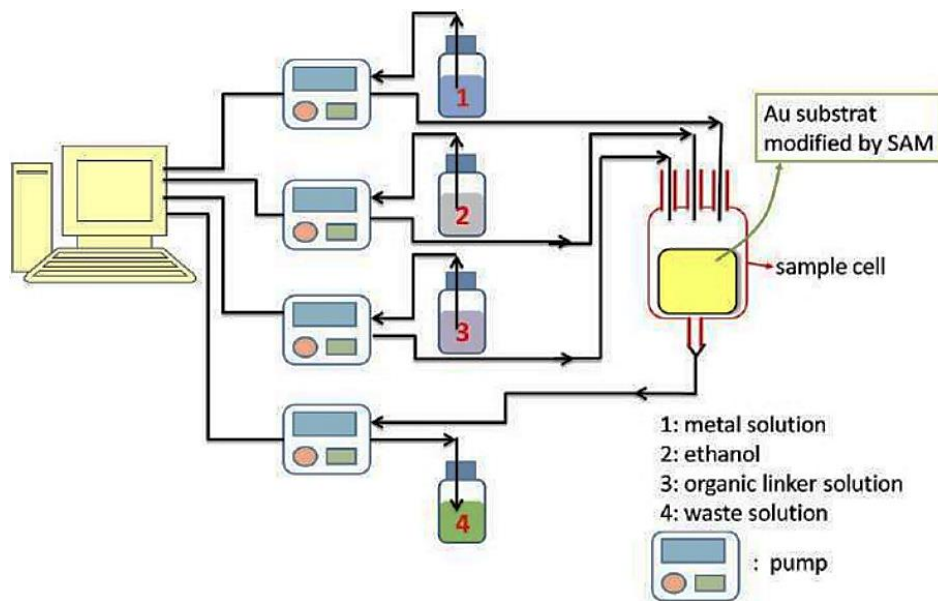
Figure 1.10 Diagram of the pump system for the automated layer-by-layer growth of SURMOFs. (Taken from Ref. [94])

1.2.3.4 Quartz crystal microbalance (QCM)

The quartz crystal microbalance (QCM) is used to measure the changes in the mass of piezoelectric quartz substrate during the loading with or the release of materials. The mass difference can be calculate from the change in the substrate resonant frequency with time by applying the Sauerbrey equation.[97] The QCM method for the growth of SURMOFs is an extension of pump method, where the solutions are also pumped into the QCM cell. During the synthesis, film growth is monitored by the changes of the resonance frequency of the sensor (Figure 1.11).

Here is a detailed preparation of SURMOFs by the QCM method. Firstly, a QCM sensor, an electrode coated with gold, functionalized with SAM is placed in the QCM cell. Then the pure

solvent is pumped through the QCM cell. After achieving a stable baseline, the metal solution, pure solvent and the organic ligand are pumped through the cell sequentially in a similar manner. After each subsequent flow, it will reach equilibrium as detected from the frequency signal, which means all the chemicals have reacted completely. The steps are repeated until sufficient materials are deposited on the QCM sensor. It is an automated real-time analytical instrument for the studies of molecular events occurring on the electrode surface.
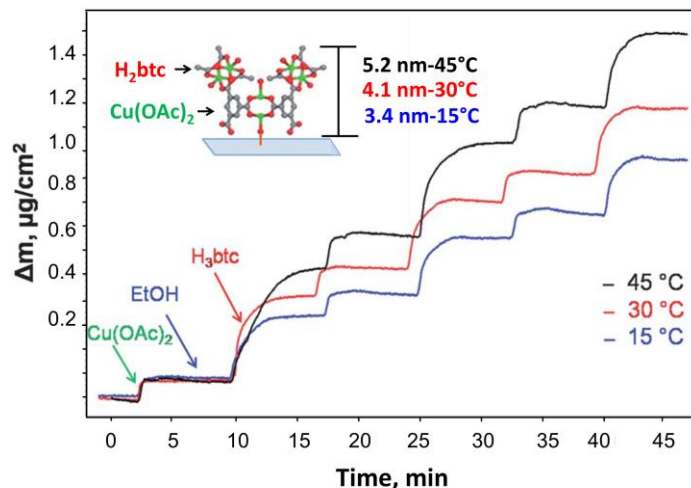
Figure 1.11 Sauerbrey mass change after three Cu(OAc)₂-H₃btc deposition cycles on SiO₂-coated electrodes at 15, 30 and 45 ℃.(Taken from Ref.[98])

1.2.3.5 Magnetic separation
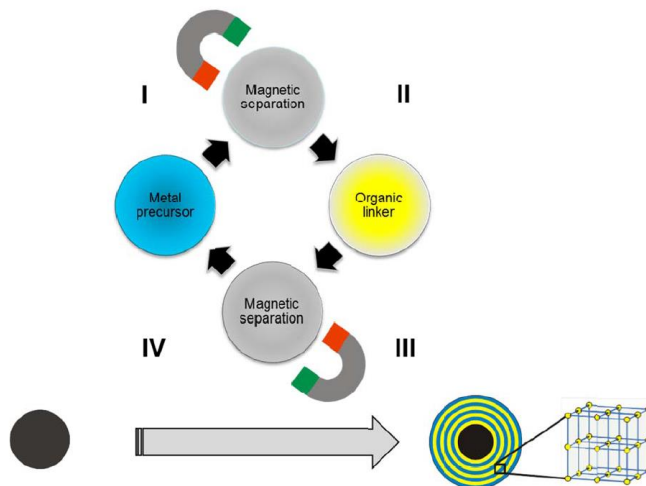
Figure 1.12 Stepwise liquid phase epitaxy growth of MOF thin films on the pretreated magnetic nanoparticles.(Taken from Ref.[96])

The LPE method for the growth of SURMOFs is not limited to the flat substrates, but can also be applied for the solid particles. More recently, highly defined magnetic MOF (magMOF) core/shell nanoparticles where the MOF coating is very homogeneous and of a uniform, well-defined thickness for all particles were fabricated based on a modification of the LPE process.[96] The scheme of this method is shown in Figure 1.12. For each full cycle, the magnetic particles are first immersed in metal precursor (I) solution and second in a solution of organic linker (II). In between the particles are washed with pure solvent to remove the unbound components. The separation of the magnetic particles from the suspension is performed by a magnet, which is fast, scalable and easily automated.

1.2.4 Advantages and applications of SURMOFs

In addition to the common properties of MOF films prepared by other methods, SURMOFs exhibit several unique properties, such as: (1) highly oriented and controllable growth orientation; (2) controllable thickness according to the number of the deposited; (3) smooth and homogeneous morphologies with roughness of the order of a few elementary cells; (4) easy scale-up in mild conditions and (5) lower defects.[99]

The unique properties of SURMOFs make these thin films perfectly suitable for the sensors in gas or liquid phase,[100] fabrication of membranes, determining the diffusion coefficient,[101] mass transfer investigations and other MOF properties in a quantitative fashion.[87]

1.3 Surface-grafted gels (SURGELs)

Functionalization of MOFs can be realized by using linkers with extra functional groups or by a so-called post-synthetic modification (PSM). In general, PSM leads to new MOF configurations by covalently reacting molecules into the framework, which cannot be achieved during the synthesis of MOFs. A number of MOFs, from IRMOF-3 to ZIF-90, even SURMOFs, are amenable to PSM.[102] Wang et al. obtained functional SURMOFs using post-synthetic modification based on two types of azide-alkyne click reaction, Cu(I)-catalyzed and strain-promoted, as well as to monitor such reaction using IRRAS and XRD. The results revealed that the yield could reach almost 100%.[103]

SURMOFs grown using liquid-phase epitaxy on functionalized substrates are an interesting class of MOFs that have wide applications as surface coatings. The cytotoxic metal ions and instability

against water of some SURMOFs limit the biological application, for example, cell culture. To settle the problem, surface-grafted gels (SURGELs) with three-dimensional structure were first proposed and fabricated by Tsotsalas et al. in 2013.[104] The linker equipped with azide side groups were used to achieve the post-synthetic modification via click chemistry. The scheme of the approach for SURGEL is shown in Figure 1.13. The SURGELs were synthesized from SURMOFs via copper-free click reaction of the ligands (diazido-stillbenedicarboxylic acid) with the cross-linker (trimethylolethane tripropiolate), followed with ethylenediaminetraacetic acid (EDTA) treatment to remove the metal ions.[104] The obtained film is metal-free and covalently connected. The corresponding XRD and IRRAS data confirmed the coupling reaction and revealed that the SURGELs are amorphous.
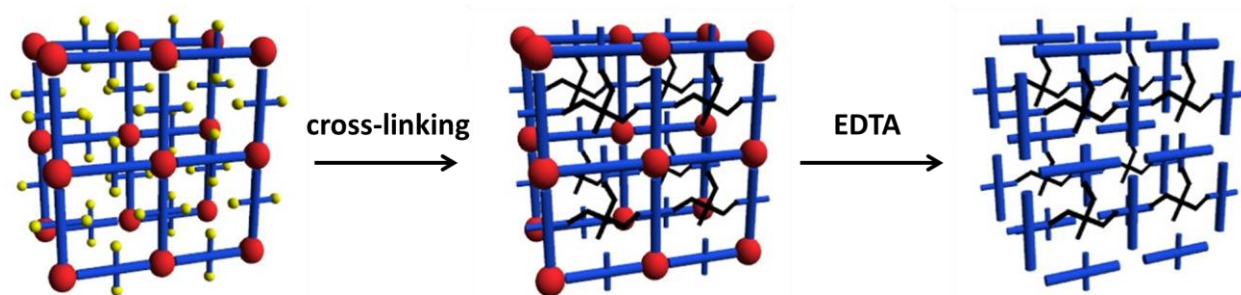
Figure 1.13 Schematic representation of SURGELs synthesis.(Modified from Ref.[104])

The SURGELs combine the advantages of MOFs and polymer hydro-gels, exhibiting the properties of versatile chemistry with various functional groups, pronounced water stability and metal ions absence.[104,105] SURGELs provide a drug-release platform in *in vitro* cell culture studies[104] as well as the chance of introducing guests into the SURGELs.[106] The method of SURGELs synthesis has been successfully extended to the fabrication of SURGEL capsules (magGELs), where the cargo molecules can be loaded and released under different environment.[105]

1.4 Porphyrins

1.4.1 Introduction
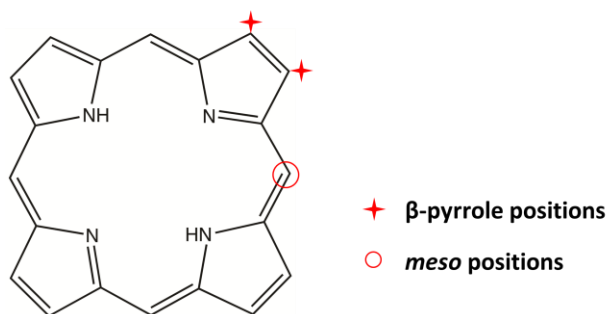
Figure 1.14 The unsubstituted porphyrin macrocycle

Porphyrins are a group of compounds containing the porphin structure to which a variety of side chains are attached. As shown in Figure 1.14, the simplest porphyrin, named porphin, are composed of four modified pyrrole (5-membered organic ring) subunits connected by methine (=CH-) bridges. The structure of porphyrin supports a highly stable configuration of single and double bonds with aromatic character, resulting in a highly-conjugated molecule containing 18 pi-electrons. The porphyrin nucleus is a tetradentate ligand in which the space available for a coordinated metal has a maximum diameter of approximately 3.7 Å. During the coordination, two protons are removed from the pyrrole nitrogen atoms, leaving two negative charges,[107] which could bind with transition metal ions to form metalloporphyrins. In the porphyrin macrocycle, there are two different sites where electrophylic substitution can take place with different reactivity[108]: *meso* and *β*-pyrrole positions.

Porphyrins are involved in the metabolism of living organisms and have a universal biological distribution, for example, the iron-containing porphyrins found in hemoglobin[109] and the reduced magnesium-containing porphyrins found in chlorophyll.[110] The history of porphyrin synthesis began in the middle of the 1930s. Hans Fischer's group developed an enormous number of synthetic procedures for porphyrins and began to investigate and manipulate the chemistry of the porphyrin macrocycle and its diverse substituent groups.[111] Until now, the synthesis of porphyrins has been achieved by common methods, ranging from using naturally occurring hemoglobin or chlorophylls to total synthesis from monopyrroles. Various synthetic routes are available in the literature for the synthesis of substituted porphyrins and for the

structural modification of porphyrins, such as monopyrrole polymerization, MacDonald route ((the [2+2] approach)),[112] a [3+1] approach[113] and from a,c-Biladiene salts.[114] The choice of the synthetic route depends upon the symmetry features of the porphyrins.

Owing to structural robustness, attractive absorption and emission properties, strong aromaticity and rich metal coordination chemistry properties, porphyrin and derivatives have been successfully utilized across a wide range of applications, such as mimicking enzymes,[115] chemical sensor,[116,117] photodynamic therapy (PDT),[118,119] molecular electronic devices[120] and dye-sensitized solar cells,[121,122] as well as many applications as functional materials, like non-linear optical materials,[123] light-emitting materials,[124] magnetic materials.[125]

1.4.2 Porphyrin-based MOFs

Due to the above properties and wide applications, porphyrins have successfully attracted attentions to construct MOFs recently. Various kinds of MOFs constructed from porphyrin-based linkers have been synthesized.[126]

The first porphyrin-based coordination polymer was reported in 1991,[127] earlier than the benchmarks of HKUST-1 and MOF-5. However, the first porphyrin-based MOF supported by 5, 10, 15, 20-tetra-4-pyridyl-21H, 23H-porphine (H$_2$TPyP) and Cu$_2$(AcO)$_4$ was successfully synthesized in 2006, which is constructed by the self-assembly of a 2D coordination network consisting of a 22.2 Å square grid. The characterization by N$_2$ adsorption indicated that this coordination network has uniform micropores and gas adsorption cavities.[128] Since then, an exponential increase in the numbers of porphyrin-based MOF structures has occurred.[126]

Hupp's group combined ZnPO-MOF under solvothermal conditions (Figure 1.15 (a)), with large channels in three directions occupied by a substantial amount of disordered solvent. The free-base porphyrin was metallized during the course of the solvothermal synthesis. The obtained ZnPO-MOF can efficiently catalyze acyl-transfer reactions primarily by preconcentrating the substrates within its pores, in stark contrast to analogous supramolecular systems [129] Afterwards, a pillared-paddlewheel type MOF featuring bodipy- and porphyrin-based struts, and capable of harvesting light across the entire visible spectrum (Figure 1.15 (b)), has been synthesized via a standard solvothermal method by the same group.[130]
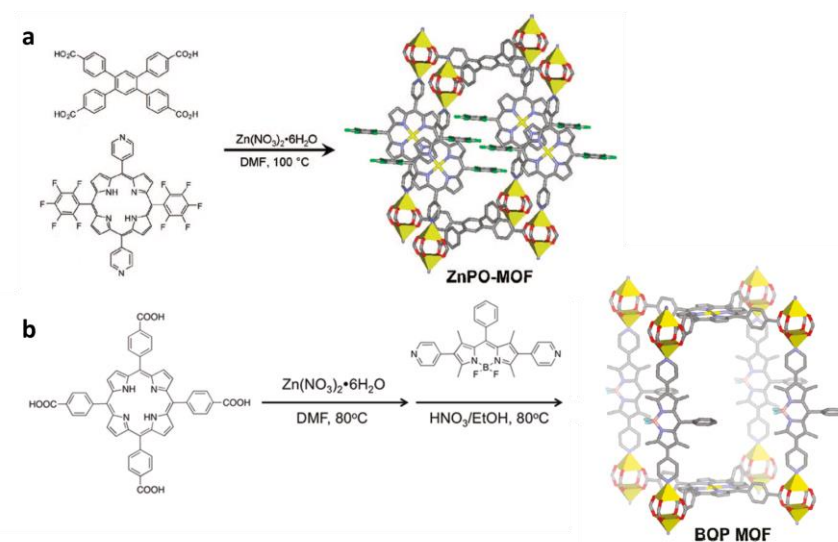
Figure 1.15 Synthesis procedures of (a) ZnPO-MOF and (b) the isostructural BOP MOF (Taken from Ref.[129,130])

Kitagwa and coworkers applied the layer-by-layer deposition coupled with the Langmuir Blodgett (LB-LbL) technique using CoTCPP and pyridine molecular building units spread onto an aqueous solution of $CuCl_2$ $2H_2O$ in a Langmuir trough, leading to the formation of a copper-mediated CoTCPP 2D array (CoTCPP-py-Cu) on the substrates, named NAFS-1.[80] Subsequently, they used the same method to prepare NAFS-2 consisting of 5, 10, 15, 20-tetrakis(4-carboxyphenyl)porphyrin (H_2TCPP) molecules and copper ion metal linkers were assembled on a surface. The interlayer spacing in NAFS-2 varied while retaining the same in-plane molecular arrangement by employing different molecular building units than for the previously reported NAFS-1. The obtained NAFS-2 showed a thermal stability above 200 ℃.[131]

H. C. Zhou et al. employed Fe-TCPP (TCPP = tetrakis(4-carboxyphenyl)porphyrin) as a heme-like ligand and chose highly stable Zr_6 clusters as nodes to construct a 3D heme-like MOF, designated as PCN-222(Fe). The PCN-222(Fe) , acting as an effective peroxidase mimic, shows good activity for the oxidation of a variety of substrates.[132]
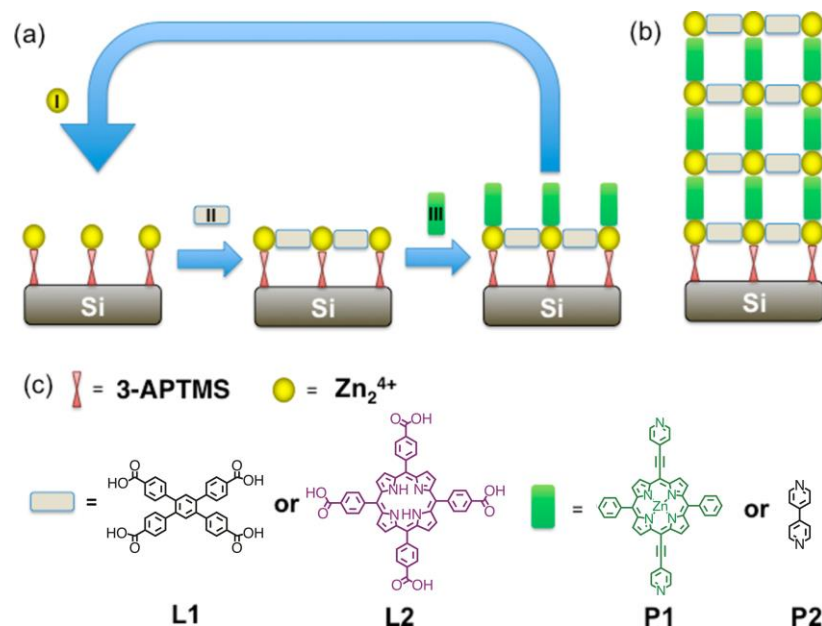
Figure 1.16 (a) Schematic diagram of step-by-step growth of the DA-MOF and L2-MOF structures resulting in (b) a film after N cycles of growth. (c) Representations of building blocks used in fabrication of MOF film. (Taken form Ref.[133])

A pillar-layered paddlewheel type MOFs, DA-MOF consisting of [5,15-di(4-pyridylacetyl)-10,20-diphyenyl] porphyrinatozinc-(II), 1,2,4,5-tetrakis(4-carboxyphenyl)benzene, zinc-(II) acetate (Zn_2^{4+}) and L2-MOF composed of Zn_2^{4+}, 4,4'-bipyridine (P2), and 5,10,15,20-tetrakis(4-carboxyphenyl)porphyrin (Figure 1.16), have been synthesized on functionalized surfaces using a layer-by-layer (LbL) approach. The obtained porphyrin-based MOF thin films are preferentially oriented, highly porous and have controlled thickness.[133] Long-range energy transfer is demonstrated for both MOF films and the findings point to the potential utility of porphyrin-based MOF films for light-harvesting and efficient energy transport in solar energy conversion devices.

1.5 Objectives

In the past, a large amount of work has been devoted to prepare porphyrin thin films on solid substrates using different techniques, especially self-assembly approach, but the resulting systems are not highly ordered and crystalline. Recently, numerous "artificial or human-made" porphyrins MOFs have been prepared, but mainly focused on solvothermal synthesis. The studies regarding thin film of porphyrin-base MOFs are quite rare.

The major aims of this thesis are the preparation of porphyrin-based SURMOFs by LPE approach and the investigations of their properties as photovoltaic devices. The LPE approach avoids the metalloporphyrin complexes which are always produced during the conventional solvothermal synthesis. Herein, two groups of different porphyrin SURMOFs were prepared: free base porphyrin and Pd metalized porphyrin SURMOF, Zn(II)porphyrin and DPA-Zn(II)porphyrin SURMOF. Due to the light-harvesting properties, all the porphyrin based SURMOFs were assembled as photovoltaic devices. The obtained porphyrin-based SURMOFs provide a platform for in-depth investigations between structure-function relationships.

Porphyrins serve as the electron-donor in the electron and energy-transfer processes. If the porphyrin is combined with an acceptor moiety, a donor-acceptor (D-A) system is formed. The formation of D-A systems plays a very important role because of the potential application of such systems to enable artificial photosynthesis and organic solar cells. Among the donor-acceptor systems, porphyrin-fullerene systems are one of the widely studied classes of compounds due to their rich photo- and redox chemistry.[134] Therefore, to improve the properties of the porphyrin SURMOF based photovoltaic devices, C_{60}-fullerene were involved in the porphyrin SURMOF.

Surface-grafted gels (SURGELs), with the absence of cytotoxic metal ions and pronounced stability against water, have high potential for applications in biology, especially porphyrin based SURGEL that combines the advantages of porphyrins. In this thesis, post-synthetic modification was used to modify the porphyrin SURMOF equipped with two azide groups. Then, further experiments were carried out to synthesize porphyrin SURGEL via cross-linking and removal of metal ions.

In addition, the mass transfer of guest molecules in nanoporous host materials, in particular in MOFs, is among the crucial features of their applications. Finally, the diffusion of ferrocene in vapor and in ethanolic and hexanic solution in HKUST-1 was investigated by using SURMOF thin films in combination with QCM technique.

2 Characterization methods

In this section, the relevant methods and instruments applied for the characterization of synthesized thin films in the thesis are described, including X-ray diffraction (XRD), ultraviolet-visible (UV-Vis) spectroscopy, infrared spectroscopy (IR), scanning electron microscope (SEM), X-ray photoelectron spectroscopy (XPS), quartz-crystal microbalance (QCM), fluorescence lifetime, transient absorption spectroscopy (TAS) and flash-photolysis time-resolved microwave conductivity (FP-TRMC).

2.1 X-ray diffraction (XRD)

XRD is one of the most important, powerful and widely used analytical techniques available to determine the nature and identity of crystalline substances. A primary use of this technique is the identification and characterization of compounds based on their diffraction pattern. XRD has been applied to many different types of materials including single crystals, poly- and amorphous materials, thin film analysis, sample texture evaluation, monitoring of crystalline phase and structure, and investigation of sample stress and strain. Therefore, the XRD technique is used to determine the crystalline structure of the synthesized SURMOF thin films in the studies.

The principle of X-ray diffraction is based on the constructive interference of X-ray radiations resulting from the interaction through the probed crystalline sample. The X-ray wavelengths are comparable with the inter-atomic distances. A crystalline material has an ordered and periodic arrangement of elements. When incident monochromatic X-rays impinge on a sample, their scattered waves off the various crystal planes within the sample can interfere constructively. This constructive interference produced the so called "X-ray diffractions", which were first discovered by Laue in 1912. Braggs proposed the Bragg's law related the X-ray diffraction pattern with the crystalline structure of the probed material as exemplified by their study of the crystalline structure of sodium chloride (NaCl) and potassium chloride (KCl) using XRD. Bragg diffraction principle is schematically shown in Figure 2.1. Two coherent beams of X-rays approaching a crystalline solid are scattered off two different atoms from neighboring lattice planes separated by the inter-planar distance d and undergo interference. Constructive interference occurs when the path difference between two waves, $2d \sin \theta$ as shown in Figure 2.1, equals to an integer multiple of the X-ray wavelength. The Bragg's law can be expressed as follows:

$$n\lambda = 2d \sin \theta \qquad\qquad\qquad\qquad\qquad\qquad\qquad\qquad\qquad (2.1)$$

where n is a positive integer which defines the order of the reflection; λ denotes the wavelength of the incident X-rays; d is the perpendicular spacing between the lattice planes and θ is the scattering angle.
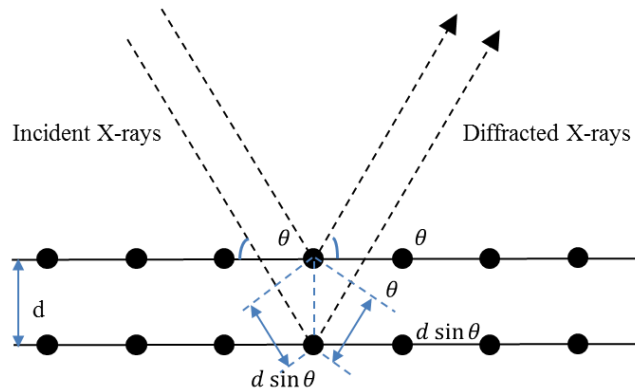
Figure 2.1 Schematic representation of XRD showing the geometrical parameter of the Bragg's law with the solid lines representing two d distant crystalline planes and the solid beads the atoms.

For the powder materials, there are often many individual crystals of random orientation in the sample, so all possible Bragg diffractions can be observed in the "powder pattern". Consequently, the structure of the crystal can then be determined by comparing the measured diffraction patterns with simulated results or with a database. However, a thin-film sample is two-dimensionally formed on the surface of a substrate, and normally has a large anisotropy either parallel along the stacking (thickness) direction or in the in-plane direction (within surface plane). Therefore, it can be difficult to use a conventional powder diffractometer to acquire high-quality diffraction data from a thin film and it is necessary to obtain the information in both directions. Generally speaking, X-ray diffraction techniques for thin films can be divided into two groups in terms of sample geometry; "out-of-plane" diffraction or "in-plane" diffraction.

Out-of-plane diffraction can be obtained by collecting diffracted X-rays from crystal lattice planes that are parallel to the sample surface and gives crystallographic information along the perpendicular direction to the sample surface. While in the case of in-plane, the perpendicular

directions of these lattice planes to be measured lie parallel to the sample surface. Figure 2.2 shows a schematic diagram of geometries for the two measurement techniques.
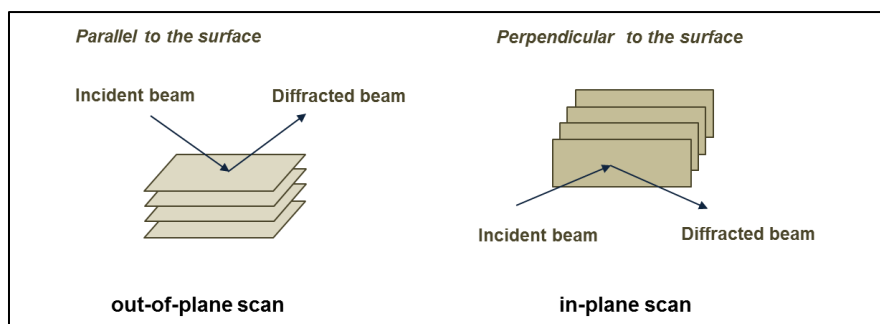
Figure 2.2 Schematic diagrams of geometries for the out-of-plane and in-plane XRD scan mode

In this thesis, both out-of-plane and in-plane XRD were carried out on two diffractometers, respectively. For the out-of-plane, a Bruker D8 Advance was equipped with a Si-strip detector (PSD Lynxeye©) in θ–θ geometry. On the tube side a variable divergence slit was placed and on the receiving side a 2.3 ° Soller-slit was used. For the in-plane, a Bruker D8 Discover in θ-2θ geometry was equipped with a quarter Eulerian cradle, tilt-stage, 2.3 °Soller-slits on both sides, a Göbel-mirror, and a PSD Lynxeye®. For both machines, Cu-anodes producing Cu Kα1,2 radiation ($\lambda = 0.15419$ nm) was used.

2.2 Ultraviolet-visible (UV-Vis) spectroscopy

The ultraviolet-visible (UV-Vis) spectroscopy is divided, according to the wavelength, into ultraviolet (UV, 200-400 nm) and visible (Vis, 400-700 nm) regions, where a molecule undergoes electronic transition under the ultraviolet or visible radiation. It commonly provides the information about π-electron system, conjugated unsaturation, aromatic compound and conjugated non-bonding electron system.

The total energy of a molecule is considered as the sum of its electronic energy, the vibrational energy between its constituent atoms and the rotational energy. An electronic transition could be sufficiently excited by the energy from UV to visible range, so the UV-Vis spectroscopy is also called electronic spectroscopy. When the energy from UV or visible light is absorbed by a molecule, one of its electrons will be excited from a lower to a higher energy orbital. Generally, the lowest occupied molecular orbitals are σ orbitals. The π bonding orbitals have higher energy

25

than the σ orbitals, but lower energy than the non-bonding (n) orbitals. The exact energy difference between the orbitals depends on the atoms and the bonding system. Under the electromagnetic radiation with an appropriate frequency, a transition will occur to excite one electron from its occupied orbital to an empty orbital, which is usually an antibonding orbital (σ* or π*) (Figure 2.3).
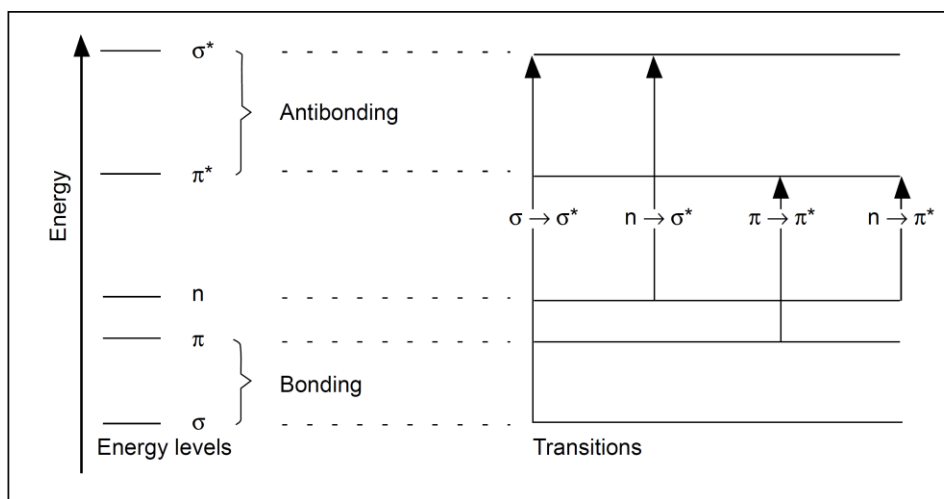
Figure 2.3 Electron transitions in UV-Vis spectroscopy (Taken from Ref.[135])

UV spectroscopy obeys the Beer-Lambert law, which states that absorption is proportional to the number of absorbing molecules and the fraction of absorbed radiation is independent of the intensity of the radiation. The Beer-Lambert law is expressed as:

$$A = \log_{10} \frac{I_0}{I} = \varepsilon l c \tag{2.2}$$

where A is the absorbance, I_0 is the intensity of the incident radiation, I is the intensity of the transmitted radiation, ε denotes the molar absorptivity, l is the path length of the absorbing solution in cm and c is the concentration of the absorbing species in mol dm^{-3}. From the Beer-Lambert law, it is clear that the greater the number of molecules capable of absorbing light of a given wavelength, the greater the light absorption. This is the basic principle of UV spectroscopy.

The UV-Vis spectra were recorded on an Agilent Cary 5000 UV-Vis-NIR spectrophotometer in the 175-3300 nm range of wavelength. All the UV-Vis spectra were recorded in transmission mode.

2.3 Infrared (IR) spectroscopy

Infrared spectroscopy is a technique based on the vibrations of atoms of a molecule. Infrared refers to that part of the electromagnetic spectrum between the visible and microwave regions. When the IR radiation passes through organic molecules and matches the molecular vibration energy, it will be absorbed by the molecules and converted into energy of molecular vibration. The information of the vibration frequency between bonding atoms of the measured material will be obtained from the resulting IR spectrum.

Vibration includes a change either in bond length (stretching) or bond angle (bending) (Figure 2.4 (a)). Some bonds can stretch in-phase (symmetrical stretching) or out-of-phase (asymmetric stretching), as shown in Figure 2.4 (b). If a molecule has different terminal atoms, such as HCN, ClCN or ONCl, the vibration turns to be the joint effect of each group.
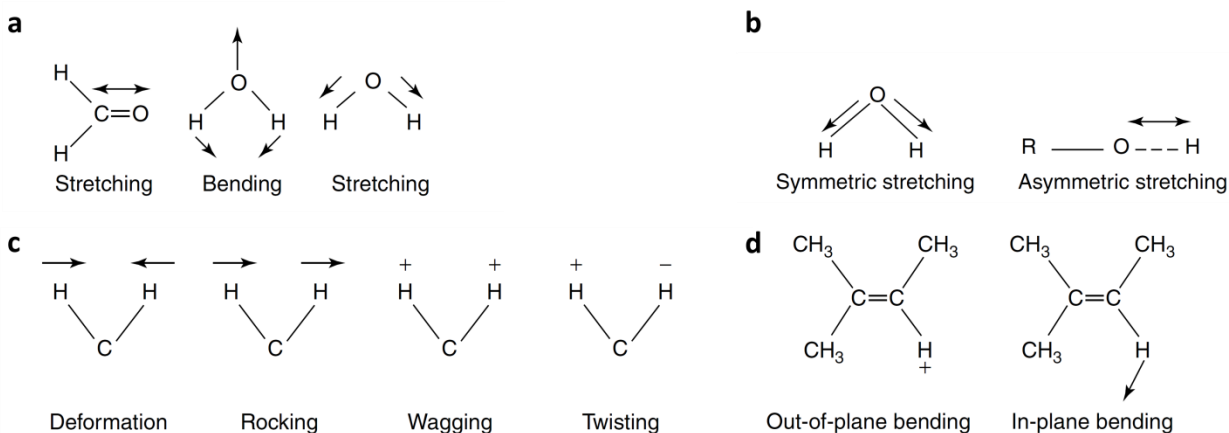
Figure 2.4 (a) Stretching and bending vibrations. (b) Symmetric and asymmetric stretching vibrations. (c) Different types of bending vibrations. (d) Out-of-plane and in-plane bending vibrations.(Taken from Ref.[136])

Bending vibration also contributes to the infrared spectrum, which is summarized in Figure 2.4 (c). It is better to imagine the molecule being cut by a plane through the hydrogen atoms and the carbon atom (the plane of the page in here). The hydrogen atoms can move in the same direction

27

or in opposite directions in this plane. For more complex molecules, the analysis becomes simpler. In this case, hydrogen atoms could be treated as isolated since they are usually attached to more massive (rigid) groups. This results in in-plane and out-of-plane bending vibrations, as illustrated in Figure 2.4 (d).[136]

Therefore, IR spectroscopy is a reliable and generally accepted method which allows identifying and characterizing numerous chemical moieties within the studied material. In this thesis, two kinds of IR spectroscopy techniques were used: attenuated total reflection and infrared reflection-absorption spectroscopy.

2.3.1 Attenuated total reflection (ATR) spectroscopy

Attenuated total reflection (ATR) is a technique used to record the infrared characteristics of solid or liquid samples without prior preparation. The basic principle of ATR is depicted in Figure 2.5. The beam undergoes multiple internal reflection in an optically dense crystal of a high refractive index surface in contact with the sample. Evanescent waves generated in the internal reflection extend only to a few microns (0.5-5 μm) off the crystal-sample interface, i.e. into the sample. The evanescent waves are attenuated or altered in regions of the infrared spectrum where the sample absorbs a part of the energy. The attenuated IR radiation is reflected back and exits from the other end of the crystal to be recorded by the detector, resulting in the specific absorption spectrum of the sample.
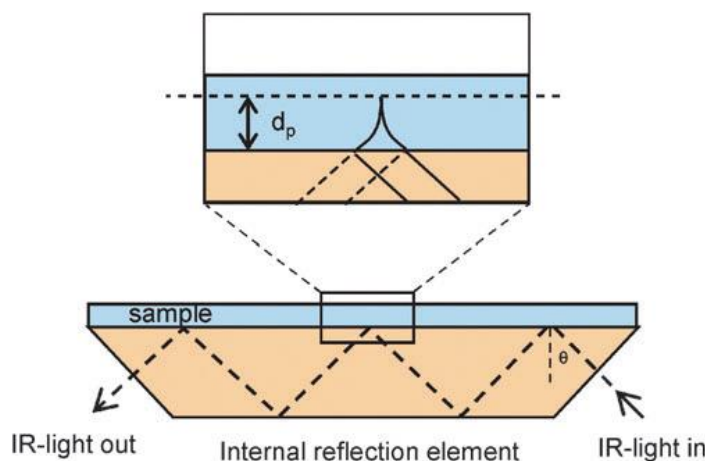
Figure 2.5 Schematic representation of ATR principle.(Taken from Ref.[137])

In the thesis, ATR measurements were obtained with a resolution of 4 cm^{-1} by a Bruker Optics Tensor 27 spectrometer equipped with platinum® ATR accessory and a deuterated L-Alanine doped triglycine sulfate (LaDTGS) detector. The spectra were recorded at room temperature (ca. 22 ℃) using air as background.

2.3.2 Infrared reflection-absorption spectroscopy (IRRAS)

Infrared reflection-absorption spectroscopy (IRRAS), also known as grazing-angle infrared spectroscopy (GAIRS), is a well-established tool to identify a wide range of functional groups present on the surface as well as their orientations relative to the reflective surface. It is typically applied to thin films on highly reflective surfaces, such as SAMs on gold surfaces.

This technique is based on the theory developed by Greenler et al.,[138,139] who were the first to note the advantage of using light near grazing incidence and the large difference in the absorption coefficient between light polarized perpendicular to the plane of reflection and that polarized parallel. In the reflection-absorption measurement, a linearly polarized light is separated into orthogonal components, *s*- and *p*- polarized light, where *s*-polarized light is perpendicular to the plane of incidence and *p*-polarized light is parallel to the plane of incidence. When the *s*-polarized light is reflected from the surface, it undergoes a phase change of 180 ° and the electric vectors at the surface sum to near zero, yielding no electric field at the surface. The *p*-polarized light undergoes a phase shift of about 90 ° and the resultant standing wave at the surface is oriented along the surface normal, as shown in figure 2.6 (a), where the electric field components are denoted by E$_p$ and E$_s$.
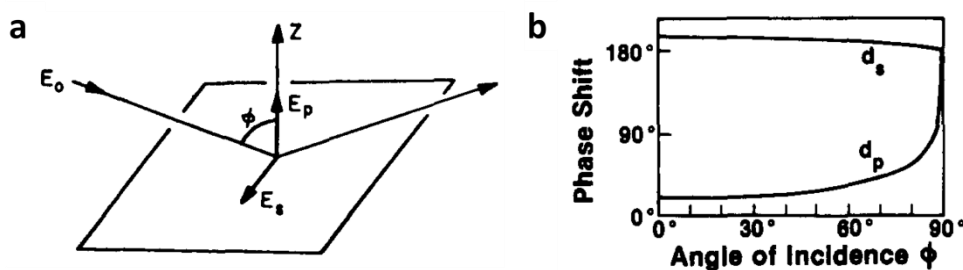
Figure 2.6 (a) Reflection of light at a surface. (b) Phase shift of the s (d$_s$) and p (d$_p$) component radiations versus angle of incidence φ at a clean metal surface. (Taken from Ref.[140])

The phase shift effect is strongly dependent on the angle of incidence and a large resultant electric field is established at grazing incidence. Calculated from Maxwell's equations, the *p*-polarized light goes through a sharp maximum at 88 °, *s*-polarized light remains virtually unchanged and very small for all angles (Figure 2.6 (b)). Therefore, the best condition for IRRAS is using *p*-polarized light incident on the surface at a grazing angle.

On metallic surfaces, the electric field of the incident light and the dipole moment of the adsorbed molecule interact with the metal electrons, which imposes a strict dipole selection rule. Modes that are completely parallel to the surface do not interact with *p*-polarized light and are not vibrationally excited. Only vibrations with dynamic dipole moment component perpendicular to the surface will be excited.

The IRRA spectra were acquired with a resolution of 2 cm^{-1} using an infrared spectrometer (Bruker VERTEX 80), with an angle of incidence amounting to 80 ° relative to the surface normal and a liquid nitrogen cooled mercury cadmium telluride (MCT) narrow band detector under ambient conditions. Perdeuterated hexadecanethiol SAMs on Au substrates were used as background for the SURMOFs.

2.4 Scanning electron microscopy (SEM)

The scanning electron microscopy (SEM) is a powerful instrument, which permits the images of heterogeneous organic and inorganic materials and surfaces on a scale of micrometer or submicrometer.[141] The principle of the instrument is shown in Figure 2.7.

The electron gun, including a hot tungsten filament as a thermionic source, emits and accelerates the electrons toward an anode that can be varied from 0.1 kV to 30 kV.[142] After the beam passes the anode, it is influenced by two electromagnetic lenses, which are used to focus and define the electron beam and to form a small focused electron spot on the specimen, respectively. The original electron source of around 50 μm is reduced by 5000 times to 1-100 nm.

Between the lenses, there is a single or double deflection field, where the deflector coils can move the beam focus over the sample in both *x* and *y* directions. At the lower portion of the column the specimen stage is located. Complex interactions occur when the electron beam impinges on the surface, which generates exciting signals from the chosen area of the specimen surface. The signals include secondary electrons (that produce SEM images), backscattered

electrons (BSE), diffracted backscattered electrons (EBSD that are used to determine crystal structures and orientations of minerals), photons (characteristic X-rays that are used for elemental analysis and continuum X-rays), visible light (cathodoluminescence-CL), and heat. Among them, secondary electrons and backscattered electrons are commonly used for imaging samples.

The measurement is carried out at high vacuum condition, which allows electron traveling without scattering by the air. The whole system provides a real-time observation and image recording of the specimen surface.
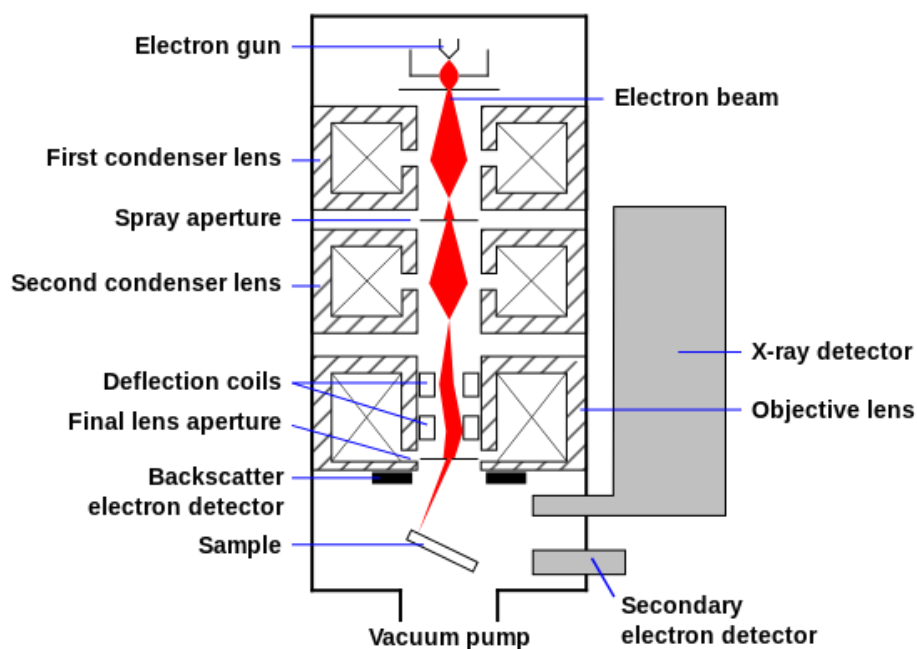
Figure 2.7 Schematic diagram of the scanning electron microscope. (Taken from Ref.[143])

In this thesis, the sample morphologies in thesis were analyzed on a Philips XL 30 Field Emission Gun Environmental Scanning Electron Microscope (FEG-ESEM) at 20.0 kV at the Institute of Functional Interfaces, Karlsruhe Institute of Technology by Moritz Ebeler.

2.5 X-ray photoelectron spectroscopy (XPS)

X-ray photoelectron spectroscopy (XPS), also known as electron spectroscopy for chemical analysis (ESCA), is an important and widely used surface analysis method. XPS is referred to as

the measurement of core electron binding energies. The energy of X-ray is sufficient to eject an electron whose binding energy is lower than the exciting X-ray.[144]

The work principle of this technique is based on the photoelectric effect outlined by Einstein in 1905 where the concept of the photon is used to describe the ejection of electrons from a surface when photons impinge upon it, as shown schematically in Figure 2.8 (a). When the X-ray photons interact with an electron in the K shell, it will lead to the emission of 1s electron, which could be detected and its energy measured. The determination of the kinetic energy of the outgoing electron is the cornerstone of experimental XPS.[145]

When the specimen is irradiated with the X-ray with a known energy (hv), the electrons with binding energy (E_b) lower than hv can be ejected. The kinetic energy (E_k) of these ejected electrons can be measured in the spectrometer and is given by:

$$E_k = hv - E_b - \emptyset_{sp} \tag{2.3}$$

where φ_{sp} is the work function (energies required to remove electrons from the Fermi to vacuum levels) of the spectrometer, a constant for a given analyzer. As the photon energy of the X-ray (hv) and φ_{sp} are known and the E_k is determined experimentally, the calculation of the binding energy is a simple matter. A typical X-ray photoelectron spectrum is generated by plotting the measured photoelectron intensity as a function of binding energy, in which photoelectron peaks coming from different chemical elements can be identified by their characteristic energies.
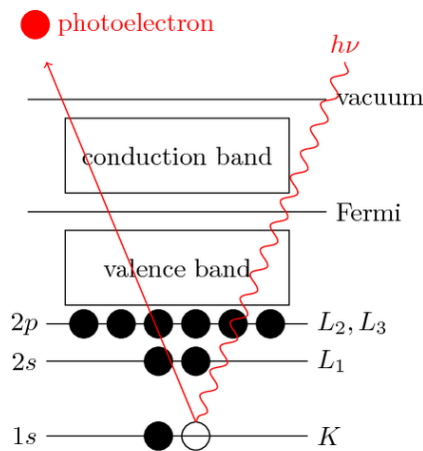
Figure 2.8 Schematic of photoemission process (Taken from Ref.[146])

An X-ray photoelectron spectrometer consist of a primary source of X-ray, a sample/support system, an electron analyzer and a detector, which are all maintained under an ultra-high vacuum (UHV) enclosure and suitable electronics to convert the detected current into a readable spectrum. The UHV conditions are necessary to ensure that the mean free path of the photoelectron is large enough to allow it to traverse the distance from the sample to the detector without suffering energy loss.[144]

Herein, XPS experiments were performed in a specifically designed ultrahigh vacuum system (base pressure 2×10^{-10} mbar) equipped with a hemispherical electron energy analyzer (VG-Scienta R4000) and a non-monochromatic Al Kα X-ray source.

2.6 Quartz-crystal microbalance (QCM)

The quartz crystal microbalance (QCM) is a simple, cost-effective, high-resolution mass sensing technique, based upon the piezoelectric effect.[147] It has been used for more than 50 years to effectively analyze mass changes on rigid surfaces in liquid, air or vacuum.

A quartz crystal microbalance consists of a thin quartz disk with metal (Au, Pt, etc.) electrodes deposited on either side of the disk (Figure 2.9). A resonant oscillation is achieved by connecting the crystal to an external driving oscillator circuit where the electric and the mechanical oscillations are close to the fundamental frequency of the crystal.[148] The so-called AT-cut crystal used in the QCM often oscillates in a shear mode.[149]

If any mass are added to or removed from the electrode, there will be a shift of the frequency (Δf), which is related to the mass change Δm according to the well-known linear Sauerbrey equation[150]:

$$\Delta f = -C\Delta m \tag{2.4}$$

where C is a constant that depends only on the thickness of the quartz slab and on the intrinsic properties of the quartz. The equation is also based on the assumption that the mass is rigidly attached to the electrodes, with no slip or deformation due to the oscillatory motion.[149]

The QCM measurements can be performed in several ways. One method is impedance analysis, using a vector analyzer to investigate the impedance of a quartz oscillator to obtain the polarization at the crystal surface as a function of the frequency of the applied voltage.[151,152]

The method results in two parameters per overtone, the resonance frequency f_n and the bandwidth Γ_n. Another method is referred to as QCM-D, which was developed by Rodal.[149] The crystal is driven at its resonant frequency by an oscillator that can be intermittently disconnected causing the crystal oscillation amplitude to decay exponentially. During the decay of mechanical oscillations, the resonance frequency f_n and the dissipation D_n are recorded, where D_n is related to the mechanical change of the film adhering at the sensor surface.[153] The third way is to operate with oscillator circuits, which can provide the bandwidth via the oscillation amplitude.[151]
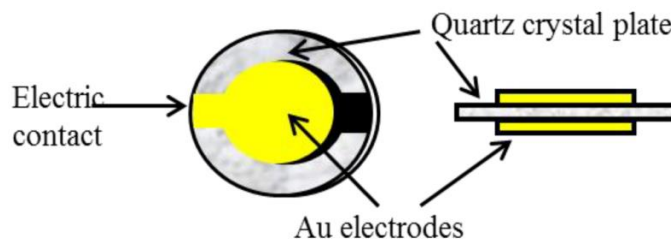
Figure 2.9 Schematic of a piezoelectric quartz crystal.(Taken from Ref.[154])

In this thesis, the experiments were carried out using the automated QCM-D instrument (Q-Sense E4), which can be operated in gas phase or liquid environments to monitor the resonance frequency changes on the gold electrode thin film.

2.7 Fluorescence lifetime

Generally, a molecule occupies the lowest vibrational level of ground state (S_0). After excited by sufficient energy, it can be transited to a higher energy level, S_1 or S_2, and create an atom or molecule in an excited state. This transition process is very fast, which is on the order of 10^{-15} seconds. The detailed description of photophysical processes is presented by the Jablonski diagram (Figure 2.10).

On the left are the singlet states, which maintain the paired $+\frac{1}{2}$ and $-\frac{1}{2}$ spin states of the electrons within a single orbital. The second excited singlet state S_2 contains more energy than the first excited state S_1, which has more energy than the ground state S_0.[155] After absorbing the energy and reaching one of the higher vibrational levels of an excited state, the molecule can dissipate the energy through vibrational relaxation, a non-radiative process, transiting from a vibration level in one electronic state to another vibration level in a lower electronic state, which

is called internal conversion, and finally reaching the lowest vibrational levels of the first excited state (S_1). From this level, the molecule can return to any different vibrational level of the ground state, emitting photons in the form of fluorescence. Fluorescence is a fast process on the order of 10^{-9} to 10^{-7} seconds.

The right hand of figure 2.10 there are the triplet states, where a pair of nonbonding electrons may exist in two separate orbitals and the spin vectors are parallel. When the lowest vibrational level of the excited singlet state (S_1) has the same energy as an upper vibrational level of the triplet state (T_1), the singlet state can transition to the triplet state, which is known as intersystem crossing. A radiative transition from an excited triplet state to a singlet ground state is phosphorescence, which takes 10^{-4} to 10^{-1} seconds.
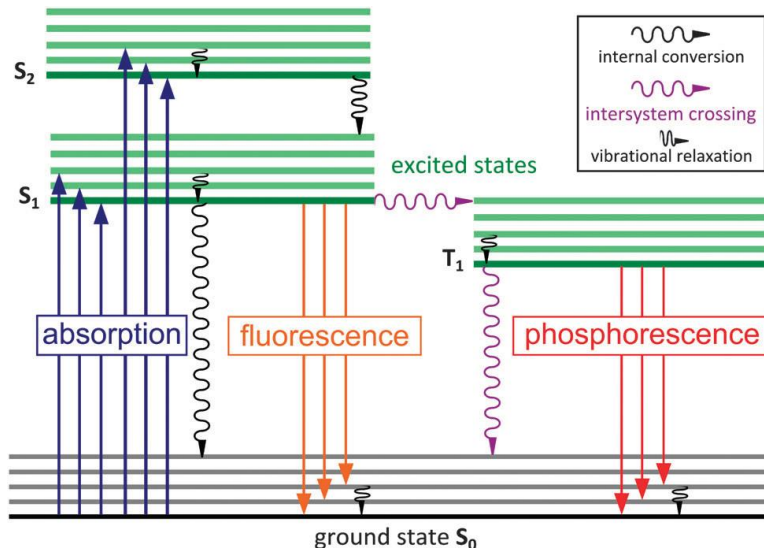
Figure 2.10 Jablonski diagram showing basic photophysical processes; S denotes singlet, T triplet states. (Taken from Ref.[156])

The fluorescence lifetime is the average time that a molecule remains in an excited state prior to returning to the ground state,[157] which is an intrinsic property of a fluorophore and therefore does not depend on the method of measurement.[158] There are two complementary techniques being used to determine the fluorescence lifetime: the time domain and the frequency domain.

In the time domain (Figure 2.11 (a)), the sample is excited by a short pulse of light and the intensity of the emission versus time is recorded, where the intensity of fluorescence emission decreases with time by an exponential function:

$$I(t) = I_0 \exp\left(-\frac{t}{\tau}\right) \hspace{5cm} (2.5)$$

where $I(t)$ is the fluorescence intensity measured at time t, I_0 is the initial intensity immediately after the excitation pulse, τ is the fluorescence lifetime, which is formally defined as the time in which the initial fluorescence intensity decays to $1/e$ of the initial intensity. However, fluorescence lifetime is often multiexponential, leading to complex curves. The typical technique of lifetime measurement is time-correlated single photon counting (TCSPC), which is based on the detection of single photons of a periodic light signal. The TCSPC simplifies the use of the time domain method. The fluorescence lifetime is calculated from the slope of the decay curve according to the equation 2.5.[158]
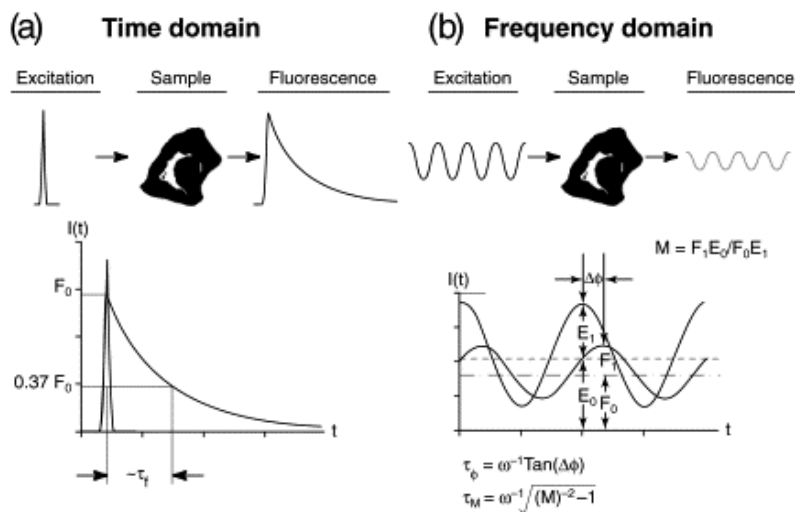
Figure 2.11 Methods of fluorescence lifetime measurement. (a) Time domain, (b) Frequency domain.(Taken from Ref. [159])

In the frequency domain (Figure 2.11 (b)), the sample is excited by sinusoidally modulated light. In this configuration, the emitting fluorescence occurs at the same frequency as the excitation light, but is modulated in depth M and shifted in phase $\Delta\varphi$,[159] which can be used to calculate the lifetime. For a single fluorescent species, the lifetime calculated from the phase (τ_φ) and modulation (τ_M) are equal. For more than one fluorescent species, the lifetime can be obtained from measurements of the phase and modulation lifetimes over variable frequencies.[160,161]

Herein, the fluorescence lifetime were carried out using TCSPC technique with light source of 458 nm and FluoroHub Single Photon Dection Module. The instrument response function (IRF) is evaluated using colloidal silica (Ludox) as scattering solution. For the SURMOF thin film, a Streak Camera System (Hamamatsu C4742) with a synchroscam sweep unit after excitation by the frequency doubled output (approximately 400 nm) of a Ti: Sapphire laser oscillator (Mira, Coherent Inc. 80 MHz repetition rate) was used.

2.8 Transient absorption spectroscopy (TAS)

To investigate fast processes, such as photophysical and photochemical reaction taking place on timescales ranging from tens of femtoseconds to a few nanoseconds, an ultrafast system with sufficiently good time resolution, which has been pushed into the femtosecond range, is needed. In this case, energy migration, the photo-induced electron transfer reactions and the key dynamical events, e.g. electron transfer process, charge-separated states, can be monitored in real time.[162] However, this can be achieved by a kind of time resolved method, transient absorption spectroscopy, also known as flash spectroscopy, which is an example of non-linear spectroscopy and measures changes in the absorbance in an excited system arising from changes in the electronic population of the excited levels.

Transient absorption spectroscopy (TAS) involves a pump-probe configuration in which a sample is promoted to an electronically excited state by an excitation pump pulse and the resulting changes in absorbance are monitored by a weak probe pulse with a delay time compared with the pump pulse (Figure 2.12). In a typical measurement, the temporal evolution of created transient species is recorded by measuring the absorption at different delay times between pump and probe pulses, which can be varied continuously by using an optical delay line. The incoming and transmitted intensities of the probe pulse are detected simultaneously for a range of wavelengths using a multichannel detection system.[163] In this fashion, any change in the absorption spectrum as a function of time and wavelength is obtained. The recording transient absorption reflects the dynamic processes occurring in the photosystem, such as ground state bleaching, further excitation of the excited electrons to higher excited states, stimulated emission or product absorption.
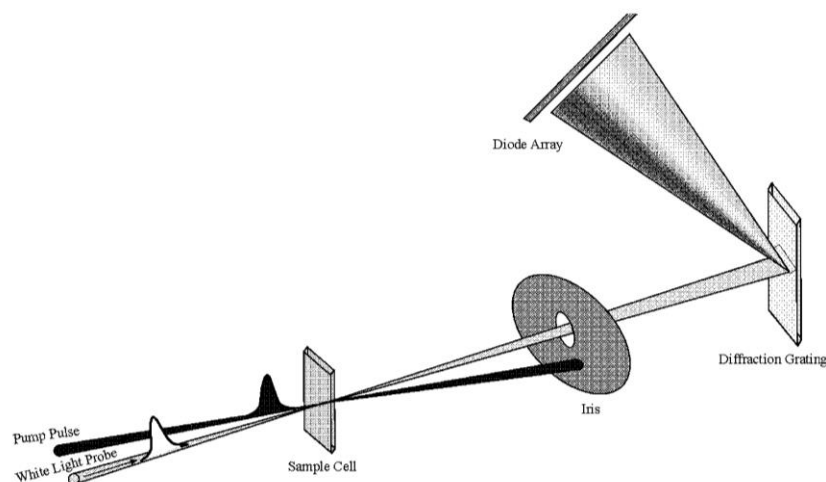
Figure 2.12 Schematic depiction of transient absorption spectroscopy principle. (Taken from Ref. [162])

In this thesis, transient absorption measurements were carried out by an amplified Ti: sapphire laser (Coherent LIBRA HE, 3.5 mJ, 1 kHz, 100 fs). The excitation beam was the frequency doubled fundamental at 400 nm and the excitation fluence was 15 μJ cm^{-2}. White light was generated for the probe pulse by focusing a portion of the fundamental into a 3 mm thick a c-cut sapphire window allowing the transient absorption to be measured from 450-800 nm. The pump-probe delay was obtained by delaying the pump pulse using a retroreflector mounted on a mechanical delay stage.

2.9 Flash-photolysis time-resolved microwave conductivity (FP-TRMC)

Flash-photolysis time-resolved microwave conductivity (FP-TRMC) is aimed to probe the change in conductivity on photoexcitation of inorganic-semiconductor/organic-antenna layers,[164] which is free of electrodes and requires low electric fields (≤100 V/cm). In this method, the change in conductivity within the sample is directly related to the amount of mobile electrons created in the conduction band of the semiconductor. It is sensitive to the charge carrier density and mobility.[165] Seki et al. have combined FP-TRMC and TAS techniques for simultaneous measurement of photo-induced changes in conductivity and charge carrier density in organic films, which provides an exact mobility value.[166]

Figure 2.13 shows the schematic representation of FP-TRMC system. A third harmonic of a Q-switched Nd:YAG laser is used to pump an optical parametric oscillator (OPO) yielding tunable

38

laser pulse (e.g. 200-2000 nm). A resonant cavity serves as an interaction site between the sample and microwave. The microwave circulator, microwave source and detector are enclosed in a Faraday cage. Under the microwave electro field, transient species produced by the pulsed excitation can affect the resonant frequency, resulting in microwave absorption.

The transient change in microwave power reflected by the cavity ($\Delta P/P$) is related to the photoinduced change in the conductance of the sample ($\Delta\sigma$) resulting from the formation of mobile charge carriers by:

$$\Delta\sigma = \frac{1}{A}\frac{\Delta P}{P} \tag{2.6}$$

where A is the sensitivity factor which can be derived from the resonance characteristics of the microwave cavity, sample geometry and the dielectric properties of the medium. The conductivity change is derived from transient charge carriers with a concentration N:

$$\Delta\sigma = e \sum \mu N \tag{2.7}$$

where e is the unit charge of a single electron and $\Sigma\mu$ is the sum of charge carrier mobilities. Based on Lambert-Beer's law, the relationship between the carrier distribution and the penetration depth of the light (z) is given by:

$$N(z) = \alpha ln10 \cdot 10^{-\alpha z} \cdot \varphi \cdot I_0 \tag{2.8}$$

where α is the linear absorption coefficient of the sample, I_0 is incident photon density of the excitation laser(photon cm^{-2}), φ donates a photocarrier generation yield. F_{light} is defined as a correction (or filling) factor (cm^{-1}) of the light, taking account of the electric field, the geometry and the cross-section of the laser pulse. Combining the above equations, the following expression for $\varphi \Sigma\mu$ is obtained:[166]

$$\varphi \sum \mu = \frac{1}{eAI_0F_{fight}} \cdot \frac{\Delta P}{P} \tag{2.9}$$

Flash-photolysis time-resolved microwave conductivity (FP-TRMC) measurements were performed under ambient atmosphere at room temperature, where the resonant frequency and microwave power were properly adjusted at 9.1 GHz and 3 mW, respectively. Charge carriers

were photochemically generated using a third harmonic generation (λ = 355 nm) of a Spectra Physics model INDI-HG Nd:YAG laser with a pulse duration of 5- 8 ns. The photon density of the 355 nm laser pulse was 4.6- 9.1 $\times 10^{15}$ photons cm^{-2} pulse^{-1}. The TRMC signal picked up by a diode (rise time < 1 ns) was monitored by a Tektronix model TDS 3032B digital oscilloscope.
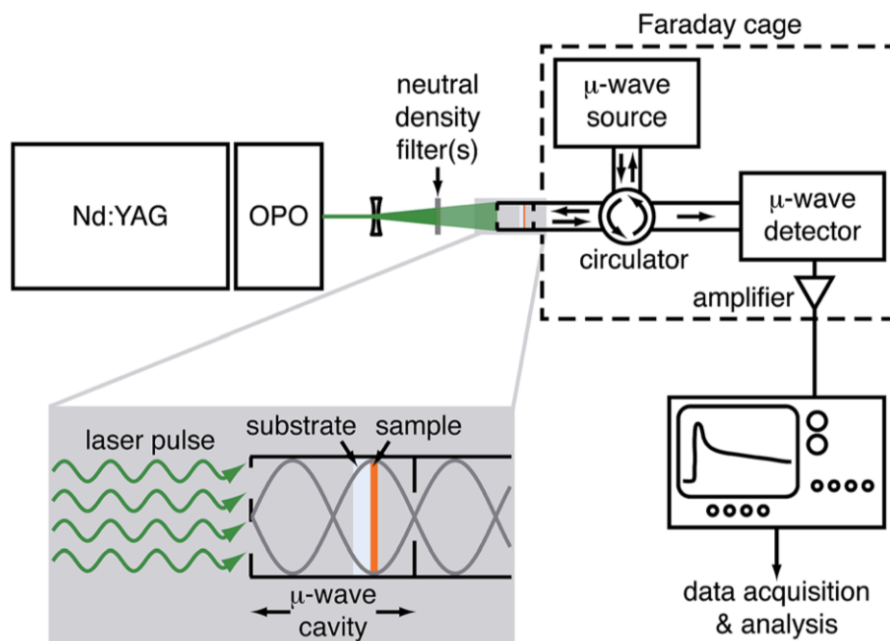
Figure 2.13 Schematic representation of the flash photolysis time-resolved microwave conductivity (FP-TRMC) system. (Taken from Ref.[165])

TAS measurements were carried out under ambient atmosphere at room temperature. The identical samples used for FP-TRMC measurement were also measured with TAS. The sample was photoexcited using the same light with the FP-TRMC. A white light continuum from a Xe lamp was used as a probe light source, which was guided into a Hamamatsu model C7700 wide-dynamic-range streak camera system, collecting a two-dimensional image of the spectral and temporal profiles of light intensity. The photocarrier generation yield (φ) was evaluated based on the observed photo-bleach of a porphyrin Q band. 1 μm-thick SURMOF films were used for FP-TRMC and TAS measurements.

3 Materials and experiments

3.1 Chemicals

5,15-diphenyl-10,20-di(4-carboxyphenyl)porphyrin (free base porphyrin) and Pd(II) 5,15-diphenyl-10,20-di(4-carboxyphenyl)porphyrin (Pd porphyrin) were purchased from Livchem Logistics GmbH and used without further purification. [5,15-Bis(*N*,*N*-diphenylamino)-10,20-bis(4-carboxyphenyl)porphyrinato]zinc(II) (DPA-Zn(II)porphyrin) and [5,15-Bis(4-carboxyphenyl)-10,20-diphenylporphyrinato]zinc(II) (Zn(II)porphyrin) were synthesized by the group of Prof. Hiroshi Imahori at Kyoto University. 5,15-diphenylazido-10,20-di(4-carboxyphenyl)porphyrin (N_3-porphyrin), trimethylolethane tripropiolate and cyclooctyne derivative were synthesized by the group of Prof. Dr. Stefan Bräse, Institute of Organic Chemistry (IOC), Karlsuhe Institute of Technology (KIT).

The iodine/tri-iodine acetonitrile solution (I^-/I_3^-, 50 µM, Iodolyte AN-50) was commercially obtained from SOLARONIX (Switzerland). (Poly(3,4-ethylenedioxythiophene)-poly(styrenesulfonate)) PEDOT/PSS (CLEVIOS™ PH 1000) liquid solution with a specific conductivity of 850 S/cm was purchased from Heraeus. Zinc acetate dihydrate, Copper acetate monohydrate, n-hexane, were purchased from Merck Millipore. 1,3,5-benzenetricarboxylic acid (BTC) was obtained from Alfa Aesar. C_{60}-fullerene, ferrocene (Fc), 16-mercaptohexadecanoic acid (MHDA, 97%), 11-mercapto-1-undecanol (MUD, 99%), toluene ($\geqslant$99.7%), acetonitrile ($\geqslant$99.8%), poly(methyl methacrylate) (PMMA) were purchased from Sigma-Aldrich (Germany). Absolute ethanol was purchased from VWR (Germany).

All the commercially available chemicals were used without further purification.

3.2 Substrates

Gold substrates were obtained from Georg Albert-Physical Vapor Deposition (Silz, Germany), one kind of which is deposited on Si wafers with 100 nm thickness and the other is deposited on mica substrates.[103] QCM sensors were purchased from LOT-ORIEL (UK). The sensors are Au coated with a diameter of 14 mm, a thickness of 0.3 mm and a resonance frequency of 4.95 MHz $\pm$ 50 kHz. The working electrode has a diameter of 10 mm.

The fluorine doped tin oxide (FTO) coated glass slides with a surface resistivity of ~10 Ω/sq were obtained from Sigma-Aldrich. The silicon substrates with a [100] orientation were obtained from Silicon Sense (US). The quartz glasses were purchased from Hellma Optics GmbH Jena (Germany). The glasses (microscopy slides) were obtained from VWR. These substrates were treated with plasma (Diener Plasma) under O_2 (50 sccm) for 30 min to remove the impurities and generated a surface with hydroxyl groups.

3.3 Preparation of SAMs

3.3.1 Preparation of MHDA SAMs on gold substrate

The gold substrate was immersed in a 20 µM MHDA solution (acetic acid/ ethanol solution, 1/9, v/v) for 3 days at room temperature, then rinsed with pure ethanol and gently dried under nitrogen flux to obtain the MHDA SAMs, shown as Figure 1.6.

3.3.2 Preparation of MUD SAMs on gold substrate

The gold substrate was immersed in a 1 mM MUD ethanolic solution for 24 h, then rinsed with pure ethanol and gently dried under nitrogen flux to obtain the MUD SAMs, shown as Figure 1.6.

The SAMs are usually prepared shortly before use.

3.4 Preparation of porphyrin SURMOFs

3.4.1 Preparation of free base porphyrin Zn-SURMOF 2 and Pd porphyrin Zn-SURMOF 2

The porphyrin-based SURMOF grown on various functionalized substrates were fabricated using the spraying method.[91] 1 mM zinc acetate ethanolic solution and 20 µM free base porphyrin or Pd porphyrin ethanolic solution were sequentially deposited onto the substrates for 15 s and 25 s in a layer-by-layer fashion. After waiting for 35 s to allow for further coordination, the samples were rinsed with ethanol to remove unreacted or byproducts species from the surface. The thickness of the samples was controlled by the number of deposition cycles.

3.4.2 Preparation of Zn(II)metalloporphyrin-based SURMOF

The preparation of DPA-Zn(II)porphyrin and Zn(II)porphyrin based Zn-SURMOF 2 was the same procedure as free base porphyrin Zn-SURMOF 2. 1 mM zinc acetate ethanolic solution and 20 µM porphyrin ethanolic solution were sequentially deposited onto the substrates for 15 s and

25 s in a layer-by-layer fashion. After waiting for 35 s to allow for further coordination, the samples were rinsed with ethanol to remove unreacted or byproducts species from the surface. The thickness of the samples was controlled by the number of deposition cycles.

3.4.3 Preparation of C_{60}-fullerene loaded porphyrin-based SURMOF

A concentration of 20 μM free base porphyrin and a tunable concentration of C_{60}-fullerene were prepared, where toluene/ethanol (1/20, v/v) was used as a mixed solvent. The concentration ratio of C_{60} and free base porphyrin could be tuned from 0.25 to 2. Similar to the porphyrin-based SURMOF, the loading of C_{60} into porphyrin-based SURMOF involved the layer-by-layer fashion. 1 mM zinc acetate ethanolic solution and the free base porphyrin/C_{60} mixture solution were sequentially deposited onto the substrates for 15 s and 25 s. After waiting for 35 s to allow for further coordination, the samples were rinsed with ethanol to remove unreacted or byproducts species from the surface. The thickness of the samples was controlled by the number of deposition cycles.

3.5 Preparation of porphyrin SURGEL

3.5.1 Preparation of azido-porphyrin SURMOF

The N_3-porphyrin SURMOF was prepared similar to other porphyrin SURMOFs on MHDA SAM functionalized Au surfaces. 1 mM zinc acetate ethanolic solution and 20 μM N_3-porphyrin ethanolic solution were sequentially deposited onto the substrates for 15 s and 25 s in a layer-by-layer fashion. After waiting for 35 s to allow for further coordination, the samples were rinsed with ethanol to remove unreacted or byproducts species from the surface. The thickness of the samples was controlled by the number of deposition cycles.

3.5.2 Preparation of porphyrin SURGEL via cross-linking of azido-porphyrin SURMOF

The porphyrin SURGEL was prepared following the literature.[104] First, freshly prepared samples of N_3-porphyrin SURMOF were immersed in a solution of toluene containing 1mg/mL trimethylolethane tripropiolate (cross-linker). The samples were then heated in the solution for 7 d in dark at 80 ℃ under a nitrogen atmosphere, forming cross-linked porphyrin SURMOF. After thoroughly rinsed with acetone and ethanol and dried under nitrogen flow, the cross-linked SURMOF samples were immersed in 10 mL ethanol/water 1/1 (volume) containing 1 mg ethylene diaminetetraacetic acid (EDTA) to remove the metal ions. After 30 min immersion at

room temperature, the samples were rinsed thoroughly with ethanol and water and dried under nitrogen flow and the SURGEL was obtained.

3.6 Preparation of HKUST-1 on QCM-sensor

HKUST-1 thin film grown on MHDA SAMs functionalized QCM-sensors were performed in a layer-by-layer fashion employing the spraying method. 1 mM copper acetate ethanolic solution and 0.2 mM 1,3,5-benzenetricarboxylic acid (BTC) ethanolic solution were alternately sprayed on the target substrate for 15 and 25 s, respectively. After waiting for 35 s to allow for further coordination, the samples were rinsed with ethanol to remove excess compounds. The repetition of the procedure produced thick film.

4 Porphyrin-based SURMOFs and photophysical properties

4.1 Photoinduced charge-carrier generation in porphyrin SURMOF

4.1.1 Background

The design of MOF materials is inherently flexible, and recently, the substitution of the organic struts with organic chromophores has attracted considerable attention because of their ubiquity in nature systems. Porphyrins and its' derivatives afford great potential as building blocks in the construction of coordination polymers for versatile applications resulting from their central role in the metabolism of living organisms, e.g. in the process of photosynthesis.[126,130] More recently, numerous "artificial or human-made" porphyrins based metal-organic frameworks have been fabricated and demonstrated to be used as artificial light-harvesting antennae to understand the aspect of the exciton migration in porous metal-organic frameworks.[167]

The conventional solvothermal synthesis of porphyrin-based metal-organic frameworks encountered a challenging problem that the metal precursors (metal ions) will not only take part in constructing the MOF structure but also be inserted into the cores of porphyrin units forming metalloporphyrin complexes, which leads to the intergrowth in metal-organic frameworks. The intergrown structure will decrease the pore volume and limit the further application towards gas adsorption and metal ions separation with these materials. On the other hand, the studies regarding porphyrin-based MOF thin films are quite rare.

Thus, highly ordered and oriented porphyrin-based SURMOFs with pronounced photoconductivity upon illumination were prepared using a liquid phase epitaxy deposition method in this part. The molecular structure of the porphyrins used in this part are shown in Figure 4.1, named free-base porphyrin and Pd porphyrin. The obtained free base porphyrin and Pd porphyrin SURMOF adopt AA stacking arrangement without intergrowth in MOF material with the layers perpendicular to the substrate. The layer distances of both are about 0.6 nm (Figure 4.2).This kind of ordered structure is crucial for energy transfer within the material and allows for the investigation of structure-property relationships. More importantly, it demonstrates the use of highly orientated and ordered porphyrin-based SURMOF as a platform in the application of light harvesting and conversion of solar energy.
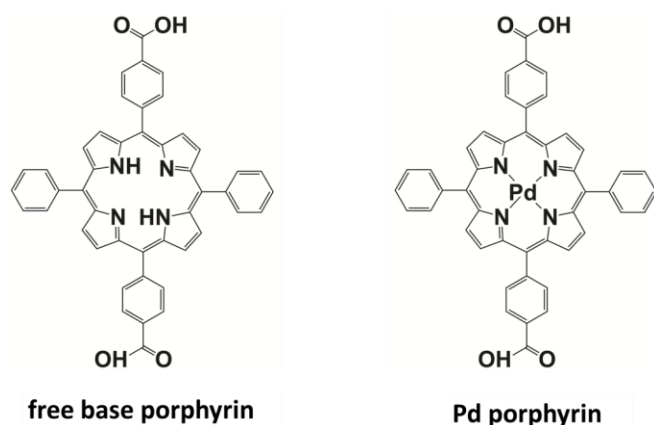
Figure 4.1 Molecular structure of (a) free base porphyrin (b) Pd porphyrin
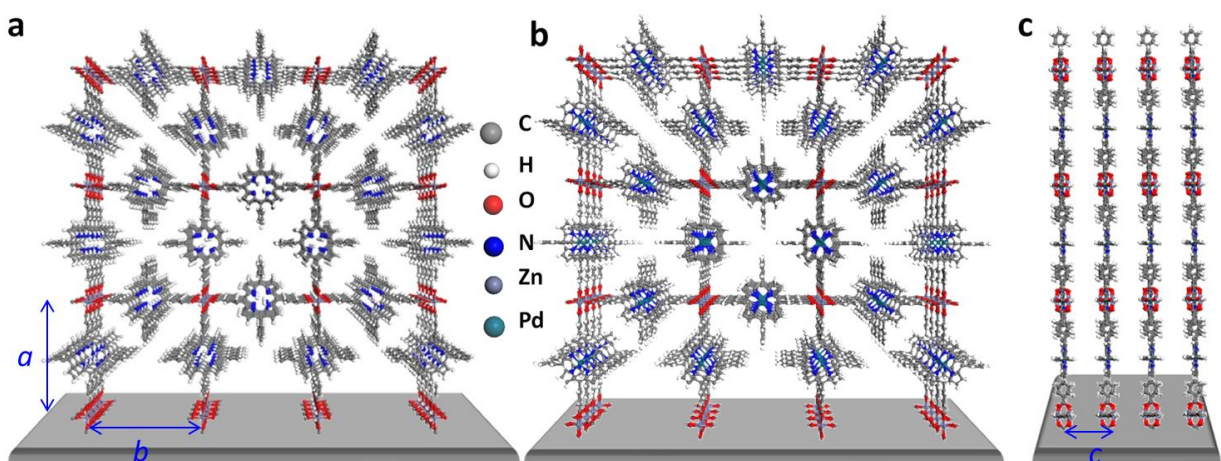
Figure 4.2 Proposed structure of (a) free base porphyrin Zn-SURMOF 2 (b) Pd porphyrin Zn-SURMOF 2 with parallel 1-D channels and (c) layers perpendicular with a layer distance about 0.6 nm.

4.1.2 Characterization of the porphyrin-based Zn-SURMOF 2

The free base porphyrin and Pd porphyrin Zn SURMOF 2 with zinc acetate as a metal source were deposited on various substrates, such as SAMs assembled on Au surfaces, FTO, Si and quartz, using spray method were described in detail as Chapter 3.4.1.

The out-of-plane XRD data of free base porphyrin and Pd porphyrin Zn-SURMOF 2 fabricated on various substrates are shown in Figure 4.3. Both SURMOFs are highly crystalline and oriented along [001] orientation on these substrates.
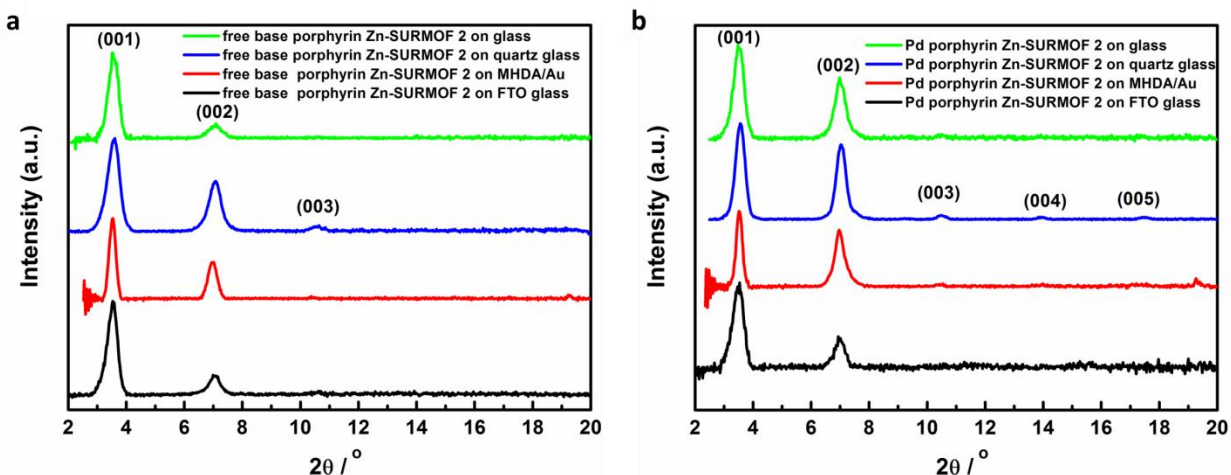
Figure 4.3 Out of plane XRD of (a) free base porphyrin Zn-SURMOF 2 and (b) Pd porphyrin Zn-SURMOF 2 fabricated on different substrates
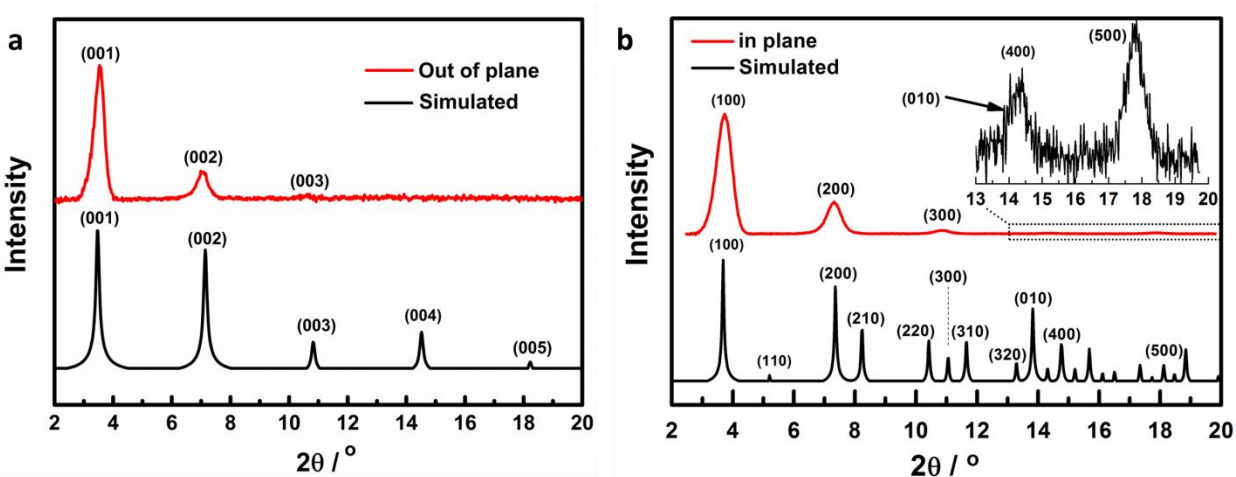
Figure 4.4 (a) Out of plane and simulated with preferred [001] orientation and (b) in plane and simulated XRD data of free base porphyrin Zn-SURMOF 2 grown on FTO substrate

Hereafter the free base porphyrin Zn-SURMOF 2 grown on FTO substrate was taken as an example for further structure analysis. The lattice parameter in the direction perpendicular to the surface (*a*) is determined from the diffraction peak (001) at $2\theta = 3.7°$ with a value of 2.4 nm, resulting from the out of plane data (Figure 4.4 (a)). The lattice parameter in the direction parallel to the surface (*b*) is determined from the diffraction peak (100) at $2\theta = 3.7°$ with a value of 2.4 nm, resulting from the in plane data (Figure 4.4 (b)). The inset is the magnification of the range from 13° to 20°, which gives the shoulder peak at $2\theta = 13.9°$ close to the (400) peak

corresponding to the layer distance (*c*) with a value of 0.64 nm. The parameters fit very well with the calculated values described later in this chapter.

The IRRA spectra of free base porphyrin and Pd porphyrin Zn-SURMOF 2 grown on MHDA SAMs/Au substrates are shown in Figure 4.5 (a). The difference of both samples occurs in lower wavenumber, where 964 cm^{-1} in free base porphyrin Zn-SURMOF 2 are attributed to the vibration of N-H. This N-H band vanished and a new band appeared at 1012 cm^{-1}, which is attributed to the vibration of N-Pd. The broad band centered at 1595 cm^{-1} and 1405 cm^{-1} for both samples are attributed to the asymmetric and symmetric stretching of COO$^-$ groups, respectively. The difference (Δv_{COO}-) of ~200 cm^{-1} indicates the formation of a perfect zinc paddle-wheel structure with bidentate bridging bonding.[168,169]

Table 4.1 UV-Vis data for free base porphyrin and Pd porphyrin in ethanol, free base porphyrin Zn-SURMOF 2 and Pd porphyrin Zn-SURMOF 2 grown on quartz glass substrate.

Compound		Soret band (nm)		Q bands (nm)			
				I	II	III	IV
Solution	free base porphyrin	415		512	547	590	646
	Pd porphyrin	414		522	554		
Thin films	free base porphyrin Zn-SURMOF 2	380	438	526	561	597	654
	Pd porphyrin Zn-SURMOF 2	381	439	533	565		

Due to the special absorption properties of porphyrin as a result of its' highly conjugated π-electron system, the UV-Vis spectrum of porphyrin consists of two characteristic features: Soret bands, resulting from the transition from the ground state to the second excited state (S0→S2), with a typical absorption range between 380 nm - 500 nm; Q bands, resulting from the transition from the ground state to the first excited state (S0→S1), with a typical absorption range between 500 nm - 750 nm. The UV-Vis spectra of free base porphyrin and Pd porphyrin in ethanol solution are shown in Figure 4.5 (b) and the spectra of the corresponding SURMOFs grown on quartz substrates are shown in Figure 4.5 (c). The detailed data are listed in Table 4.1. The Soret bands of both SURMOFs split into two bands at ~ 380 nm and ~ 438 nm after the formation of SURMOFs onto quartz glass, which is due to the formation of densely packed porphyrins.[170] The small redshifts observed for both porphyrin SURMOFs on quartz glass with a value of ~25

nm compared with the Soret band of the corresponding porphyrin in ethanol result from the expanded π-conjugation of the porphyrins constructed into the highly oriented and ordered SURMOF structure.[171] The decrease of two Q bands for the Pd porphyrin Zn-SURMOF 2 compared to the four Q bands observed for the free base porphyrin Zn-SURMOF 2 clearly suggests that the porphyrin macrocycle is chelated with Pd(II) ions leading to the formation of higher D_{4h} symmetric inner nitrogen atoms in porphyrin macrocycles.
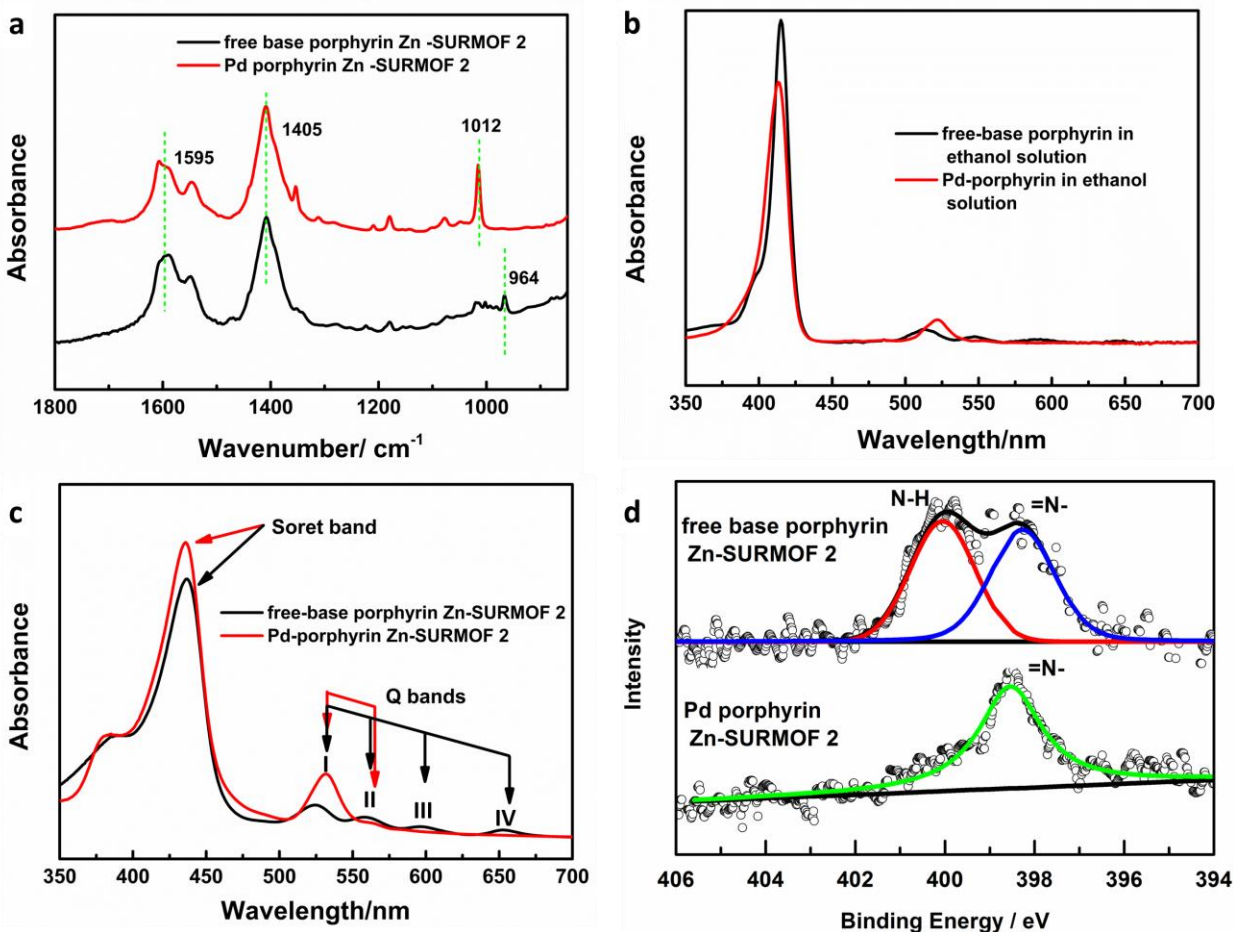
Figure 4.5 (a) The IRRA spectra of free base porphyrin and Pd porphyrin Zn-SURMOF 2 grown on MHDA SAMs/Au substrates. (b) The UV-Vis spectra of free base porphyrin and Pd porphyrin in ethanol solution. (c) The UV-Vis spectra of free base porphyrin and Pd porphyrin Zn-SURMOF 2 grown on quartz substrates. (d) The XPS spectra of free base porphyrin and Pd porphyrin Zn-SURMOF 2 grown on MHDA SAMs/Au substrates.

The similar situation is observed in the XPS data of free base porphyrin and Pd porphyrin Zn-SURMOF 2 grown on MHDA SAMs/Au substrates (Figure 4.5 (d)). Using XPS, the N1s binding energy was obtained, which provides the possibility to distinguish free base porphyrin and metalloporphyrin due to the replacement of freebase proton by metal ions, which lead to the change of charge distribution of the N atoms. The XPS data were fitted with a fixed full width at half maximum (FWHM) value 1.7 eV. The N1s peaks appeared at 399.9 eV and 398.2 eV for Zn-porphyrin SURMOF are attributed to the N-H and =N- of the free-base porphyrin units.[172] The replacement of the two protons in free base porphyrin SURMOF 2 with Pd(II) ions increases the symmetry from D2h to D4h, and the four nitrogen atoms become equivalent and exhibit a single metal-nitrogen peak at 398.6 eV for Pd porphyrin Zn-SURMOF 2.[172]

Morphology

2 µm   **2 µm**

← SURMOF →
← FTO →
1 µm   ← Glass →   **1 µm**

(a) Free base porphyrin Zn-SURMOF 2   **(b) Pd porphyrin Zn-SURMOF 2**
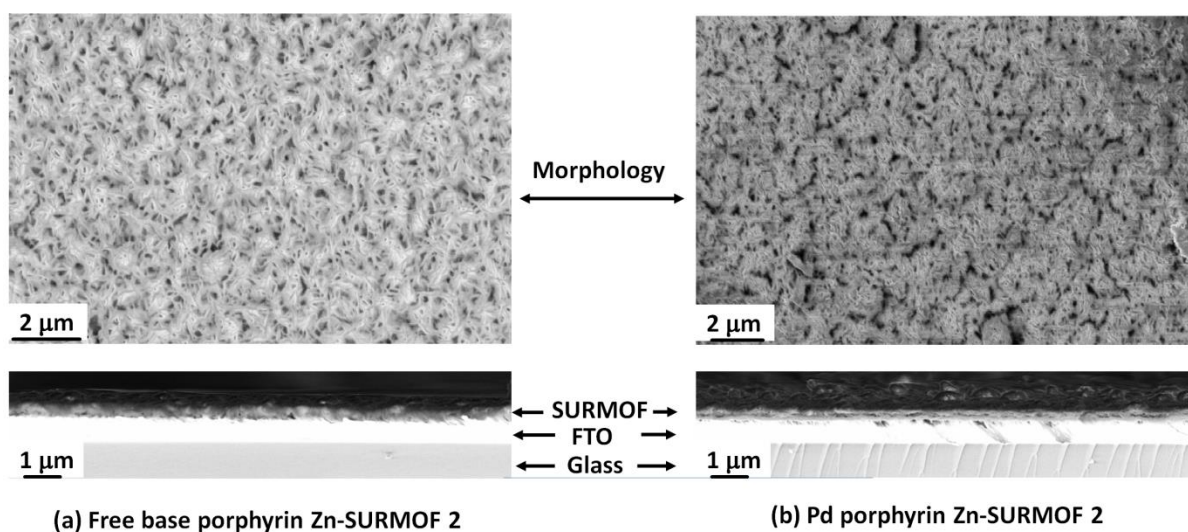
Figure 4.6 Top view and cross-section SEM images of (a) free base porphyrin Zn-SURMOF 2 and (b) Pd porphyrin Zn-SURMOF 2 grown on FTO substrates.

The morphology of free base porphyrin and Pd porphyrin Zn-SURMOF 2 grown on FTO substrates with 30 spraying cycles is shown in Figure 4.6, as well as the cross-section images. From the top view, the thin films seem quite compact and homogeneous. From the cross-section, the thickness of the SURMOF films is determined to be ~300 nm corresponding to 30 cycles, e.g. 10 nm for each spraying cycle. In addition, the photographs of both thin films on FTO with different thicknesses are displayed in Figure 4.7. Evidently, with increasing thickness color intensified. The metallization makes a remarkable color change compared with the free base

porphyrin, which can also be confirmed by the transformation of UV-Vis spectrum especially in the range of Q bands.
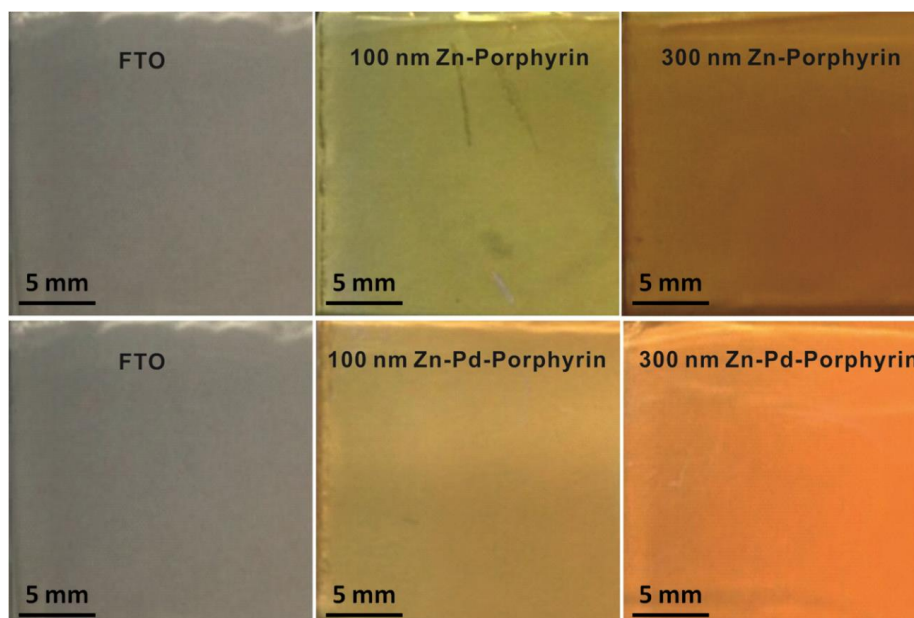
Figure 4.7 Photographs of free base porphyrin (top) and Pd porphyrin Zn-SURMOF 2 (bottom) grown on FTO with different thicknesses.

4.1.3 Photocurrent measurements

In order to study the effect of light illumination on the conductivity, the photocurrent response of the porphyrin-based SURMOF was measured under the illumination of light. The photocurrent measurements were carried out with an electrochemical workstation (Palm Instruments) in a 50 µM iodine/triiodine solution (I^-/I_3^-) by using a three-electrode system as shown in Figure 4.8. The FTO glass assembled with the porphyrin-based MOF film was used as the working electrode (WE), a Pt coated FTO substrate as counter electrode (CE), and a Pt wire as the reference electrode (RE). The distance between the working electrode and the counter electrode is 1 cm. The samples with an active area of 0.79 cm^{-1} were illuminated under a fiber coupled LEDs system (Prizmatix Ltd., 530 nm). The output power is different for different wavelength, e.g. 112 mW for LED 365 nm, 65 mW for LED 400 nm, 135 mW for LED 455 nm, 55 mW for LED 530 nm and 102 mW for LED 640 nm, which were measured using Ophir Nova II power meter with PD-300-UV sensor.

51
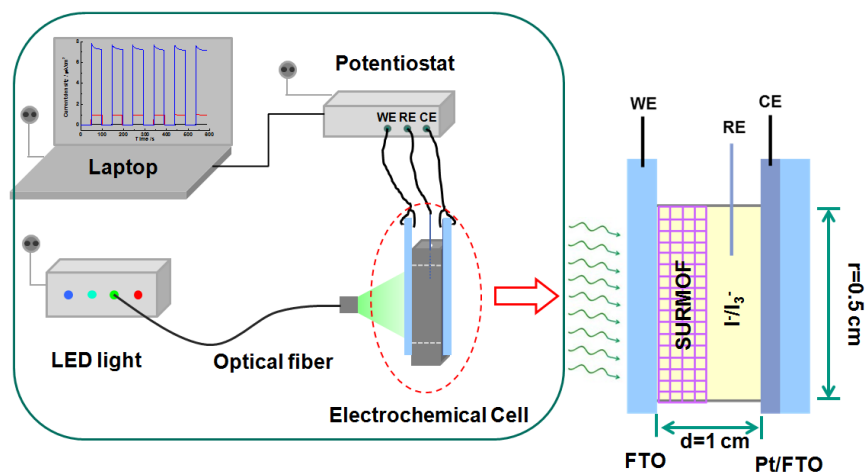
Figure 4.8 Schematic drawing of photoelectrochemical setup equipped with three-electrode cell and LED light system for photocurrent measurement.

The photocurrent was obtained when the light was switched on with an applied bias voltage of 0.06 V vs Pt wire electrode, which shows no dramatic influence on the photocurrent from the bare FTO substrate as shown in Figure 4.9. The photocurrent response under the illumination of different wavelength light, on- off response under illumination of 530 nm and the durability for 30min of free base porphyrin Zn-SURMOF 2 and Pd porphyrin SURMOF 2 are displayed in Figure 4.9. The figures on the left side are for free base porphyrin Zn-SURMOF 2 and on the right side are for Pd porphyrin SURMOF 2, respectively. The Pd porphyrin SURMOF 2 exhibits larger photocurrent than the free base porphyrin Zn-SURMOF 2. Overall, the generated photocurrents follow the absorption of the porphyrin chromophores (Figure 4.5(b)). Both samples exhibit fast response and have a maximum photocurrent at 400 nm. The thicker films generated higher photocurrent than the thin film thickness for both SURMOFs in the studies, resulting from more materials deposited on the substrates.
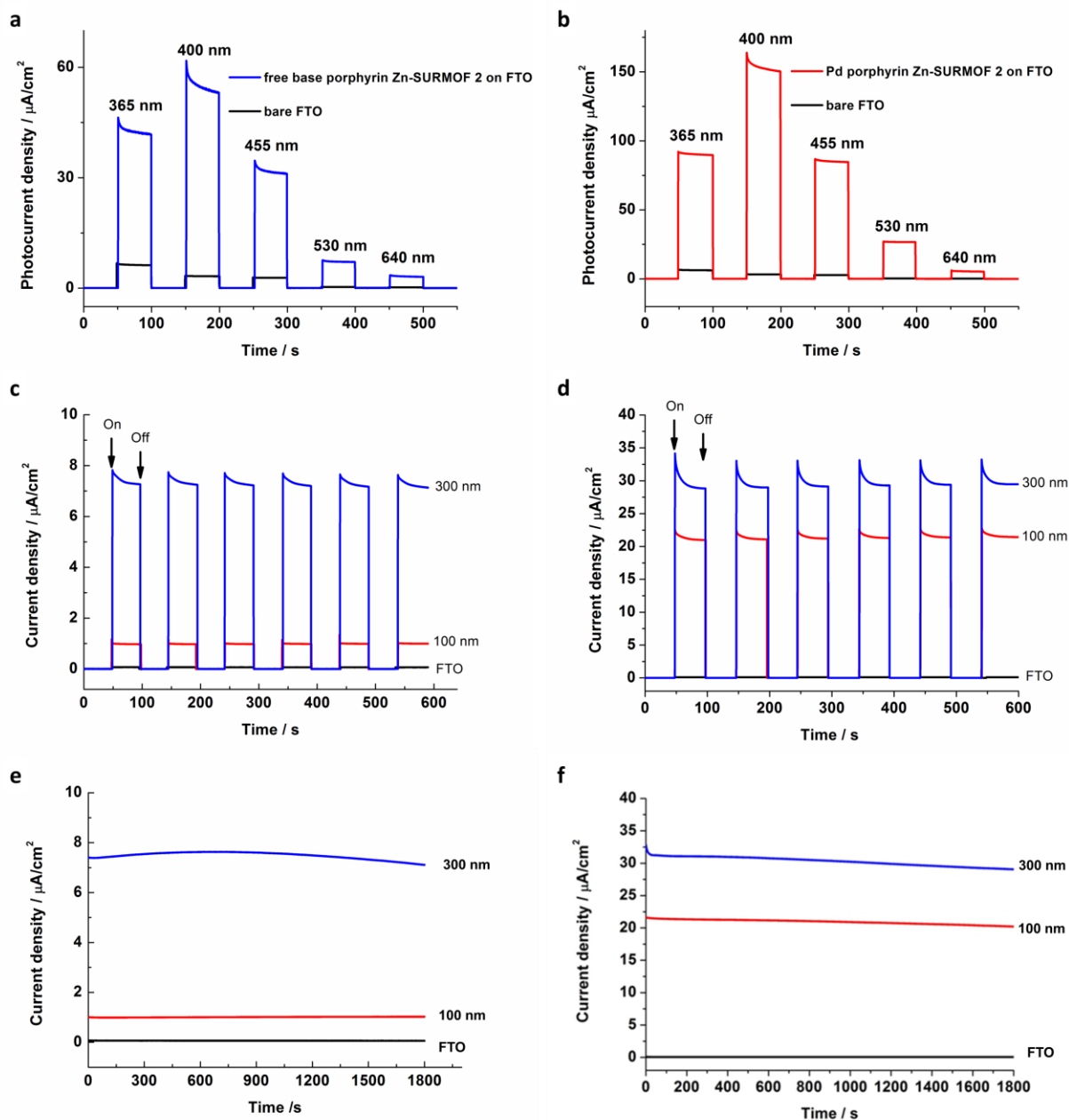
Figure 4.9 Photocurrent response under illumination of different wavelength light (a)(b), on- off response under illumination of 530 nm (c)(d) and the durability for 30min (e)(f) of free base porphyrin Zn-SURMOF 2 (left) and Pd porphyrin SURMOF 2 (right)

After the illumination for 30 min, no obvious decrease of the generated photocurrent is observed, confirming the stability of the thin films, which can also be proved by QCM-D (Figure 4.10 (a)). Here, the free base porphyrin SURMOF 2 which was prepared on QCM-sensor was taken as an

example. After the air flow over the sample, the pure acetonitrile solution was injected, following by I^-/I_3^- electrolyte (in acetonitrile). The obtained Δf = ~80 Hz for acetonitrile and Δf = ~ 40 Hz for I^-/I_3^- and nearly vertical slopes suggest the very fast diffusion of acetonitrile and I^-/I_3^- into the materials. The dissipation signal in red provide with information about the mechanical properties of the deposited film. The obtained very small dissipation factor ($\Delta D = 1.5\times10^{-6}$) after injection of acetonitrile and I^-/I_3^- solutions show that the deposited free base porphyrin Zn-SURMOF 2 on QCM sensor is very rigid and stable in these solutions. The out of plane XRD data of the free base porphyrin SURMOF 2 after the injection of acetonitrile and I^-/I_3^- electrolyte solutions is shown in Figure 4.10 (b). The existence of (001) and (002) diffraction peaks after injection of acetonitrile and I^-/I_3^- electrolyte suggests the high stability of the free base porphyrin Zn-SURMOF 2 in these solutions.
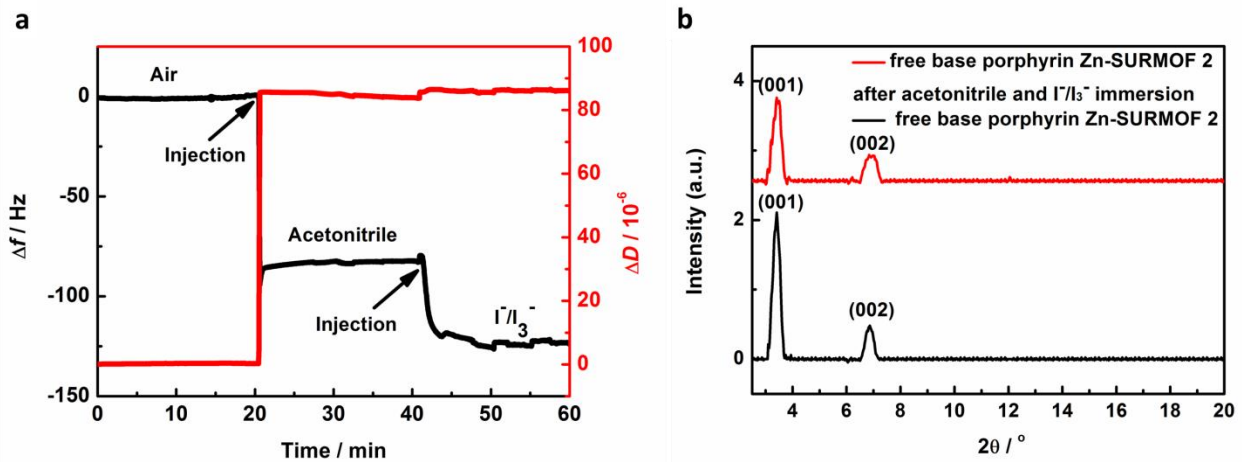
Figure 4.10 (a) QCM-D signals and (b) out of plane XRD data obtained for the free base porphyrin Zn-SURMOF 2 grown on QCM sensor after injection of pure acetonitrile solution and I^-/I_3^- electrolyte.

4.1.4 Photovoltaic performance

The photovoltaic devices have been designed to convert solar energy to electrical energy. The most common parameter to determine the performance of the photovoltaic devices is the power conversion efficiency (η), which is the ratio of the maximum power generated by the solar cell to the incident radiant energy and expressed as following:

$$\eta = \frac{V_m J_m}{P_{in}} = FF \frac{V_{oc} J_{sc}}{P_{in}} \tag{4.1}$$

Where J_m and V_m represent the voltage and current density corresponding to the maximum power P_m delivered by the solar cell, P_{in} is the incident photon flux (in W cm^{-2}), V_{OC} donates open-circuit voltage and J_{SC} donates short-circuit current density, The fill factor, FF, is defined by the quotient of maximum power and product of open-circuit voltage and short-circuit current, expressed by equation 4.2:

$$FF = \frac{P_m}{V_{oc}J_{sc}} = \frac{V_m J_m}{V_{oc}J_{sc}} \tag{4.2}$$

The porphyrin-based photovoltaic device was assembled as FTO/SURMOF/ (I$^-$/I$_3^-$)/Pt/FTO (Figure 4.11 (a)). Free base porphyrin Zn-SURMOF 2 and Pd porphyrin Zn-SURMOF 2 with a thickness of about 300 nm and area of 0.25 cm^2 (5 mm $\times$ 5 mm) was sprayed on FTO glass substrate and used as the photoelectrode. Pt coated FTO substrate with a hole (1 mm diameter) was used as the counter electrode. I$^-$/I$_3^-$ electrolyte was chosen as the top electrode. To make the photovoltaic device, the porphyrin-based SURMOF electrode and Pt-counter electrode were assembled in a sandwich architecture and sealed with a 20 μm thick hot-melt gasket as a spacer. A drop of electrolyte was put on the hole in the back of the counter electrode, which was introduced into the cell via vacuum backfilling. The hole in the counter electrode was sealed by a film of Meltonix 1170-25PF.

The photovoltaic performance of the assembled cells were studied by photocurrent density-photovoltage (J-V) characterization using an electrochemical analyzer (2600 series, Keithley Instruments, Germering, Germany) under illumination using AM 1.5 solar simulator (LS0308, LOT-Oriel Group Europe, Darmstadt, Germany). The measurement under illumination was performed without a mask, due to a clearly defined anode area of 25 mm^2. The incident light intensity was calibrated to 100 mW cm^{-2} with a silicon reference cell (RR- 187-O, Rera Solutions, the Netherland).

Figure 4.11 (b) shows current density-voltage (J-V) curve recorded for a free-base porphyrin Zn-SURMOF 2 (in black) and Pd porphyrin Zn-SURMOF 2 (in red) based photovoltaic devices under illumination with artificial sunlight. An analysis of the data shown in Figure 4.11 (b) yields an open circuit voltage of 0.57 V, a short-circuit current density of 0.45 mA cm^{-2}, a fill factor of 0.55 and an efficiency of 0.2% according to the equation above. Using the simplest

modification strategy, adding a Pd atom into the center of this polycyclic compound, already more than doubles the efficiency achieved to a yield of 0.45%, with an open-circuit voltage of 0.7 V, a short circuit current density of 0.71 mA cm^{-2} and a fill factor of 0.65. For a single-component organic photovoltaic simply sandwiched between two electrodes such a solar cell performance is rather impressive.
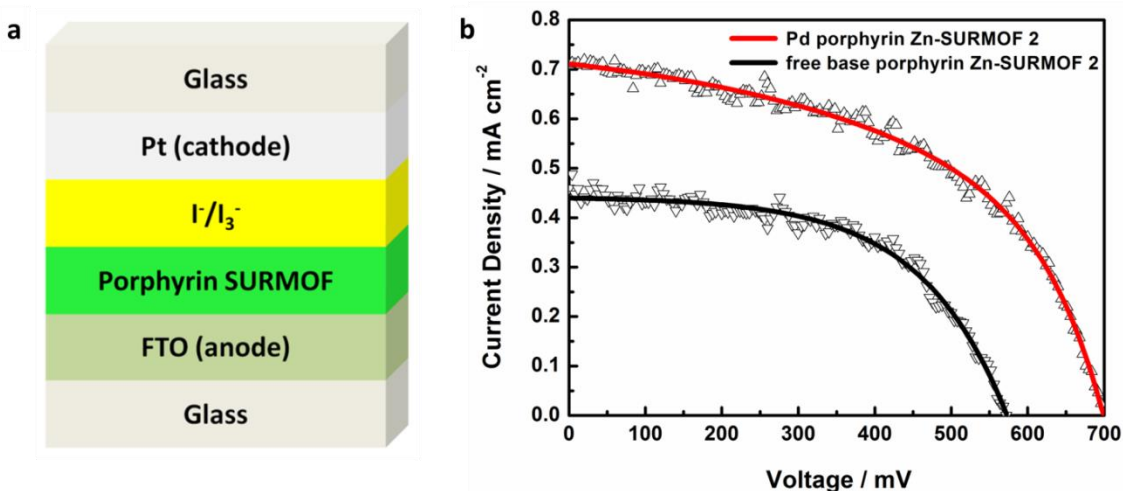
Figure 4.11 (a) Architecture of porphyrin-based SURMOF assembling photovoltaic device. (b) Photocurrent versus voltage (J-V) characteristics for freebase porphyrin Zn-SURMOF 2 and Pd porphyrin Zn-SURMOF 2 based photovoltaic device under illumination of AM 1.5 G simulated solar light (100 mW cm^{-2}) with liquid electrolyte (I$^-$/I$_3^-$) and active area 0.25 cm^2.

4.1.5 Photophysical properties

To explore the impressive photovoltaic performance of the porphyrin-based SURMOF, the intrinsic charge-carrier transport property as well as carrier generation efficiency within the well-defined SURMOF thin layers were investigated by a flash-photolysis time-resolved microwave conductivity (FP-TRMC) system coupled with transient absorption spectroscopy (TAS). Both the free base porphyrin Zn-SURMOFs 2 and Pd porphyrin Zn-SURMOFs 2 showed typical transient conductivity ($\varphi \Sigma\mu$) upon photoexcitation at 355 nm with a photon density of 4.6×10^{15} photons cm^{-2} pulse^{-1} (Figure 4.12 (a) (b)). Transient absorption spectra of both samples were recorded at ca. 0.2 μs after photoexcitation at 355 nm (Figure 4.12 (c) (d)). The photon density was 9.1×10^{15} and 4.6×10^{15} photons cm^{-2} pulse^{-1} for free base porphyrin SURMOF 2 and Pd porphyrin Zn-SURMOF 2, respectively. It is obvious that they displayed transient absorption and

photo-bleaching in their Q bands region, which indicates the photo-generation of porphyrin radical cations (holes). Based on the measurements, the charge carrier generation efficiency (φ) amounted to be 5.0×10^{-2} and 9.5×10^{-2} for the free base and Pd systems, respectively. The remarkably high OPV-performance for the Pd system is attributed to the high photocarrier generation efficiency ($\varphi = 9.5 \times 10^{-2}$) of this MOF-material. Such high efficiencies have not yet been reported for organic materials, the largest values reported to date for other MOFs materials[173] or porphyrin-based covalent organic frameworks (COFs)[174,175] amount to around 10^{-4}, almost three orders of magnitude smaller than the present value.
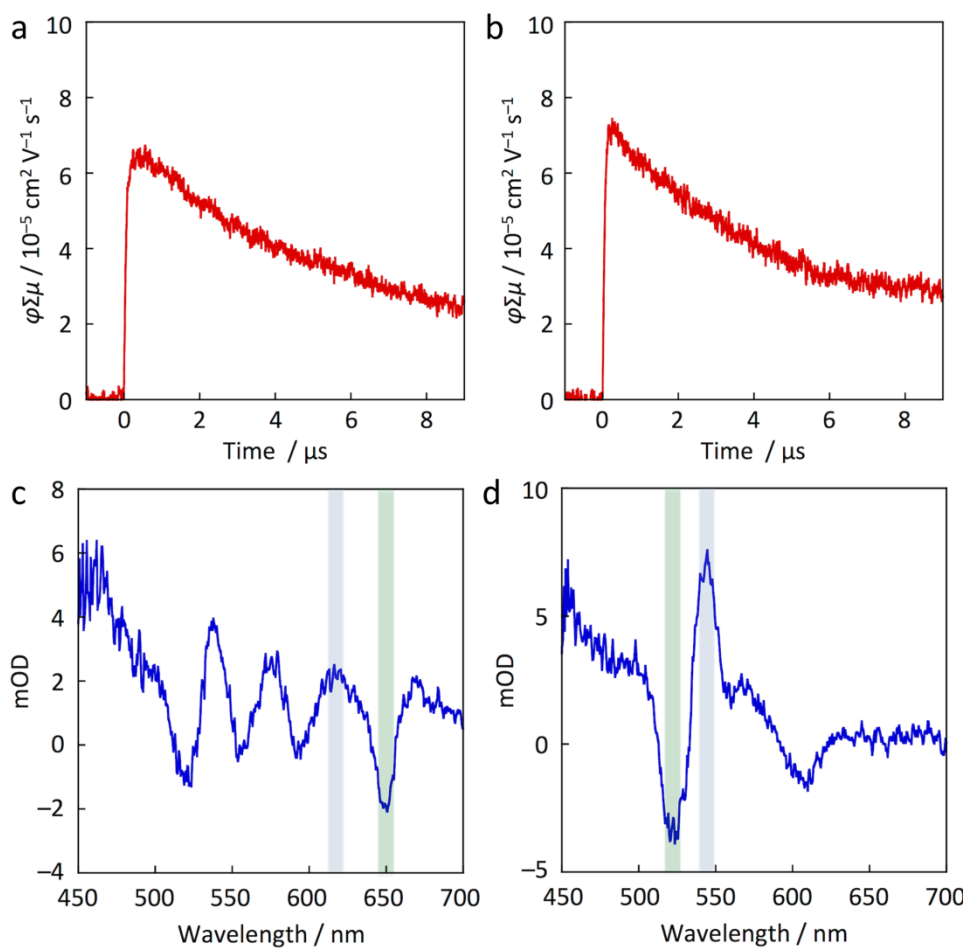
Figure 4.12 FP-TRMC profiles (a) (b) and transient absorption spectra (c) (d) of free base porphyrin SURMOF 2 (left) and Pd porphyrin Zn-SURMOF 2 (right) upon photoexcitation at 355 nm.

The FP-TRMC and transient absorption profiles at 620 nm and 650 nm of free base porphyrin SURMOF 2 as well as the FP-TRMC profiles and transient absorption profiles at 540 nm and 520 nm of Pd porphyrin Zn-SURMOF 2 were normalized as Figure 4.13. Since the kinetic profiles in FP-TRMC and TAS were well correlated, it was possible to determine the local-scale charge-carrier mobility for holes in the SURMOFs. The resulting values, 0.003- 0.004 cm^2V^{-1} s^{-1} for free-base porphyrin Zn-SURMOF 2 and 0.002 cm^2V^{-1} s^{-1} for Pd porphyrin Zn-SURMOF2, are large compared to those reported for another MOF, MIL-125(Ti),[176] with ~ 10^{-5} cm^2V^{-1} s^{-1}, but slightly smaller than those reported for a tetrathiafulvalen-based MOF structure (0.2 cm^2V^{-1} s^{-1}).[173]
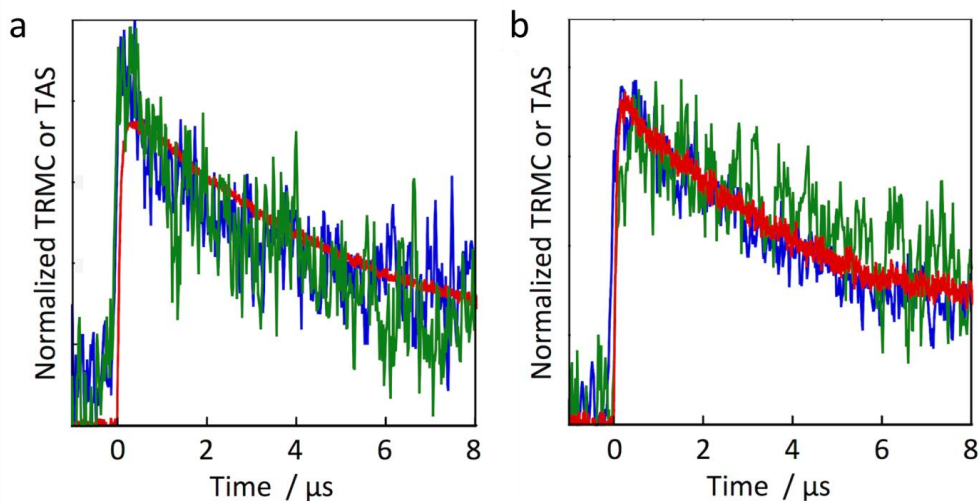
Figure 4.13 (a) Normalized FP-TRMC (red) and transient absorption profiles at 620 nm (blue) and 650 nm (green) of free base porphyrin SURMOF 2. (b) Normalized FP-TRMC profiles (red) and transient absorption profiles at 540 nm (blue) and 520 nm (green) of Pd porphyrin Zn-SURMOF 2.

Regarding to the photocurrent measurement of the porphyrin-based SURMOF (Figure 4.9), it is demonstrated a pronounced dependence of photocurrent on SURMOF thickness. When the thickness increases from 100 nm to 300 nm an increase of 150% for the free base SURMOFs and of 75% for the Pd porphyrin SURMOF is observed. This strong positive correlation suggests that the exciton diffusion length in the porphyrin-based SURMOFs must be on the order of several 100 nm. The observation of such large exciton diffusion lengths on the order of 20 nm has

already been reported earlier for quasi-periodic nematic packings of the porphyrin units (Figure 4.14 (a)).[177]
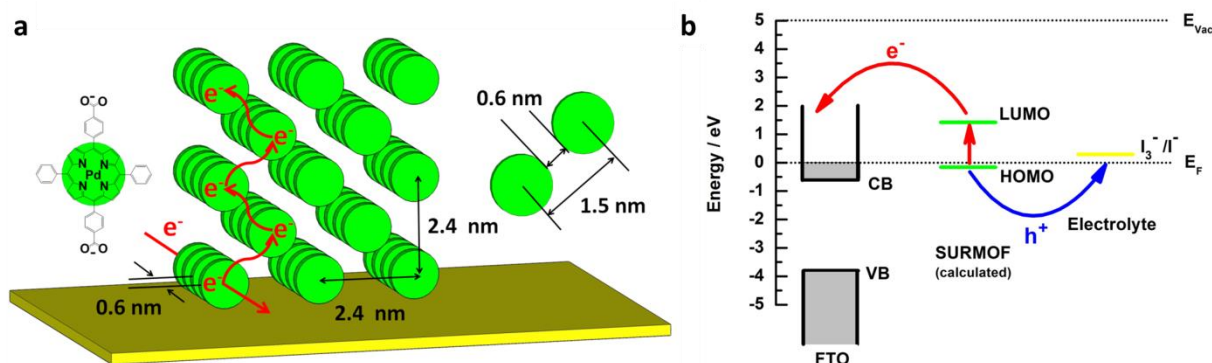
Figure 4.14 (a) Nematic stacking of porphyrin units in porphyrin SURMOFs, the paddle-wheels are omitted for the purpose of clarity. (b) Schematic description of photons absorption and excitons separation process in a porphyrin SURMOF photovoltaic device. The energy value of iodine/triiodine electrolyte in acetonitrile was taken from Ref.[178]. E_F = Fermi level

This hypothesis is fully supported by time-resolved photoluminescence of free base porphyrin Zn-SURMOF 2 and Pd porphyrin Zn-SURMOF 2 (Figure 4.15 (a)), showing fast quenching of singlet exciton populations. The y-axis (PL) is integrated between 650-750 nm and 550-650 nm for free base and Pd porphyrin SURMOF respectively. The data shows that the singlet exciton lifetime is very short in both free base- and Pd- systems. For the Pd porphyrin Zn-SURMOF 2 the observed emission is limited by the instrument response of the streak camera, so the singlet exciton lifetime is less than 15 ps. This is consistent with the fast intersystem crossing and unity yield of triplet states in Pd porphyrin dyes in solution.[179] The free base porphyrin Zn-SURMOF 2 shows a singlet exciton lifetime of approximately 100 ps. This is two orders magnitude lower than the 10 ns singlet exciton lifetime of the free base linker in solution (Figure 4.15 (b)), meaning that over 99% of the singlet excitons are quenched even in the free base porphyrin Zn-SURMOF 2. For both types of SURMOFs studied here, this observation strongly indicates that the singlet-excitons resulting from the photo absorption process are quickly converted into triplet-excitons by means of fission of primary singlets, which typically show much longer life-times and, as a result, diffusion length.[180]
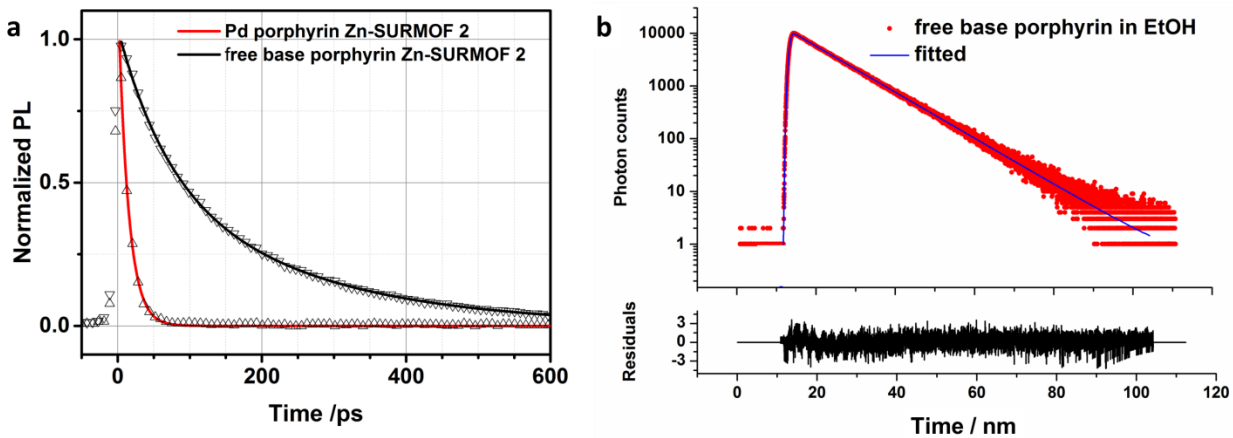
Figure 4.15 (a) Time-resolved photoluminescence of the free base porphyrin Zn-SURMOF 2 and Pd porphyrin Zn-SURMOF 2. (b) Fluorescence lifetimes of free base porphyrin in ethanol solution (20 μM). The free base porphyrin can be fit well with a single exponential decay with a lifetime of 10 ns.

The results from transient absorption spectroscopy (Figure 4.16) also provide evidence for the fast and high-yield formation of long-lived states from the singlet exciton, and are in fact fully consistent with the formation of triplet states. It shows the mean photoinduced absorption kinetics between 700 and 750 nm as a function of time after excitation at 400 nm with an intensity of 15 μJ cm^{-2}. Both porphyrin SURMOFs show the creation of long-lived states responsible for photovoltaic action following the fast quenching of the singlet exciton population. Importantly, we clearly detect the creation of long-lived states in both the free-base porphyrin Zn-SURMOF 2 and the Pd porphyrin Zn-SURMOF 2. We see a fast decay component of the photoinduced absorption in both samples that is associated with the transition from singlet-excitons to the long-lived species responsible for the photovoltaic performance. In agreement with the time-resolved photoluminescence, this population transition has a longer-lived component in the free-base Zn-SURMOF 2 matching the 100 ps singlet exciton lifetime. However, both samples also show a fast decay component with time constant of about 8 ps. After this fast singlet-exciton quenching, a clear signal is left from the resultant population that does not decay at all on the 4 ns timescale. This is a clear evidence for the fast and high-yield formation of long-lived states from the singlet exciton which underpin the long-diffusion in the highly ordered material and photovoltaic performance.
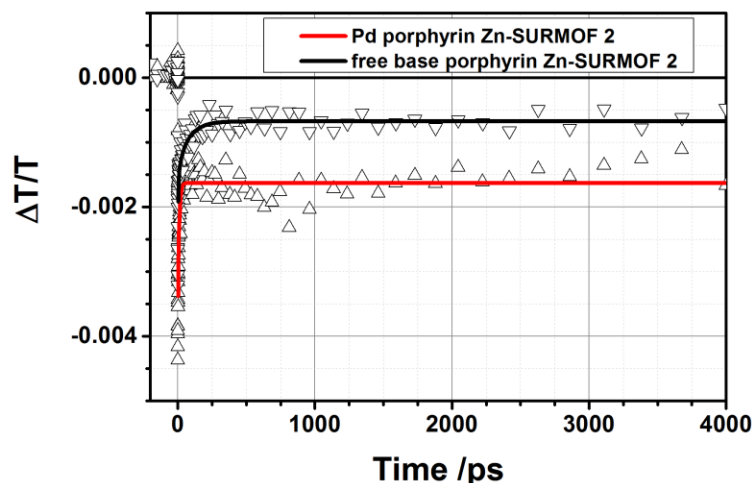
Figure 4.16 Mean photoinduced absorption kinetics in the 700-750 nm spectral window measured with TAS for the free base porphyrin Zn-SURMOF 2 and Pd porphyrin Zn-SURMOF 2.

The successful operation of our porphyrin SURMOF based photovoltaic device can be rationalized by considering the energy-level diagram which shows the positions of the F: SnO$_2$ substrate flatband[181,182] and that of the porphyrin SURMOFs. On the basis of this existing knowledge and experiments, the electrons are proposed to be injected from the MOF porphyrin ligands into the FTO substrate (Figure 4.14 (b)).

We thus attribute the astonishingly good performance of our novel single-component SURMOF-based OPV device to two effects. First, the presence of the Zn-ions linking the porphyrin-units to form the metal-organic framework strongly enhances a singlet-to-triplet conversion of the excitons. Second, the regular array of porphyrin units present in the 3D-structure, with a periodic, well-defined overlap between adjacent porphyrin units results in huge triplet exciton diffusion lengths. As a result, the triplet excitons have a high chance to reach the SURMOF/FTO interface, where they are dissociated to yield an electron transferred to the substrate and a hole, which is transported through the SURMOF-film to the top electrode. The fairly high electron mobility required to make this transfer effective is proposed to also result from the overlap between the adjacent porphyrin units.

4.1.6 Computational studies of porphyrin based SURMOF

The calculations were attributed by the group of Prof. Thomas Heine and Dr. Agnieszka Kuc from Jacobs University Bremen.

61

To further figure out the reason why Pd porphyrin Zn-SURMOF 2 exhibits better photovoltaic performance, more computational studies were carried out. The presence of an organic solid with known, strictly periodic structure allows for a meaningful comparison to the results of high-level electronic structure calculations.

First, the atomistic structure of porphyrin SURMOF (Figure 4.2 and Figure 4.17) was obtained from Universal Force Field (UFF),[183] employing the UFF4MOFparameter extension and by employing the General Utility Lattice Program (GULP) version 4.2.[184,185] The bond order specified between paddlewheel Zn atoms was 0.25, paddlewheel Zn-O bonds were specified as 0.5 and all other bond orders were specified according to standard chemical notation. The optimized lattice constants for free-base porphyrin SURMOF is $c = 6.75$ Å for the interlayer distance, and $a = b = 23.96$ Å for the in-plane lattice parameters. Insertion of metals significantly lowers the in-plane lattice parameter by 0.05 Å.
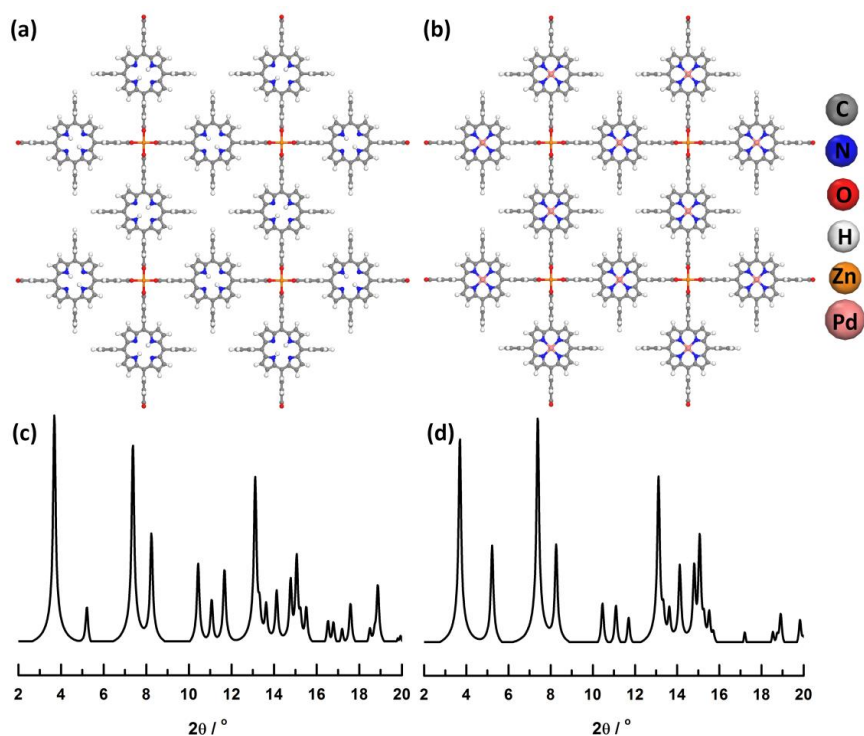
Figure 4.17 Calculated structure of (a) free base porphyrin Zn-SURMOF 2 and (b) Pd porphyrin Zn-SURMOF-2; Simulated XRD patterns of (c) free base porphyrin Zn-SURMOF 2 and (d) Pd porphyrin Zn-SURMOF-2.

Then, the porphyrin electronic structure and light absorption were computed. Band- and HOMO-LUMO gaps calculations of the framework and of the hydrogenated porphyrin have been carried out using the density functional based tight-binding (DFTB) method using the QUASINANO 2013.1 parameters[186] and the DFTB+ 1.2 code.[184,185] Time dependent density functional theory (TD-DFT) calculations employed the PBE0 functional with a 6-311++g (2d, p) basis set as implemented in the Gaussian09 program.[187] Generalized gradient approximation density functional theory (GGA-DFT)band structure calculations were performed using the CRYSTAL09 code, PBE functional, and TZVP basis set (except for Pd, which was treated using the HAYWSC ECP).[188-190]

In fact, the HOMO-LUMO energy difference of a saturated, single porphyrin molecule is essentially identical to the band gap at the Γ point of the periodic structure. For free-base porphyrin Zn-SURMOF 2, a band gap of 1.58 eV (DFTB level, DFTB = density-functional based tight-binding) nearly coincides with the 1.60 eV HOMO-LUMO gap of the saturated single porphyrin molecule. The value of the saturated single porphyrin molecule can be compared with TD-DFT, which gives 1.51 eV for the same system. Introduction of metal centers increases the band gap to 1.94 eV (Pd porphyrin Zn-SURMOF 2) and 1.88 eV (Zn porphyrin Zn-SURMOF 2).
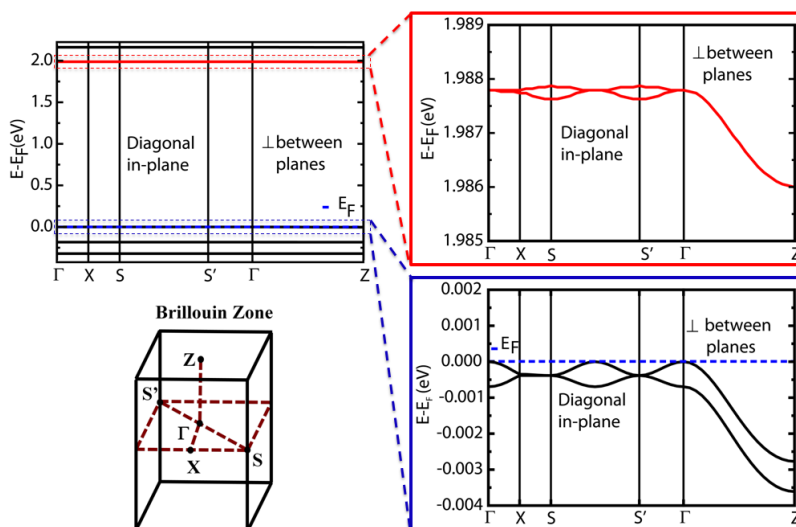
Figure 4.18 Band structure of Pd porphyrin Zn-SURMOF 2. Calculated band structure at the PBE level, the high-symmetry k points are indicated in the sketch of the Brillouin zone (left). The

magnified two frontier bands of the conduction and balance bands are given on the right. The Fermi level is defined as the valence-band maximum.

Then, GGA-DFT band structure of Pd porphyrin Zn-SURMOF 2, which exhibits the highest efficiency was investigated, shown in Figure 4.18. At first sight the band structure appears to comply with the expectation that the bands are essentially flat. A closer inspection, however, reveals a small but distinct dispersion of about 3 meV for both valence and conduction bands. The strongest dispersion is seen in the Γ-Z direction, i.e. perpendicular to the paddle-wheel-planes, along the columns of the stacked porphyrin disks. This observation reveals that the intermolecular overlap is strongest along the columns. The dispersion allows the effective masses of the charge carriers to be estimated, giving $4.5m_e$ (holes) and $9.6m_e$ (electrons). These values are an order of magnitude higher than in traditional semiconductors such as silicon, but appreciable in comparison with other organic materials. Importantly, the minimum in the conduction band (CB) is at the Z-point, whereas the maximum of the valence band (VB) is at the Γ-point. The SURMOF 2 structure thus has to be classified as an indirect band-gap semiconductor.[191] The energy gain from the band dispersion is only on the order of 5 meV and thus certainly not sufficient for electron-hole separation. However, once electrons and holes are relaxed, direct electron-hole recombination is suppressed unlike in direct band-gap systems. Good carrier mobility along with suppressed recombination is consistent with the impressive behavior of the MOF-based OPV realized. Since the indirect band-gap for the Pd porphyrin Zn-SURMOF 2 is substantially larger than for the free-base porphyrin Zn-SURMOF 2 is fully consistent with the substantially better OPV performance of the metal porphyrin system.

4.1.7 Summary

In summary, highly oriented and crystalline porphyrin-based SURMOF thin films have been epitaxially grown as supramolecular arrays on various substrates. A prototype organic photovoltaic device, in which the substrate is used as an anode and I^-/I_3^- containing electrolyte as a cathode, shows a remarkable photovoltaic performance, with a maximum conversion yield of 0.45% for artificial sunlight. Measurements of the photoluminescence and photoconductivity as a function of SURMOF thickness reveal that this performance for a single-component organic photovoltaic device is quite large. Such high efficiency results from an effective conversion of exciton singlets into exciton triplets, with unusually large exciton diffusion length of the latter.

Further band structure calculation revealed that the SURMOF 2 structure should have an indirect band gap. Although certainly much more in depth work is needed to better understand the underlying mechanism, we see a strong potential of this material to create a major impact to the field of flexible solar cells.[192]

4.2 Porphyrin-based SURMOF for all-solid photovoltaic device

4.2.1 Background

In Chapter 4.1, a solar cell with remarkably large solar to electricity conversion efficiency has been fabricated by a free base and Pd-metalized porphyrin SURMOF. Although highly important as a proof-of-principle, this first MOF-based photovoltaic device needs to be improved with regard to applications. The redox pair I^-/I_3^- liquid used in those solution-base solar cells is corrosive to the photosensitizers in dye sensitized solar cell (DSSC). Thus, a novel MOF-based solar cell architecture, where the liquid top electrode is replaced by a solid top layer fabricated from a conductive polymer, is proposed in this part.

In addition, a modified porphyrin linker with two diphenylamine (DPA) groups attached to the porphyrin core was involved to construct the photovoltaic device. The high electron affinity of these functional groups substantially lowers the band gap of the porphyrin framework material, which is a very important improvement for the photovoltaic applications. The molecular structures of the porphyrins used in this part are shown in Figure 4.19, where both porphyrin molecules were metallized by zinc and the only difference is the DPA groups, named Zn(II)porphyrin and DPA- Zn(II)porphyrin.

Zn(II)porphyrin   **DPA-Zn(II)porphyrin**
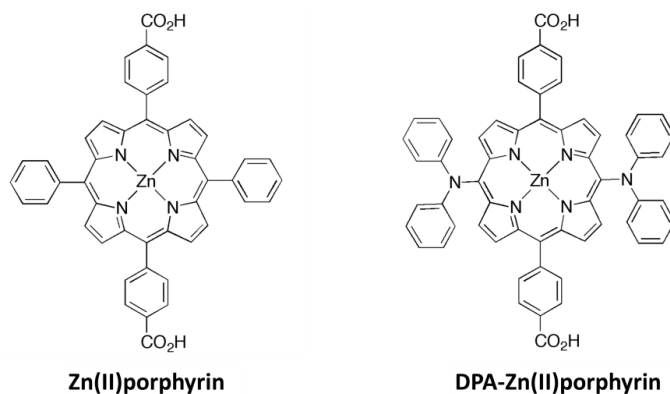
Figure 4.19 Molecular structure of Zn(II)porphyrin and DPA- Zn(II)porphyrin.

In this chapter, a novel new type of Zn(II)porphyrin SURMOF 2 thin film with high photocarrier generation efficiency and very good photocarrier mobility is synthesized. A prototype electrolyte free, all-solid-state photovoltaic device are constructed using these Zn(II)porphyrin SURMOF 2

thin film materials. By simply attaching the group which lowers the band gap to the porphyrin ring in these SURMOF 2 thin film materials, the energy conversion efficiency is enhanced.

4.2.2 Characterization of the Zn(II) porphyrin-based Zn-SURMOF 2

Zn(II) porphyrin and DPA-Zn(II) porphyrin based SURMOF using zinc acetate as a metal source and the corresponding porphyrin as organic ligand were deposited on various substrates in a layer-by-layer fashion, such as SAMs, FTO, Si and quartz, using spray method, which were described in detail as Chapter 3.4.2.

The out of plane XRD data of Zn(II) porphyrin and DPA-Zn(II) porphyrin based SURMOF fabricated on FTO, quartz glass and Au substrates functionalized with MUD SAMs are shown in Figure 4.20. It reveals that the LPE-process yields crystalline and highly oriented Zn(II)porphyrin Zn-SURMOF 2 thin films. Both SURMOF films are highly crystalline and oriented along [001] orientation on these substrates.
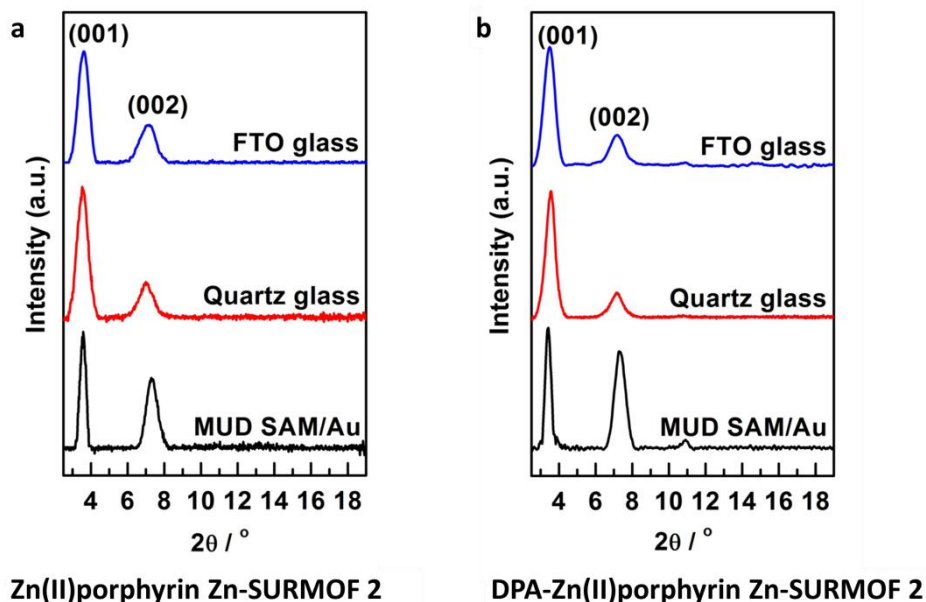
Figure 4.20 Out of plane XRD data of (a) Zn(II)porphyrin Zn-SURMOF 2 and (b) DPA-Zn(II)porphyrin Zn-SURMOF 2 grown on FTO glass, quartz glass and MUD SAM/Au substrates prepared by liquid-phase epitaxy process.

The comparisons of out of plane, in plane and simulated XRD data of Zn(II) porphyrin and DPA-Zn(II) porphyrin Zn-SURMOF 2 are shown in Figure 4.21. The experimental XRD data

are in excellent agreement with the simulated XRD patterns in Chapter 4.1. Evaluating the XRD data together with simulated XRD patterns, the structures of Zn(II)porphyrin based Zn-SURMOF 2 are proposed as illustrated in Figure 4.22. Basically, these structures consist of planes formed by Zn^{2+} -based paddle-wheels oriented perpendicular to the surfaces, resulting in pronounced one dimensional (1-D) channels parallel to the surface. The lattice parameter in the direction perpendicular to the surface of Zn(II) porphyrin Zn-SURMOF 2 is determined to be 23.51Å, the lattice parameter in the direction parallel to the surface is determined to be 23.51Å and the layer distance is 6.5 Å. While the lattice parameters of DPA-Zn(II) porphyrin Zn-SURMOF 2 in the direction perpendicular to the surface as well as parallel to the surface are 23.47Å and the layer distance is 10.34 Å due to the space of the DPA groups.
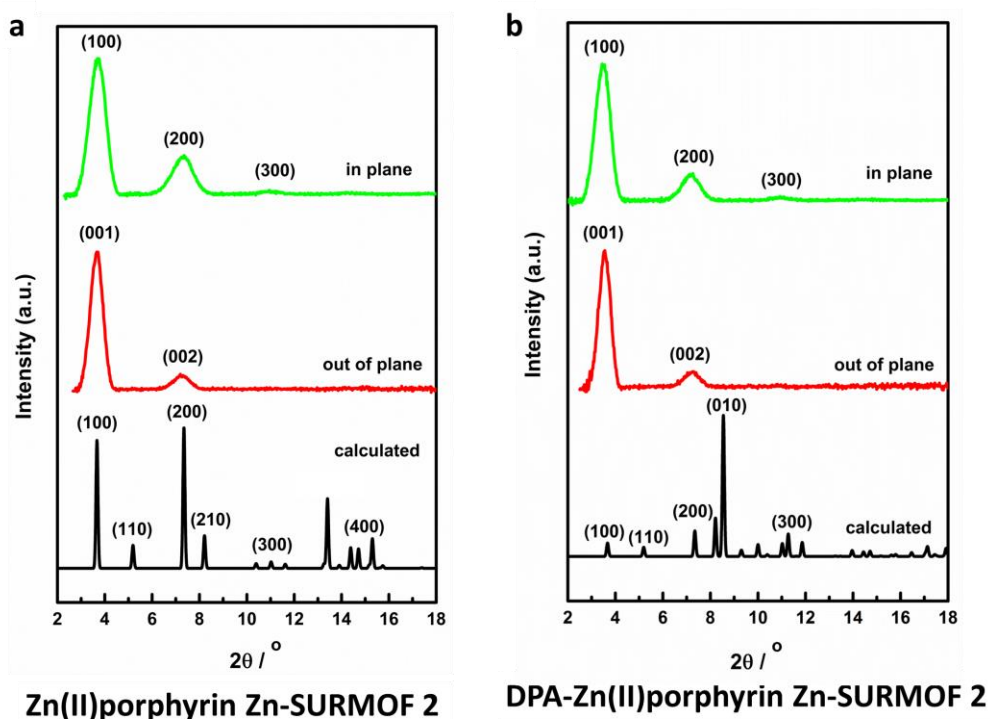
Figure 4.21 Comparison of in plane, out of plane and simulated XRD data of Zn(II)porphyrin Zn-SURMOF 2 (a) and DPA-Zn(II)porphyrin Zn-SURMOF 2 (b) fabricated onto Si substrate by liquid-phase epitaxy process.
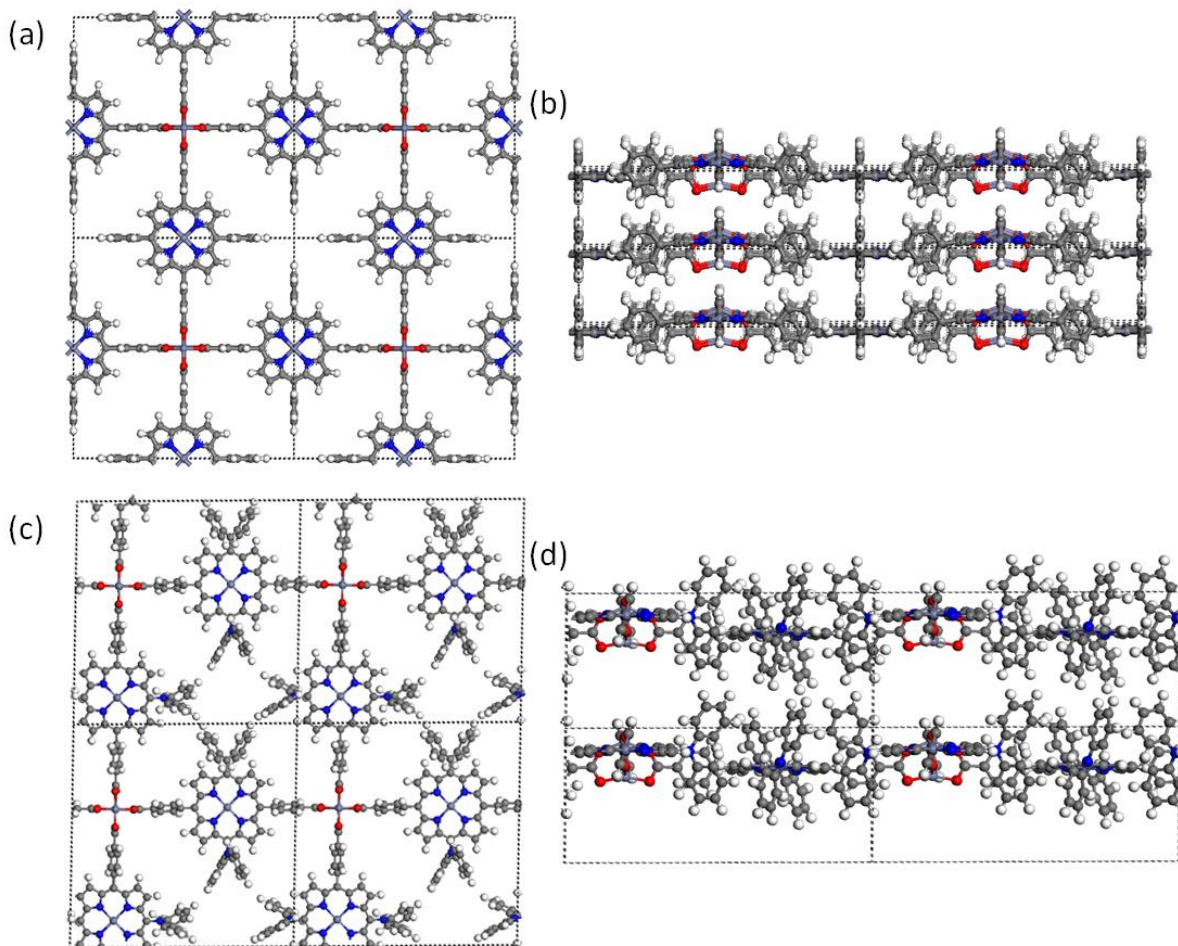
Figure 4.22 (a) and (b) Simulated structure of Zn(II)porphyrin Zn-SURMOF 2 with lattice parameters a = b = 2.351 nm, c = 6.5 Å; (c) and (d) Simulated structure of DPA-Zn(II)porphyrin Zn-SURMOF 2 with lattice parameters a = b = 2.347 nm, c = 10.34 Å.

The IR spectra of Zn(II)porphyrin and DPA-Zn(II)porphyrin Zn-SURMOF 2 grown on MUD SAMs/Au substrates are shown in Figure 4.22. The bands at 1682 cm^{-1} and 1685 cm^{-1} in bulk Zn(II)porphyrin and bulk DPA-Zn(II)porphyrin, respectively, are due to the C=O stretching in free carboxylic groups. As anticipated, these bands are completely vanished in the corresponding IRRA spectra of porphyrin based SURMOFs, suggesting that the formation of coordination bonds between the porphyrin molecules and Zn acetate. The broad bands centered at ~1592 cm^{-1} and ~1403 cm^{-1} for the porphyrin SURMOF are attributed to the asymmetric and symmetric stretching of COO$^-$ groups, respectively. The difference (Δv_{COO^-}) of ~200 cm^{-1} indicates the formation of a perfect zinc paddle-wheel structure with bidentate bridging bonding, which is

similar to the phenomenon observed in Chapter 4.1. The detailed band assignments corresponding to Zn(II)porphyrin and DPA-Zn(II)porphyrin Zn-SURMOF 2 are listed in Table 4.2.
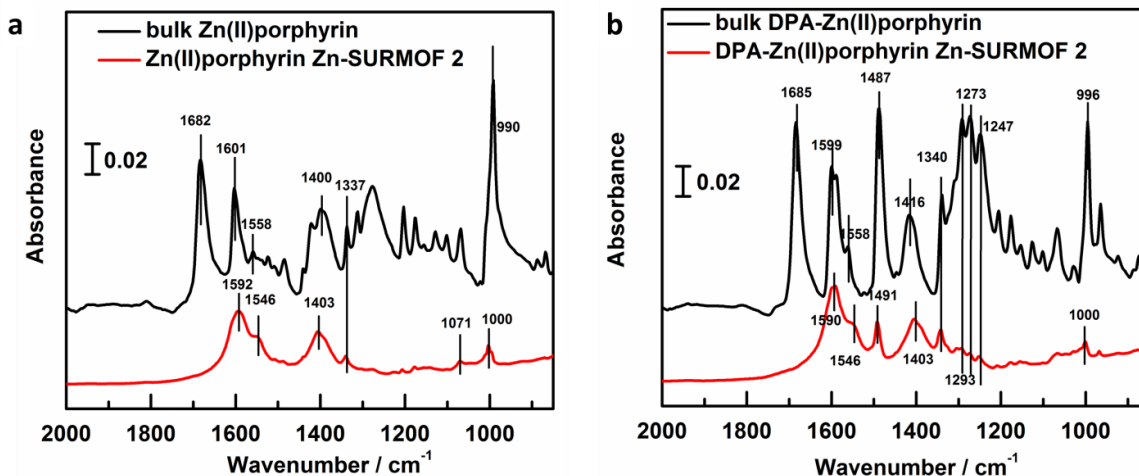
Figure 4.22 IR spectra of bulk Zn(II)porphyrin (in black) and Zn(II)porphyrin Zn-SURMOF 2 (a) and bulk DPA-Zn(II)porphyrin (in black) and DPA-Zn(II)porphyrin Zn-SURMOF 2 (b) grown on MUD/Au substrate (in red).

Table 4.2 Vibrational frequencies of Zn(II)porphyrin and DPA-Zn(II)porphyrin as obtained spectra from bulk and MOF thin films grown on MUD/Au substrate together with the assignments.

Zn(II)porphyrin			DPA-Zn(II)porphyrin		
Wavenumber (cm^{-1})		Assignment	Wavenumber (cm^{-1})		Assignment
SURMOF	Bulk		SURMOF	Bulk	
--	1682	ν C=O in free COOH	--	1685	ν C=O in free COOH
1592	1601	ν_{as} COO$^-$; CC (aromatic ring)	1590	1599	ν_{as} COO$^-$; CC (aromatic ring)
1546	1558	COO$^-$	1546	1558	COO$^-$
1403	1416	ν_s COO$^-$; Phenyl	1491	1487	Pyrrolic
1337	1337	def Porphyrin	1403	1416	ν_s COO$^-$; Phenyl
1071	--	δ CH$_{Porphyrin}$	1340	1340	def Porphyrin
1000	990	i.p. Ph	1000	996	i.p. Ph

ν: stretching mode, ν_{sym}: symmetric stretching mode, ν_{as}: asymmetric stretching mode
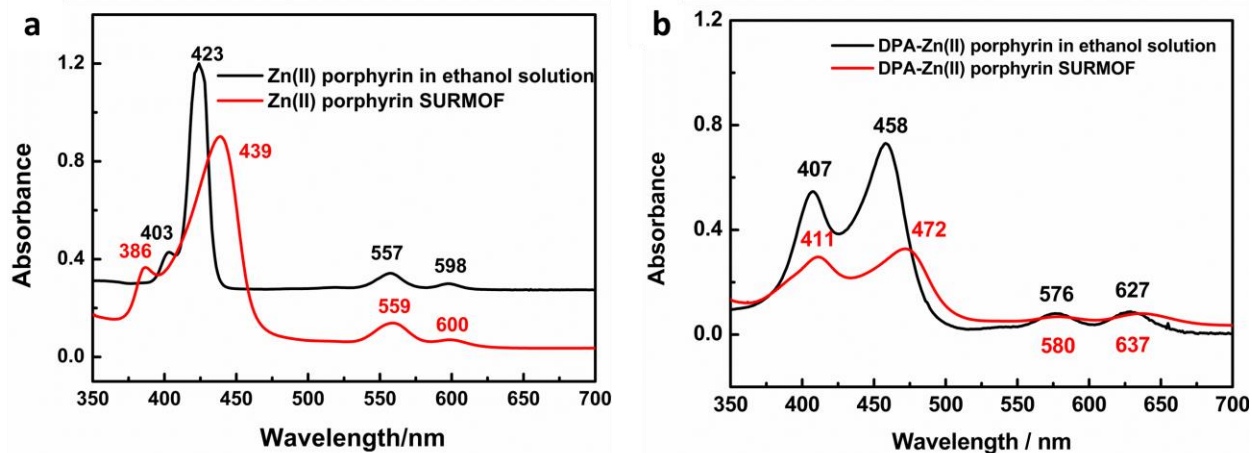
Figure 4.23 UV-Vis spectrum of Zn(II)porphyrin (a) and DPA-Zn(II)porphyrin Zn-SURMOF 2 (b) and the corresponding photograph of Zn(II)porphyrin (c) and DPA-Zn(II)porphyrin Zn-SURMOF 2 (d) on quartz glass

To exclude the substrate influence on intrinsic photophysical properties of these SURMOF thin films, Zn(II)porphyrin and DPA-Zn(II)porphyrin Zn-SURMOF 2 materials prepared on quartz glass substrates are characterized with UV-Vis spectroscopy. The corresponding UV-Vis spectra are shown in Figure 4.23(a) (b), respectively. Typical UV-Vis features for metalloporphyrin with sharp Soret bands together with two Q bands were observed. Compared with the porphyrin molecule in ethanol solution, the Soret band of the corresponding porphyrin SURMOF has a redshift due to the extended π-conjunction of the porphyrins constructed into highly oriented and ordered structure.[171] The UV-Vis spectrum of DPA-Zn(II)porphyrin Zn-SURMOF 2 shows dramatic redshift about 40 nm to the visible light region compared with that of Zn(II)porphyrin Zn-SURMOF 2, resulting from the introduction of DPA groups into Zn(II)porphyrin Zn-SURMOF 2.

The XPS data (Figure 4.24) of Zn(II)porphyrin Zn-SURMOF 2 and DPA-Zn(II)porphyrin Zn-SURMOF 2 were carried out and fitted with a fixed full width at half maximum (FWHM) value 1.7 eV. The N1s peak appeared at 397.3 eV for Zn(II)porphyrin Zn-SURMOF 2 is attributed to the =N- of the Zn(II)metalloporphyrin unit. The N1s peaks appeared at 397.6 eV and 399.1 eV for DPA-Zn(II)porphyrin Zn-SURMOF 2 are attributed to the =N- of the Zn(II)metalloporphyrin unit and diphenylamine (DPA) groups.
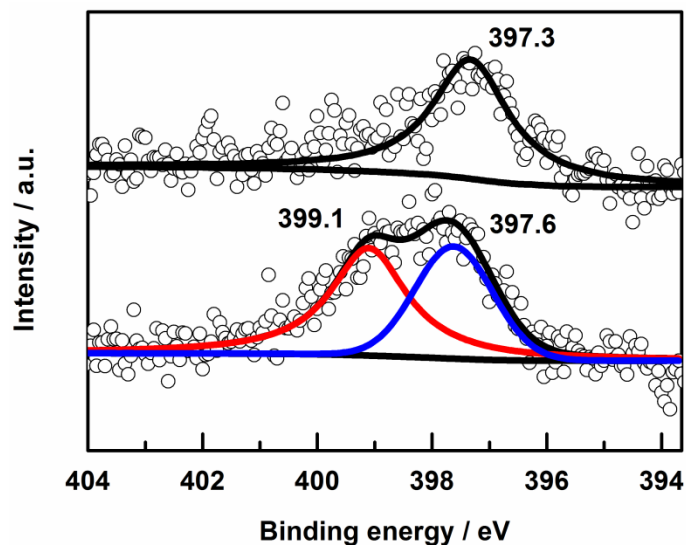
Figure 4.24 X-ray photoelectron spectra of Zn(II)porphyrin Zn-SURMOF 2 (up) and DPA-Zn(II)porphyrin Zn-SURMOF 2 (bottom) grown on MUD/Au substrate.

4.2.3 Photocurrent and photovoltaic measurement

4.2.3.1 Preparation of Al/PEDOT: PSS/Porphyrin SURMOF/FTO/Glass device

The Zn(II)porphyrin Zn-SURMOF 2 and DPA-Zn(II)porphyrin Zn-SURMOF 2 films were assembled into devices with an architecture "FTO glass/(DPA-) Zn(II)porphyrin Zn-SURMOF 2 /PEDOT: PSS/Al" as illustrated in Figure 4.25 (a). The top electrode consists of a thin layer of a conductive polymer (PEDOT: PSS), which performs two different functions. It serves as hole transport layer[193] and also as a diffusion barrier to the Al evaporated on top of the thin multilayer system to form metal top electrodes.

To assemble such device, 1% (wt%) CLEVIOS™ PH 1000 (PEDOT: PSS) liquid was diluted in Milli-Q H_2O (2/33, v/v) with ultrasonic for 1 min. For the spin-coating method, a few drops of the solution were dropped onto the porphyrin thin films at room temperature with a speed at 3000 rpm for 1 minute, the resulting thickness of PEDOT: PSS films amount to be 100 nm - 150 nm (Figure 4.25 (b)). The PEDOT: PSS/Porphyrin SURMOF/FTO/Glass device was dried at 150 °C in an oven for 30 min, subsequently an Al counter electrode with a thickness of 100 nm was deposited by using physical vapor deposition.
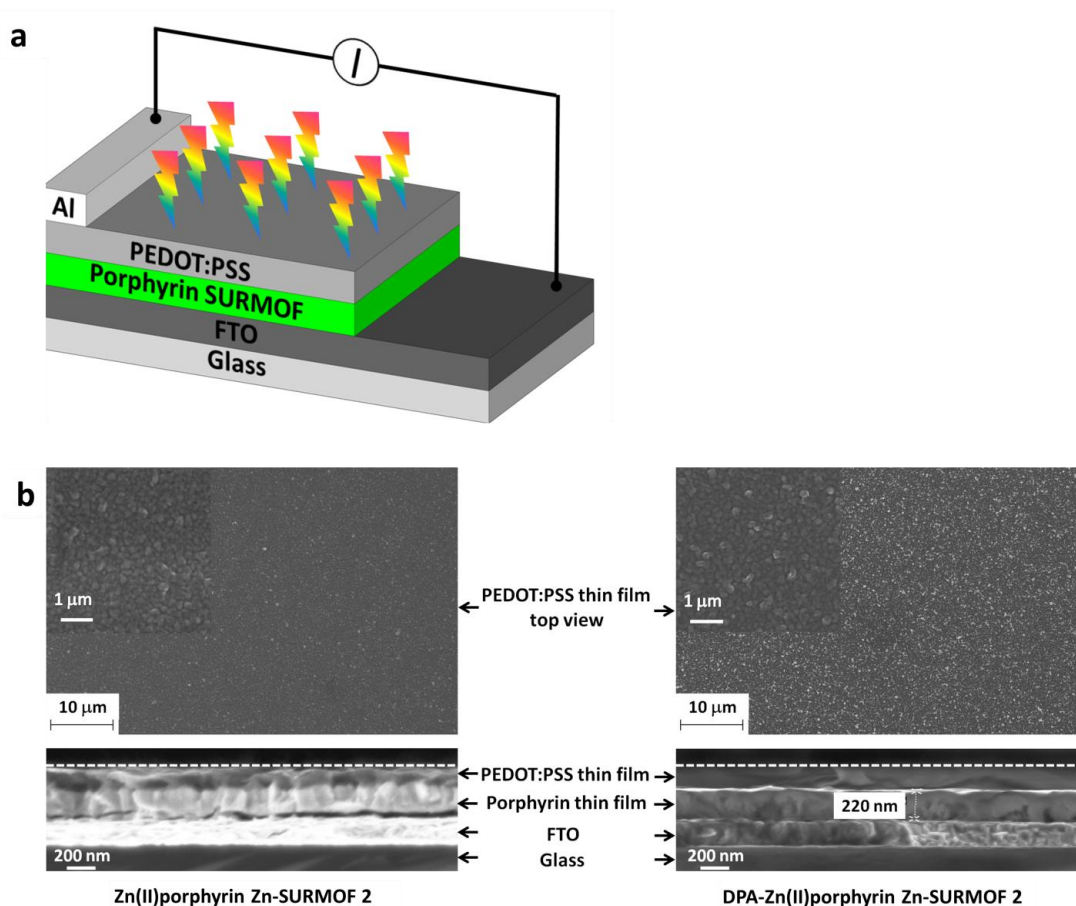
Figure 4.25 (a)) Schematic drawing of Zn(II)porphyrin based Zn-SURMOF 2 PV device (b) SEM images of Zn(II)porphyrin Zn-SURMOF 2 (left) and DPA-Zn(II)porphyrin Zn-SURMOF 2 (right) with top PEDOT:PSS thin film electrodes.

4.2.3.2 Photocurrent measurement

All photocurrent measurements has been performed by two-probe setup equipped using Agilent 4156C semiconductor parameter analyzer and Süss MicroTec EP6 probe station coupled with a LEDs system (Prizmatix Ltd., 530 nm) with five wavelengths: 365 nm, 400 nm, 455 nm, 530 nm and 640 nm, at ambient conditions. The focused light area is about 0.1 cm^2. Initially, two probes are connected to the bottom and top electrodes of SURMOF respectively and then very low voltage (0.1 V) is applied to measure the resistance. Once the resistance measurements are done, zero current and zero voltage is applied to the bottom and top electrodes respectively.
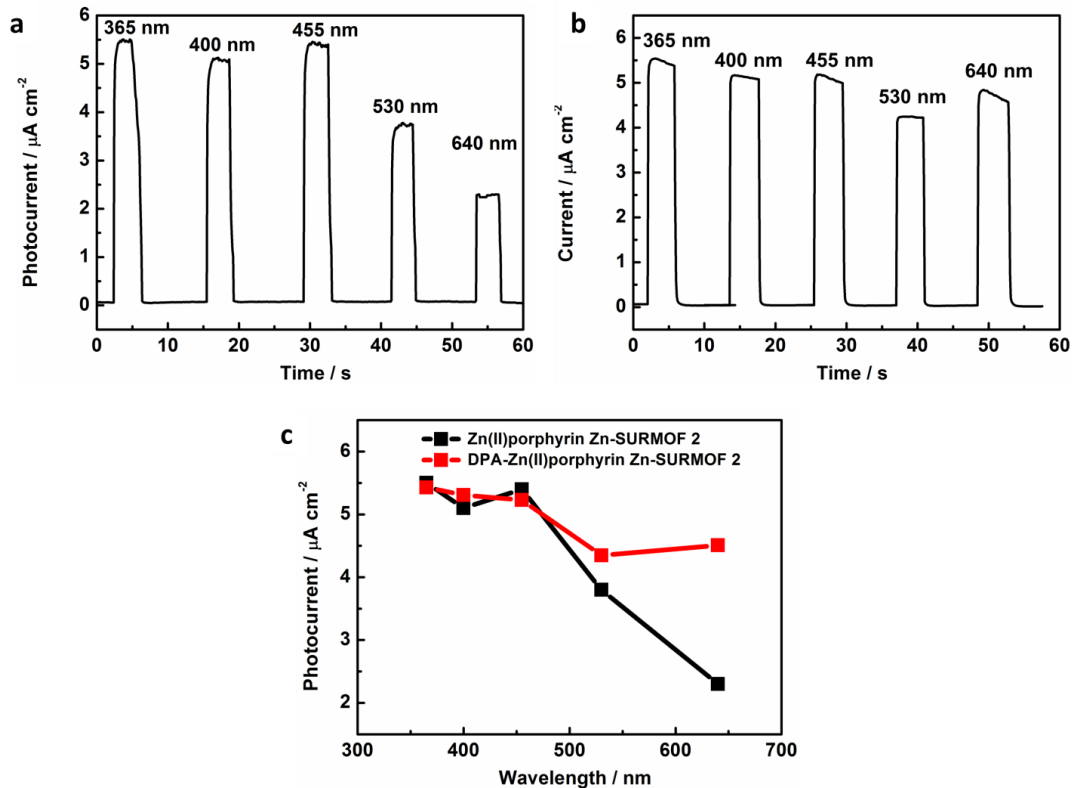
Figure 4.26 Photocurrent of Zn(II)porphyrin Zn-SURMOF 2 (a), DPA-Zn(II)porphyrin Zn-SURMOF 2 (b) thin film PV device under illuminations at 365 nm, 400 nm, 455 nm, 530 nm and 640 nm. The illumination time is about 5 s. and (c) the corresponding photoaction spectra.

While the measurement is running, a light with selected wavelength is switched on and off every 5 seconds to measure the current with and without light. Change in current is observed when the light is on and off. Both Zn(II)porphyrin Zn-SURMOF 2 and DPA-Zn(II)porphyrin Zn-SURMOF 2 thin films with 30 spraying cycles exhibit quick photocurrent response with light on and off as shown in Figure 4.26 (a) and (b), respectively. The observed change in the current is varied based on composition and wavelength of applied light. The corresponding photocurrent action data of Zn(II)porphyrin and DPA-Zn(II)porphyrin Zn-SURMOF 2 are summarized in Figure 4.26 (c). While the introduction of the DPA groups has very small influence on the generated photocurrent at wavelengths of 365 nm, 400 nm and 455 nm, the photocurrent generated at 530 nm and 640 nm is substantially larger, as expected from the red-shifted absorption spectrum of the DPA-functionalized porphyrin. The photocurrent generated at 640 nm

in the visible light region is enhanced from ~ 2 µA cm^{-2} for Zn(II)porphyrin Zn-SURMOF 2 to ~ 4.5 µA cm^{-2} for DPA-Zn(II)porphyrin Zn-SURMOF 2.

4.2.3.3 Photovoltaic performance
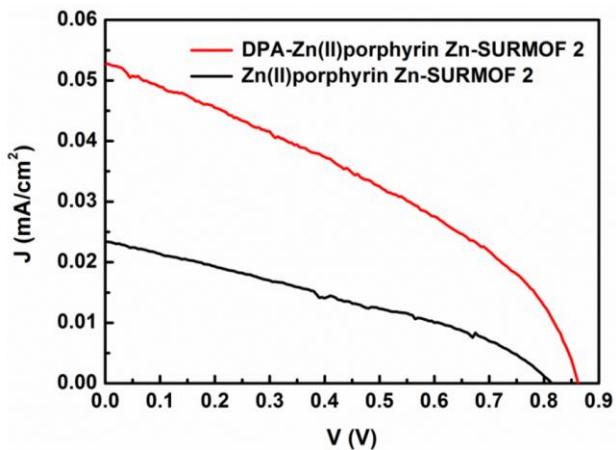
Figure 4.27 J-V curve of Zn(II)porphyrin and DPA-Zn(II)porphyrin Zn-SURMOF 2 based photovoltaic device.

Table 4.3 Zn(II)porphyrin and DPA- Zn(II)porphyrin Zn-SURMOF 2 based photovoltaic performances.

	Voc (V)	Jsc (mA cm^{-2})	FF	Eff (%)
Zn(II)porphyrin Zn-SURMOF 2	0.815	0.023	0.333	0.006
DPA-Zn(II)porphyrin Zn-SURMOF 2	0.86	0.053	0.368	0.017

The photovoltaic performance of the assembled "FTO/(DPA-) Zn(II)porphyrin Zn-SURMOF 2 /PEDOT: PSS/Al" devices was also carried out using a Keithley electrochemical under illumination using AM 1.5 solar simulator with an active area of 0.1 cm^2. The J-V curves recorded for Zn(II)porphyrin and DPA- Zn(II)porphyrin Zn-SURMOF 2 based devices are shown in Figure 4.27. While the open-circuit voltages are very high, i.e. 0.815 V for Zn(II)porphyrin Zn-SURMOF 2 and 0.86 V for DPA-Zn(II)porphyrin Zn-SURMOF 2, the corresponding total efficiencies are rather low, i.e. only 0.006% and 0.017%, respectively. The calculated results in detail are shown in Table 4.3.

4.2.3.4 Photophysical properties

For a more thorough photophysical characterization of the porphyrin SURMOFs, FP-TRMC and TAS measurements have been carried out. In particular, these techniques allow investigation of the intrinsic and local-scale photo-induced charge carrier generation efficiency and charge-carrier mobility of various types of materials. Transient absorption spectra of Zn(II)porphyrin Zn-SURMOF 2 and Zn(II)porphyrin Zn-SURMOF 2 grown on a quartz glass are displayed in Figure 4.28 (a) and (b), respectively. The spectra were averaged at 0-0.2s after the photoexcitation at 355 nm. The photon density of the excitation laser was 4.6×10^{15} photons pulse^{-1} cm^{-2}. The corresponding two-dimensional transient absorption spectral data were recorded shown in Figure 4.28 (c) and (d). The results revealed the generation of radical cations as well as photo-bleaching of the porphyrin chromophores. Typical FP-TRMC profiles recorded after photoexcitation at 355 nm for Zn(II)porphyrin Zn-SURMOF 2 (black) and DPA-Zn(II)porphyrin Zn-SURMOF 2 (red) are presented in Figure 4.29(a), where the prompt rise and gradual decay in conductivity transients were clearly observed. The normalized FP-TRMC and transient absorption profiles at 540 nm (green) and 570 nm (blue) of Zn(II)porphyrin Zn-SURMOF 2 as well as 595 nm (green) and 630 nm (blue) of DPA-Zn(II)porphyrin Zn-SURMOF 2 grown on a quartz glass are shown in Figure 4.29 (b) (c). The difference of the kinetics in DPA-Zn(II)porphyrin Zn-SURMOF 2 is most likely due to the fundamental absorption over a broad wavelength range. Considering the similarity of TRMC and TAS kinetics, it can be concluded that these Zn(II)porphyrin-based thin films exhibit typical hole transporting properties.
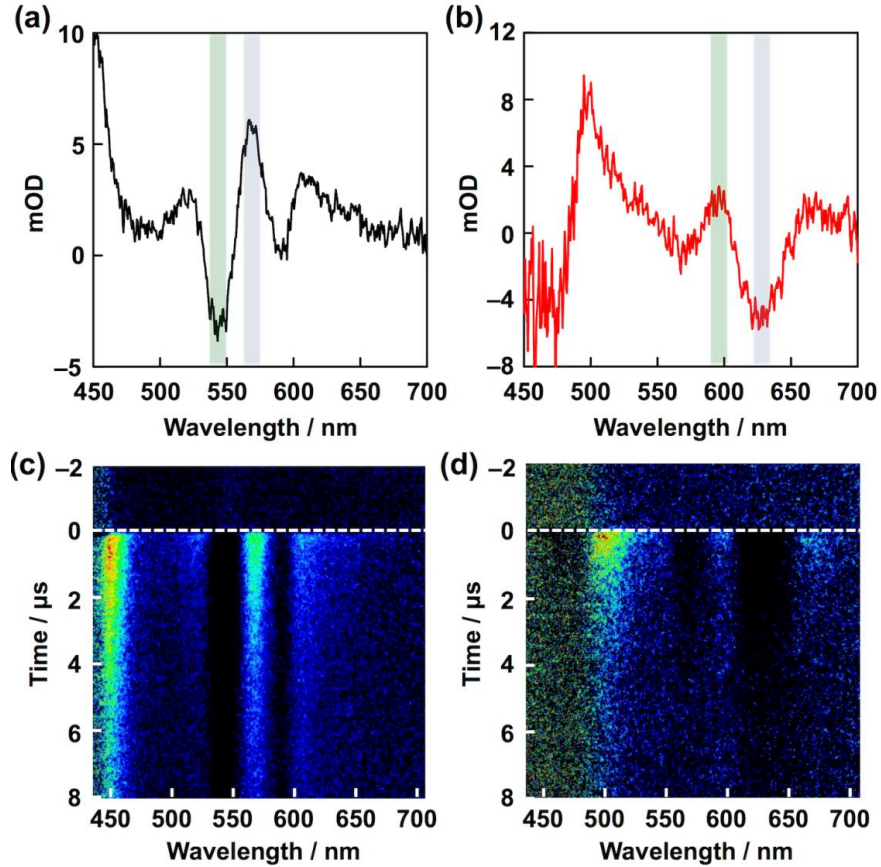
Figure 4.28 Transient absorption spectra averaged at 0-0.2 μs of (a) Zn(II)porphyrin Zn-SURMOF 2 and (b) Zn(II)porphyrin Zn-SURMOF 2 grown on a quartz glass. The photon density of 355-nm excitation laser was 4.6 × 10^{15} photons pulse^{-1} cm^{-2}. Two-dimensional transient absorption spectral data recorded for (c) Zn(II)porphyrin Zn-SURMOF 2 and (d) Zn(II)porphyrin Zn-SURMOF 2 grown on a quartz glass.

Based on the observed photo-bleach in the Q-bands region (Figure 4.28 (a) and (b)), the photocarrier generation yield (φ) was evaluated, yielding up to φ = 0.3 and 0.21 for Zn(II)porphyrin Zn-SURMOF 2 and DPA‑Zn(II)porphyrin Zn-SURMOF 2, respectively. These are the largest values reported so far for any OPV thin film. They exceed the efficiency for Pd porphyrin Zn-SURMOFs in Chapter 4.1 and are substantially larger than those obtained for other porphyrin-based MOF materials[173] and porphyrin-based COFs[174] with a typical value of 10^{-4}. By combining the evaluated φ values and the $(\varphi\Sigma\mu)_{max}$ in TRMC, the hole mobility was estimated as $\mu = 1.1 \times 10^{-3}$ cm^2 V^{-1} s^{-1} for both SURMOF films.
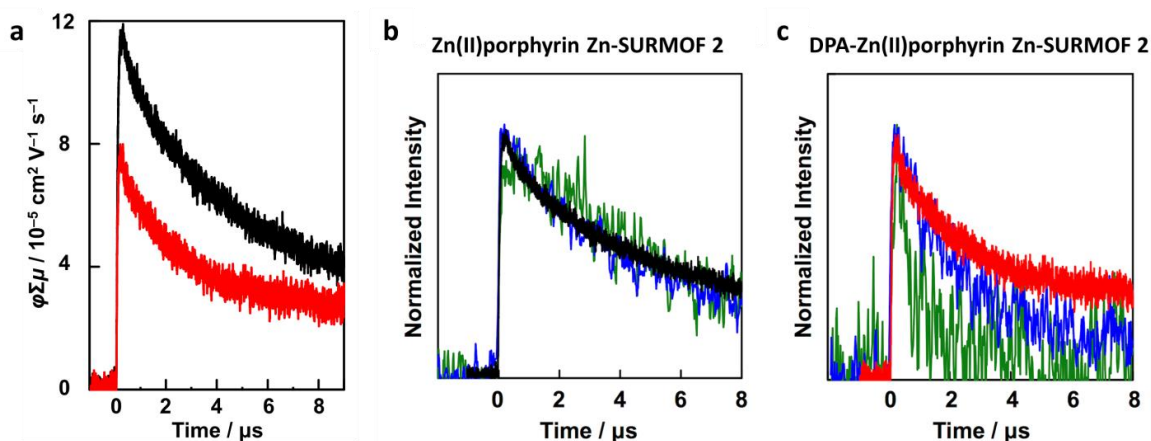
Figure 4.29 (a) FP-TRMC profiles of Zn(II)porphyrin Zn-SURMOF 2 (black) and DPA-Zn(II)porphyrin Zn-SURMOF 2 (red). (b) Normalized FP-TRMC (black) and transient absorption profiles at 540 nm (green) and 570 nm (blue) of Zn(II)porphyrin Zn-SURMOF 2. (c) Normalized FP-TRMC (red) and transient absorption profiles at 595 nm (green) and 630 nm (blue) of DPA-Zn(II)porphyrin Zn-SURMOF 2 grown on a quartz glass.

Porphyrin COFs with two dimensional (2D) flat sheets structures have been demonstrated to exhibit high charge carrier mobility. In these structures, the stacked porphyrin layers have a very short interlayer distance of less than 4 Å, forming a π-conjugated system, which serves as an effective pathway for charge-carrier transport.[194,195] In the present work, the calculated interlayer distances of the porphyrin units amount to 6.5 Å and 10.34 Å, resulting in a weak coupling between the adjacent layers. These large distances severely hinder the charge carrier transport between neighboring porphyrins, which is in accordance with the relatively low photocarrier mobility with a value of 0.001 cm^2 V^{-1} s^{-1} for Zn(II)porphyrin and DPA-Zn(II)porphyrin Zn-SURMOF 2 obtained from the analysis of FP-TRMC data. This low mobility will lead to very short exciton diffusion length, resulting in low charge-separation efficiency. As a result, recombination of holes and electrons will dominate, thus explaining the rather small overall efficiency for the Zn(II)porphyrin SURMOF-2-based photovoltaic devices.

4.2.4 Summary

The attachment of diphenylamine groups into porphyrin to construct MOF thin film materials will enhance solar light absorption and generate higher photocurrent. However, the conversion efficiency in the presented work is still very low due to the relatively low photocarrier mobility,

as well as recombination of light induced electrons and holes within the Zn(II)porphyrin Zn-SURMOF 2 materials. Nevertheless, these findings will be helpful for further improvement of the energy conversion efficiencies of MOF thin film based photovoltaic devices by designing porphyrin based chromophores.

4.3 C$_{60}$-fullerene loaded porphyrin-based SURMOF

4.3.1 Background

To satisfy the requirement of new generation of photovoltaic devices, scientists have been searching for new molecular materials, which should be characterized by a large absorption coefficient, fast process of charge separation and much slower process of charge recombination.[196] One of the most remarkable progresses is constructing an effective electron donor-acceptor system. In the dye sensitized solar cell (DSSC), the dyes are excited by absorbing the photons and leading to a rapid formation of separated electron-hole pairs at the interface of a dye-semiconducting electrode. Then the separated charges move towards the respective electrodes, therefore yielding a photocurrent in an external circuit.[197] Such a system is very important not only in electronic technologies but also in the life sciences such as e.g. respiration, photosynthesis and photomedicine.[196]

Among the donor-acceptor systems, porphyrin-fullerene systems are one of the widely studied classes of compounds due to their rich photo- and redox chemistry.[134] Porphyrins, addressed as the pigment of life, serve as photosensitizing electron donors. The C$_{60}$-fullerene is a very attractive electron acceptor with its ability to accept up to six electrons per molecule and unique three dimensional delocalized π-electron systems.[198] In the electron-transfer process, C$_{60}$-fullerene gives rise to an efficient and rapid photo induced charge separation and slow charge recombination in the dark, resulting in the formation of long-lived charge-separated states.[199] Thus, it is attractive to introduce C$_{60}$-fullerene into the framework to form an electron donor-acceptor system to improve the solar conversion efficiency of porphyrin-based SURMOF.

Up to now, there are many studies that successfully introduced nanoparticles or clusters into MOFs,[200,201] even MOF thin films.[202,203] The conventional procedure for loading of nanoparticles, clusters or functional groups into SURMOFs is post-synthetic, which means the loading process is performed after the preparation of the SURMOFs. This requires the sizes of nanoparticles, clusters or functional groups or the precursors to be suitable to the pore size of MOFs to enter. In the case of free base porphyrin Zn SURMOF 2 (Figure 4.30 (a)), the layer distance is 6.6 Å and the distances of adjacent porphyrin molecules are 6.88 Å and 6.49 Å, respectively. The diameter of C$_{60}$ is 7.1 Å (Figure 4.30 (b)), which is larger than the voids of porphyrin SURMOF. Therefore, it is impossible to insert the C$_{60}$-fullerene into the pores of the

synthesized porphyrin SURMOF by the conventional method. Here, a novel loading approach is proposed, where the C_{60}-fullerene is mixed in the ligand solution, to synthesize free base porphyrin Zn SURMOF 2 loaded with C_{60} (C_{60}@free base porphyrin SURMOF). The structure of the obtained C_{60}@free base porphyrin SURMOF was proposed as Figure 4.30 (c) as well as the simulated XRD data (Figure 4.30 (d)) according to the lowest energy principle. The porphyrin molecules are distortion after the introduction of C_{60} in the frameworks, which brings the change of the diffraction peak. The detailed synthesis procedure of free base porphyrin SURMOF loaded with C_{60} was described in Chapter 3.4.3.
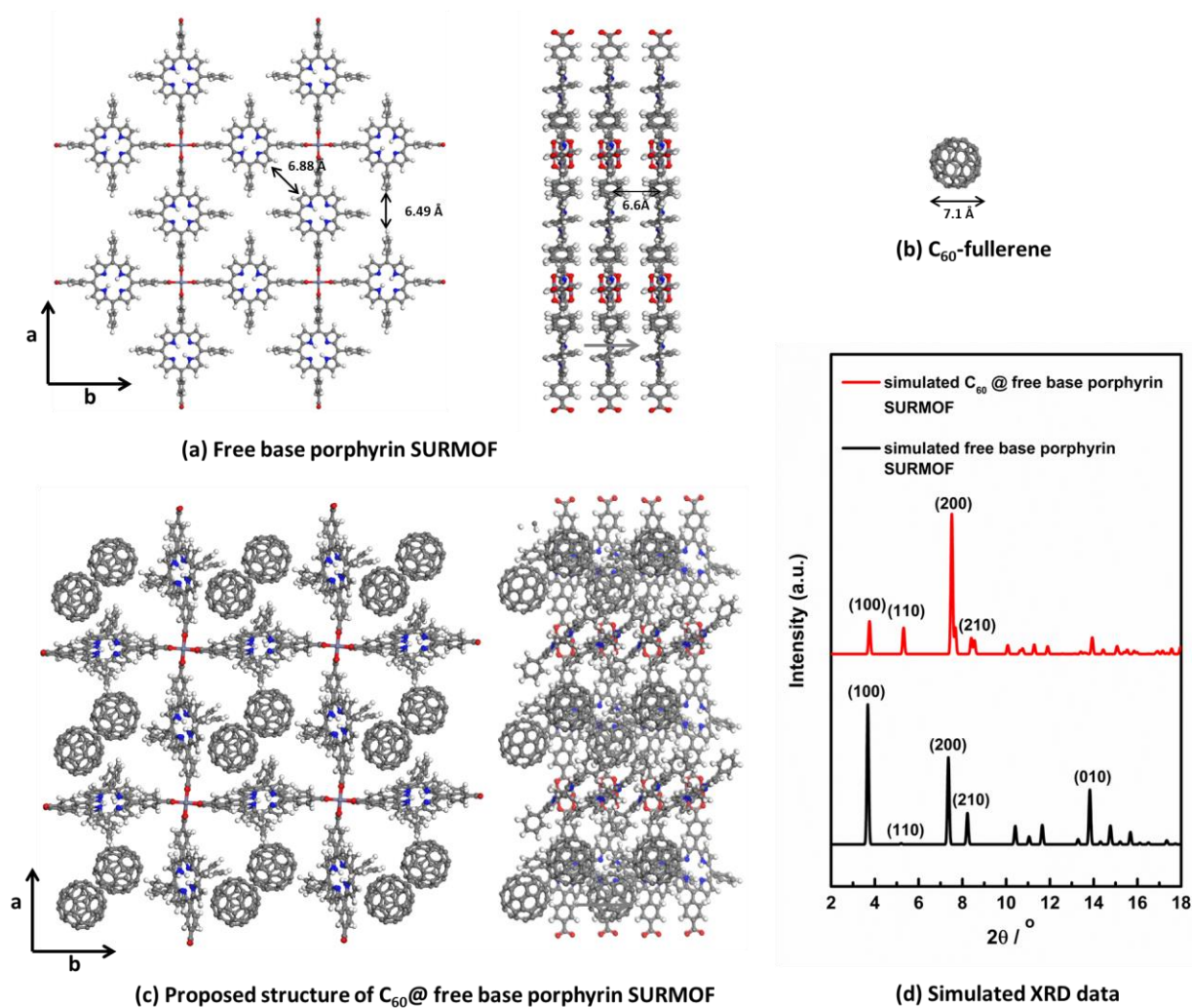
Figure 4.30 Structure of (a) free base porphyrin SURMOF, (b) C_{60}-fullerene, (c) C_{60}@free base porphyrin SURMOF (proposed by Dr. Matthew Addicoat from Jacoba-University Bremen) and (d) simulated XRD data

4.3.2 Characterization of C_{60}@free base porphyrin SURMOF

The C_{60}@free base porphyrin SURMOFs were prepared at different concentration ratio of C_{60} and porphyrin in the ligand solution. When the concentration ratio of C_{60} and porphyrin in the ligand solution is x, the obtained composite is labeled as $(C_{60})_x$@free base porphyrin SURMOFs, where x ranges from 0.25 to 2 in this study.
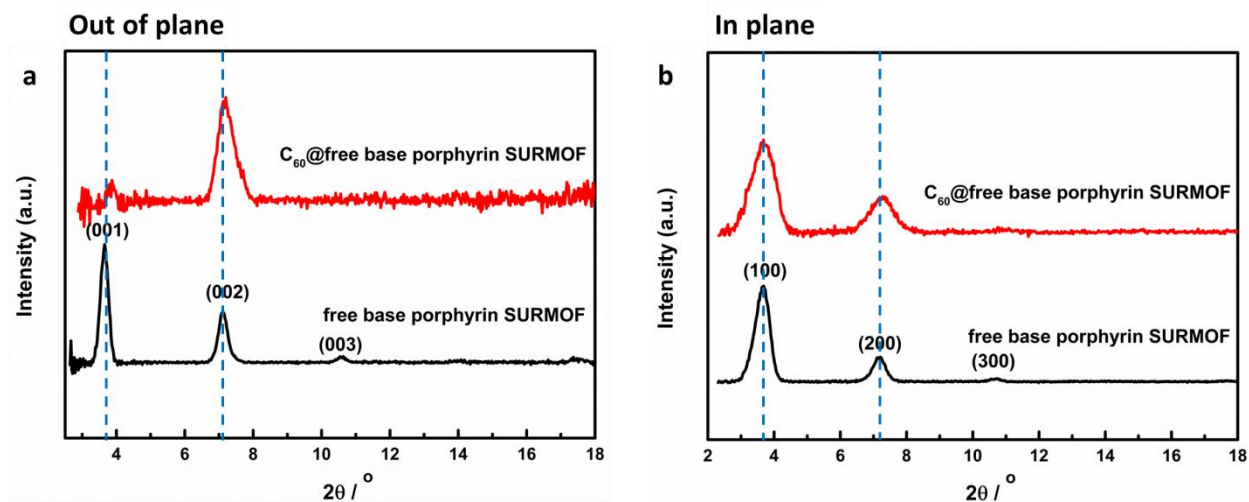
Figure 4.31 (a) Out of plane and (b) in plane XRD data of free base porphyrin Zn SURMOF 2(in black) and C_{60}@free base porphyrin Zn SURMOF 2 (in red) on MHDA SAM

The XRD data of free base porphyrin SURMOF and C_{60}@free base porphyrin SURMOF growth on MHDA SAM functionalized Au substrates is displayed in Figure 4.31, which proves that the crystallinity exists before and after loading with C_{60}. The C_{60}@free base porphyrin SURMOF growth proceeds along the [001] crystallographic direction, which is the same as the free base porphyrin SURMOF (Figure 4.31 (a)). The introduction of C_{60} brings the change of the ratio of the diffraction peak intensities. The (001)/(002) (out-of-plane data) ratio decreased compared to the empty free base porphyrin SURMOF, which is in agreement with the simulated data (Figure 4.30 (d)). This change of structure amplitude confirms that host molecules are loaded in the pore of the MOF, e.g. a decoration of only the outer surface can be excluded, which would not lead to a change of the XRD structure amplitude.[203] Since the samples are prepared on the Au substrates, it is precise to calibrate the peak position by Au, which appears at 38.2 °. After calibration by Au, the peak (001) shift a little to higher 2θ-angle after loading with C_{60},

indicating a little contraction of the structure, which maybe come from the distortion of the structure.

From the in plane XRD data (Figure 4.31 (b)), the ratio of the two peaks (100)/(200) also decreases after the introduction of C_{60} into the frameworks. There is no shift in the peak positions, which means no contraction and expansion in the b and c direction, see as Figure 4.32. However, the diffraction peaks broaden after the introduction of C_{60}, which indicates that the non-uniform strain forms.
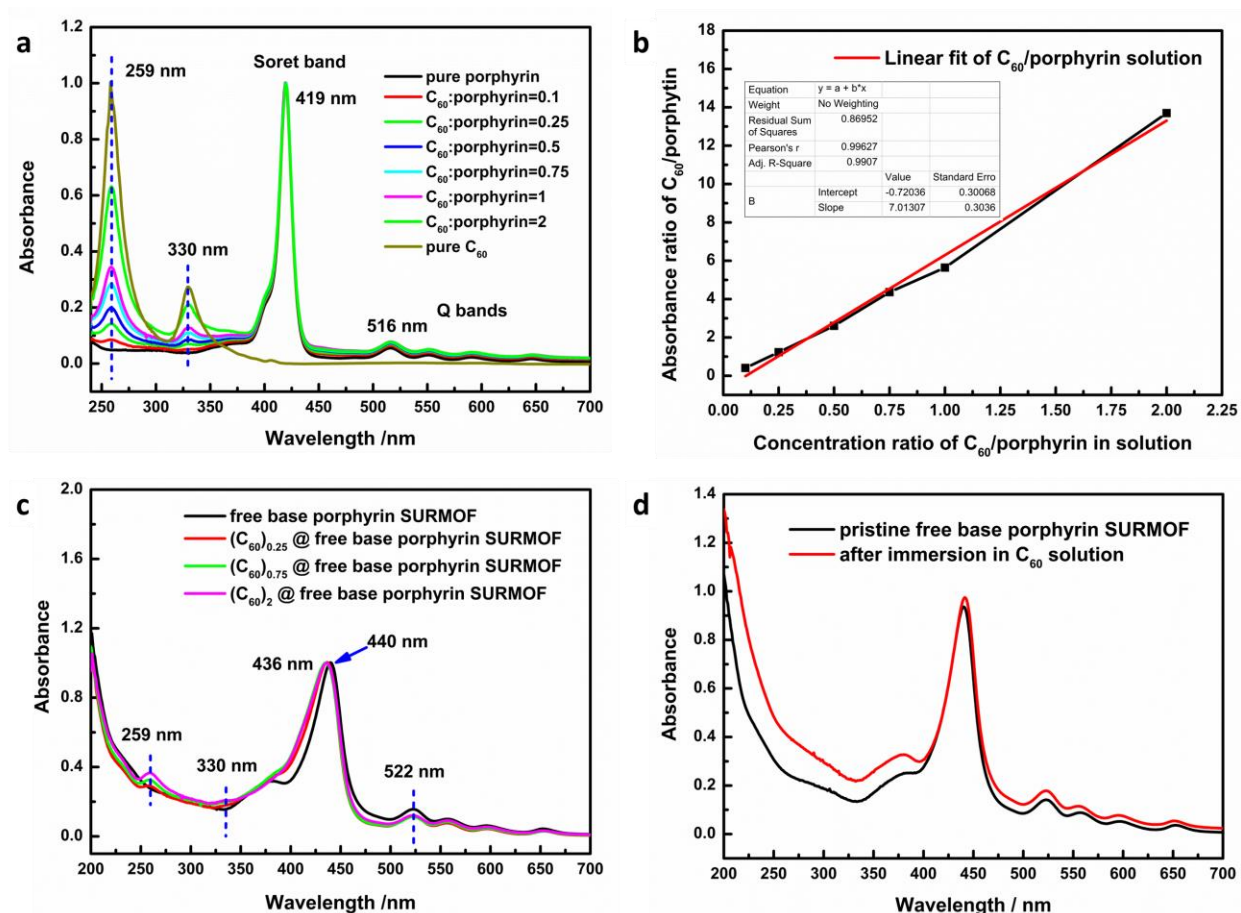
Figure 4.32 UV-Vis spectra of (a) C_{60} and porphyrin in solution and (b) the corresponding linear fit. UV-Vis spectra of (c) free base porphyrin Zn SURMOF 2 and $(C_{60})_x$@free base porphyrin SURMOFs, where x=0.25, 0.75 and 2 on quartz, (d) free base porphyrin SURMOF immersion in C_{60} solution

To further confirm the introduction of C_{60} in the voids of porphyrin SURMOF, UV-Vis spectra were carried out (Figure 4.32). Figure 4.32 (a) shows the UV-Vis spectra of C_{60} and porphyrin in solution, where C_{60} and porphyrin has different ratio of concentration, as well as pure porphyrin and pure C_{60}. C_{60} molecule exhibits two distinct bands at 259 nm and 330 nm, respectively. The detailed description of the bands from porphyrin was summarized previously in Table 4.1. According to Beer-Lambert law (equation 4.3), where A is the absorbance of the sample, ε is the molar absorptivity, l is the length which the light passes through and c is the concentration of the samples, the absorbance has a linear relationship with the concentration of the sample. Thus, the band at 259 nm from C_{60} and the Q band at 517 nm from porphyrin are taken to calculate the absorbance, leading to a linear relationship between the absorbance ratio and the concentration ratio of C_{60} and porphyrin (Figure 4.32 (b)).

$$A = \varepsilon l c \tag{4.3}$$

The UV-Vis spectra of the free base porphyrin Zn SURMOF 2 and C_{60}@free base porphyrin Zn SURMOF 2 growth on quartz glass are shown as Figure 4.32 (c). Obviously, two extra bands, 259 nm and 330nm, appeared in $(C_{60})_x$@free base porphyrin SURMOFs, which are attributed to C_{60}. Compared with the molecules in solution, the bands of C_{60} have no shift, while the bands of porphyrin shift to high wavelength, resulting from the expanded π-conjunction of the porphyrins constructed into highly oriented and ordered MOF structure.[171] What's more, the Soret band of porphyrin shifts from 440 nm to 436 nm after the introduction of C_{60} in the frameworks. The intensities of these two bands increase with the increase of the concentration ratio of C_{60} and porphyrin. Based on Beer-Lambert law and the obtained linear fit of the relationship between the absorbance ratio and the concentration ratio of C_{60} /porphyrin (Figure 4.32 (b)), the approximate ratio of C_{60} and porphyrin molecules in the frameworks could be calculated. The approximate porphyrin and C_{60} ratio is 6, 5 and 4 corresponds to *x* of 0.25, 0.75 and 2, respectively.

In comparison to the mixed solution spraying method loading C_{60}, the free base porphyrin SURMOF growth on quartz was immersed in C_{60} toluene solution for 12 h. After rinsing with ethanol, the sample was taken to perform UV-Vis measurement, shown as Figure 4.32 (d). There is no change in the spectra, indicating no C_{60} molecules were involved into the frameworks.

Figure 4.33 shows the morphology and cross-section SEM images of empty free base porphyrin Zn SURMOF 2 and C_{60}@ free base porphyrin Zn SURMOF 2. From the top view, the porphyrin SURMOF thin film consists of uniform fiber. After loading with C_{60}, there seems much aggregation appearing. From the cross-section, both samples exhibit quite compact films. The thickness has no change for both samples at the same spraying cycle.

(a) free base porphyrin Zn SURMOF 2   (b) C_{60}@ free base porphyrin Zn SURMOF 2
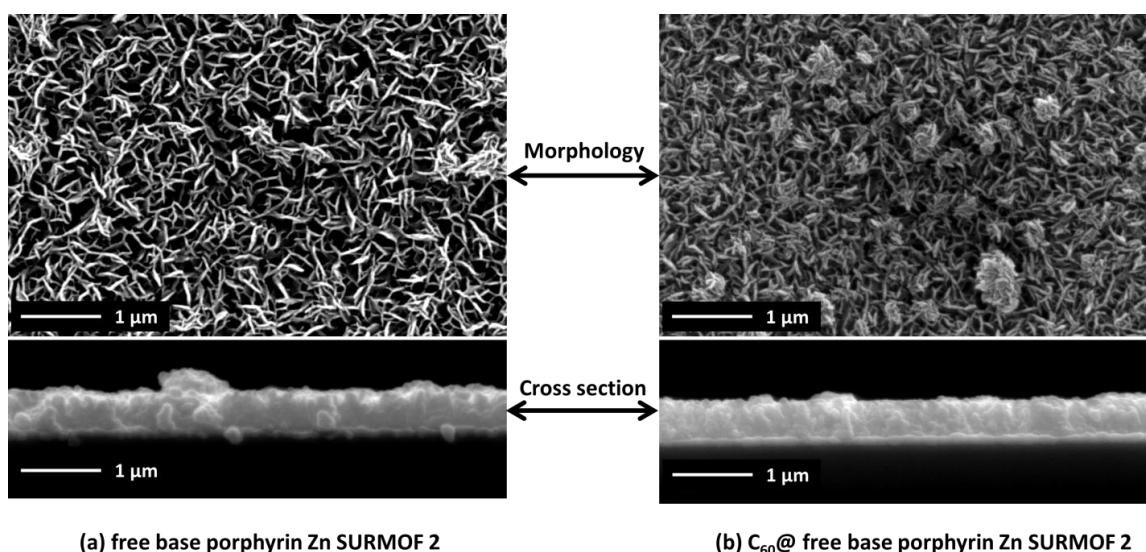
Figure 4.33 Top view and cross-section SEM images of (a) free base porphyrin Zn SURMOF 2 and (b) C_{60}@free base porphyrin Zn SURMOF 2

4.3.3 Photocurrent measurement

In order to investigate the influence of the C_{60} to the porphyrin SURMOF, the photocurrent measurements were carried out under the illumination of light using a three-electrode system. The setup is the same as Figure 4.8, where FTO glass assembled with the MOF film was used as the working electrode, a Pt coated FTO substrate as counter electrode, a Pt wire as the reference electrode and an I^-/I_3^- solution as the electrolyte.

The photocurrent was obtained when the light was switched on and off with an applied bias voltage of 0.06 V vs Pt wire electrode. The photocurrent response under the illumination of different wavelength light, on-off response under illumination of 530 nm free base porphyrin Zn-SURMOF 2 and $(C_{60})_x$@ free base porphyrin SURMOFs are displayed in Figure 4.34. All the samples exhibit quick response to the light. The introduction of C_{60} improves the photocurrent under the wavelength covering the whole range. The photocurrent density generated at 530 nm is

enhanced from 13.5 $\mu A\ cm^{-2}$ for free base porphyrin SURMOF to 20.8 $\mu A\ cm^{-2}$ for $(C_{60})_{0.25}@$ free base porphyrin SURMOF, even as high as 25 $\mu A\ cm^{-2}$ for $(C_{60})_2@$ free base porphyrin SURMOF. Nevertheless, the results are in expectation and it is true that the higher concentration C_{60} involved into the frameworks, the larger is the photocurrent of the frameworks.
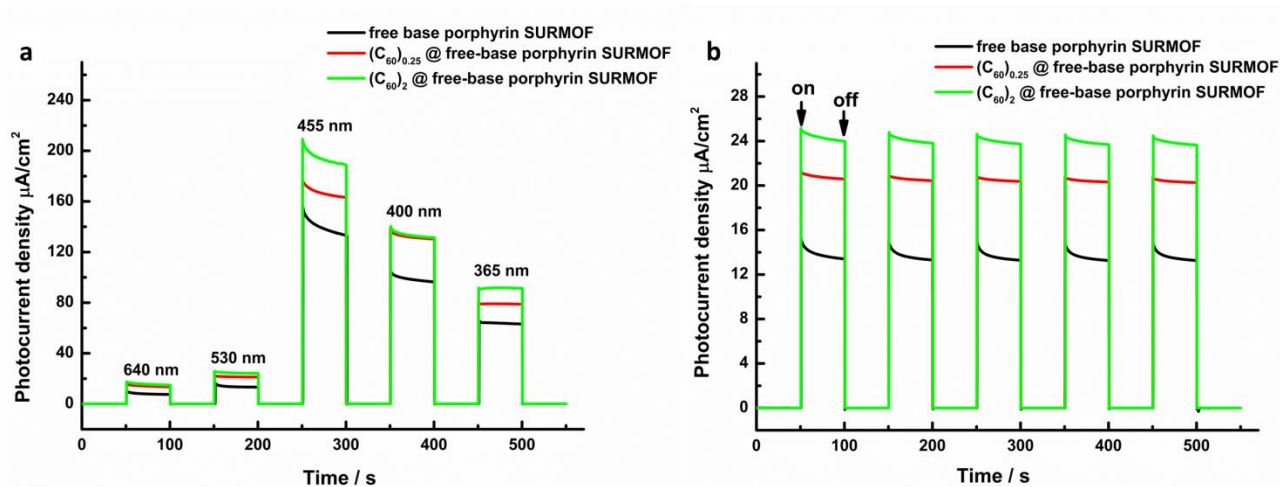
Figure 4.34 Photocurrent response of free base porphyrin Zn SURMOF 2 and $(C_{60})_x@$free base porphyrin SURMOFs, where x=0.25 and 2 on FTO at different wavelength (a) and (b) on-off illumination under 530 nm.

4.3.4 Summary

A novel method was proposed to load C_{60} into the porphyrin SURMOF, where C_{60} was mixed with the porphyrin solution and sprayed as a mixture. The UV-Vis provided the direct evidence of the presence of C_{60} in the porphyrin SURMOF. The introduction of C_{60} led to the distortion of the porphyrin in the frameworks. The loading of C_{60} enhanced the photocurrent performance of the porphyrin SURMOF. The study provides the feasibility to load C_{60} or other acceptors into the porphyrin frameworks to improve the photophysical properties.

5 Post-synthetic modification of porphyrin-based SURMOF and the preparation of porphyrin SURGEL

5.1 Background

As described in Chapter 4, crystalline, monolithic and homogeneous porphyrin-based MOF films can be achieved by LPE process in a layer-by-layer fashion.[192] To realize the functionality of porphyrin MOFs, post-synthetic modification (PSM) is a primary choice since it affords a more diverse range of functional groups to optimize certain properties.[102] PSM achieves the functionality of MOFs by covalently reacting molecules into the framework. It is based on the functional groups, such as $-NH_2$, $-OH$, $-NO_2$ and $-N_3$, incorporated in the MOFs. It has been proved that the functionalization of SURMOF thin films can be readily achieved by PSM via azide-alkyne cycloaddition.[103]

In this chapter, a functional porphyrin, 5,15-diphenylazido-10,20- di(4-carboxyphenyl)porphyrin (N_3-porphyrin), was used as the ligand to construct SURMOF. Then the PSM of the obtained N_3-porphyrin SURMOF was performed via the strain-promoted azido-alkyne cycloaddition (SPAAC). Furthermore, a so-called porphyrin surface-grafted gel (SURGEL) was also prepared by the cross-linking of N_3-porphyrin SURMOF and further removal of metal ions. SURGELs are an emerging class of porous polymer films, which came up in the recent two years.[104] Since the SURGELs are derived from the SURMOFs via PSM, they bear some properties of MOFs, such as high degree of structural and functional tunability.[204] On the other hand, the metal-free covalently connected gels afford the pronounced stability against water.[104] Although the studies regarding to the SURGELs are rare at the moment, the SURGELs have exhibited high potential for electrochemical applications[106] and biology.[104,105] Thus, the successful preparation of porphyrin SURGEL not only offers the opportunity to control the generation of singlet oxygen in photodynamic therapy, but also allows the bioactive compounds within the pores to achieve tailorable properties.

5.2 Characterization of N_3-porphyrin Zn-SURMOF 2

The N_3-porphyrin Zn-SURMOF 2 was deposited on Au substrates functionalized by COOH-terminated organothiolate. The detailed synthesis of porphyrin SURMOF is described in Chapter 3.5.1. The out of plane XRD data of the N_3-porphyrin Zn-SURMOF 2 is shown in Figure 5.1,

where the inset is the molecular structure of N$_3$-porphyrin. The XRD result proved that the N$_3$-porphyrin Zn-SURMOF 2 was successfully grown on COOH- terminated organothiolate modified gold substrate with highly crystalline in a preferred [001] orientation, which shows a similar structure of other porphyrin Zn-SURMOF 2 in the previous chapters.
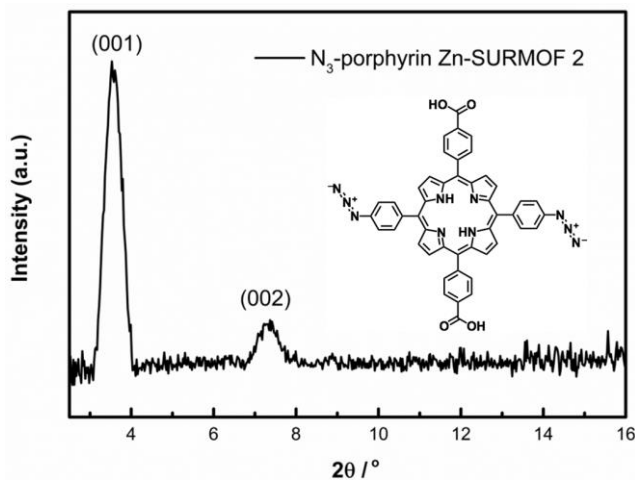
Figure 5.1 Out of plane XRD data of N$_3$-porphyrin Zn-SURMOF 2. Inset is the structure of N$_3$-porphyrin molecule.

5.3 Post-synthetic modification of N$_3$-porphyrin Zn-SURMOF 2

The PSM of the N$_3$-porphyrin Zn-SURMOF 2 is based on the strain-promoted azido-alkyne cycloaddition (SPAAC) between the azide groups and the alkyne moiety of the cyclooctyne derivative.[103] The reaction scheme is shown in Figure 5.2. Concerning the post-modification, the obtained N$_3$-porphyrin Zn-SURMOF 2 was immersed into a toluene solution containing the cyclooctyne derivative compound overnight in dark at 80 ℃ under a reflux atmosphere. After the reaction, the substrate was thoroughly rinsed with acetone and ethanol and dried under nitrogen flow. To confirm the reaction, the sample was characterized using IRRAS and XRD.
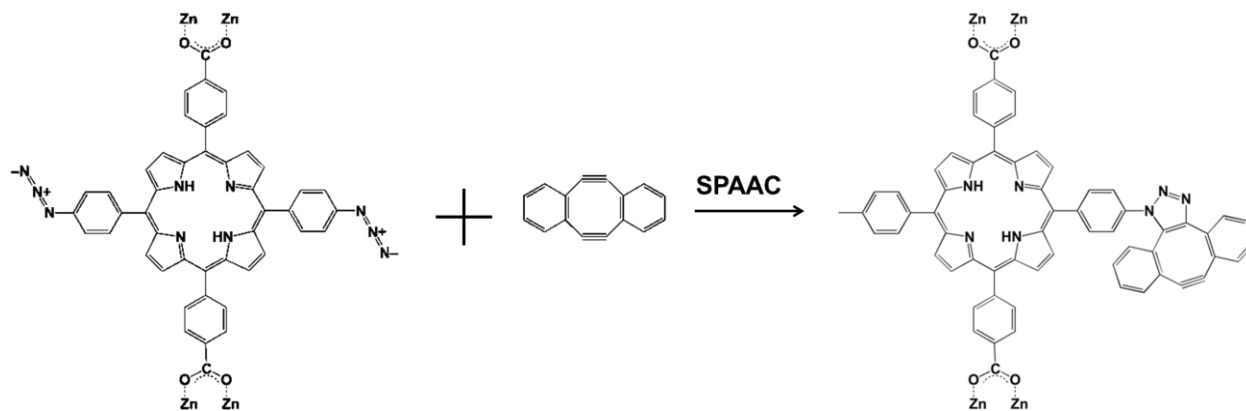
Figure 5.2 Click-reaction of N₃-porphyrin ligands using SPAAC.
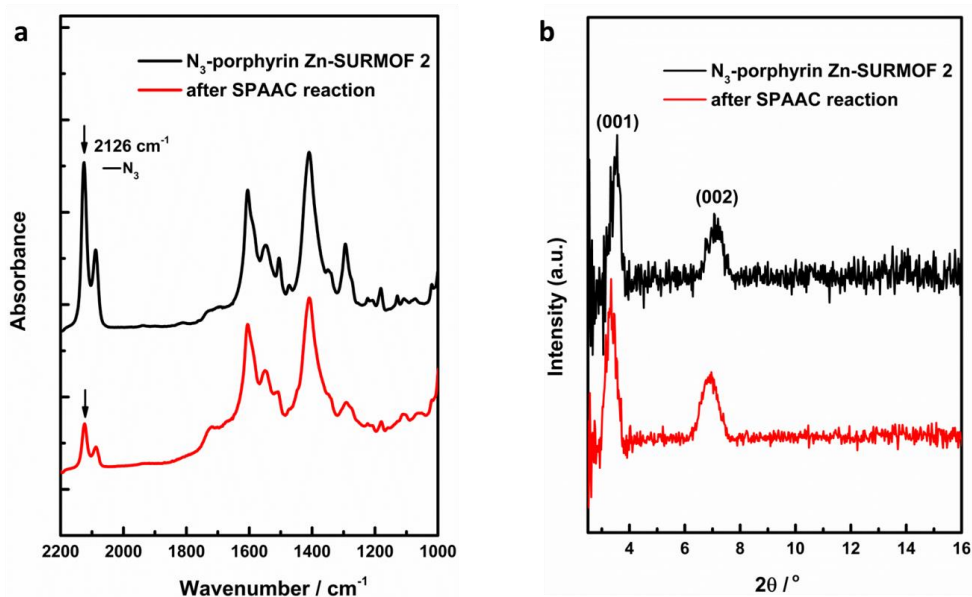
Figure 5.3 (a) IRRAS spectra and (b) XRD data of the pristine N₃-porphyrin SURMOF-2 (in black) and after SPAAC reaction (in red)

The successful SPAAC reaction was evidenced by the IRRAS data (Figure 5.3(a)), where the azide band at 2126 cm^{-1} from the N₃-porphyrin ligand in the SURMOF decreased after the reaction. The XRD data revealed the presence of the highly crystalline porphyrin SURMOF before the reaction and the SPAAC reaction does not show any significant change in the XRD pattern. Based on the above observations, we can conclude that the successful post-synthetic modification of porphyrin SURMOFs via strain-promoted alkyne-azide click chemistry was

successfully performed without destroying the crystalline MOF structure. After reaction for 12h, the conversion yield reached 75%.

5.4 Characterization of porphyrin SURGEL

When the obtained N_3-porphyrin Zn-SURMOF 2 is immersed in an electron-deficient alkyne cross-linker solution, the coupling of the azide groups in the frameworks with the alkyne groups spontaneously takes place at room temperature.[205] The copper-free click reaction scheme of N_3-porphyrin and trimethylolethane tripropiolate which serves as the cross-linker is shown in Figure 5.4. To remove the Zn ions from the framework, the sample was immersed in ethylenediaminetetraacetis acid (EDTA) solution. The detailed description of the synthesis for N_3-porphyrin Zn-SURMOF 2 and porphyrin SURGEL is found in Chapter 3.5.2.
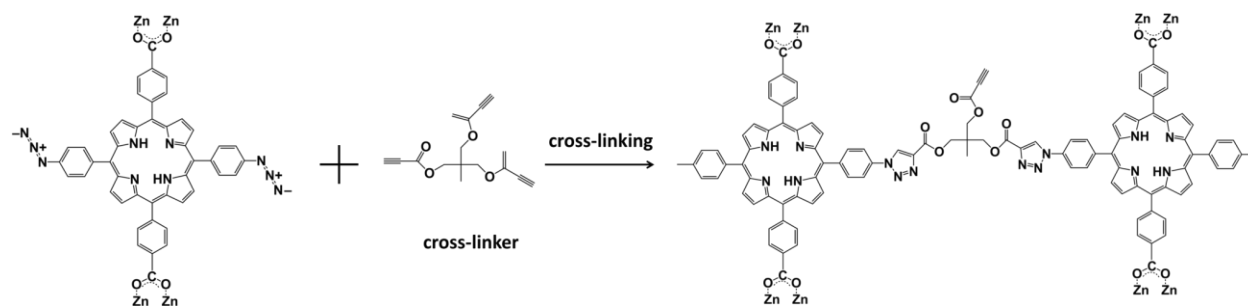
Figure 5.4 Copper-free click reaction between the N_3-porphyrin and trimethylolethane tripropiolate (cross-linker)

To confirm the successful coupling reaction of the azide groups and alkyne groups, the IRRAS were carried out (Figure 5.5 (a)). The band at 2127 cm^{-1} is assigned to the azide groups from the N_3-porphyrin linker, which substantially decreased after the coupling reaction. The alkyne-band from the cross-linker is overlapped with the band of azide groups.[104] Meanwhile, the band at 1730 cm^{-1} and 1236 cm^{-1} appeared, which are both assigned to carbonyl C=O stretching contained in the cross-linker. The observation confirmed the incorporation of the alkyne cross-linker into the SURMOF framework. After immersing in the EDTA solution, aiming to remove the metal ions, the carboxylate bands at 1590 cm^{-1} and 1404 cm^{-1} almost disappeared, which indicated that the carboxylate groups were no longer coordinated to the zinc ions.
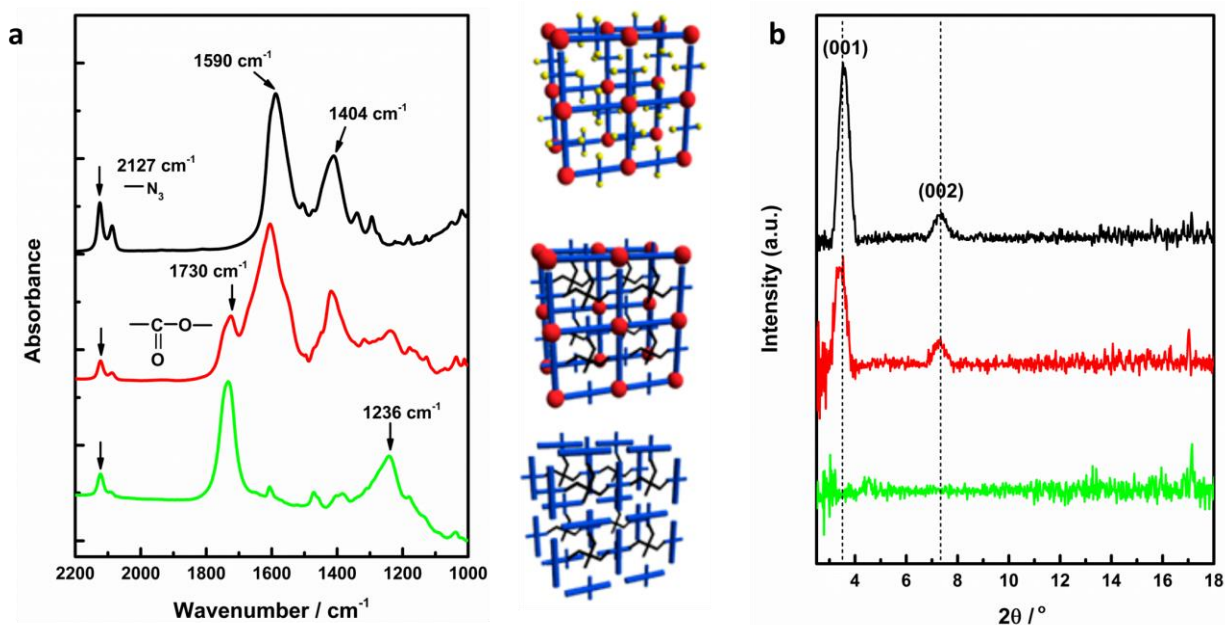
Figure 5.5 (a) IRRAS spectra and (b) XRD data of the cross-linking process within the porphyrin SURMOF-2 structure before the cross-linking reaction (top), after the cross-linking (middle), and after treatment with EDTA for 30 min (bottom) (Frameworks taken from Ref.[104]).

The XRD data (Figure 5.5(b)) showed highly crystalline porphyrin SURMOF and the crystallinity still remained after cross-linking of the framework. Upon removal of the zinc ions from the cross-linked SURMOF, the corresponding XRD data did not show any diffraction signals, indicating the structure was transformed into an amorphous SURGEL.

The SEM images of the cross-linking process within the porphyrin SURMOF-2 structure were carried out using Zeiss Ultra plus Scanning Electron Microscope, shown in Figure 5.6. The pristine N_3-porphyrin SURMOF shows uniform structure (top). After cross-linking (middle), the morphology shows no much change, which is still crystalline from the XRD data. After treatment with EDTA for 30 min (bottom), the SURGEL is formed. The structure of the SURGEL collapses and is flexible, resulting in non-crystalline structure.
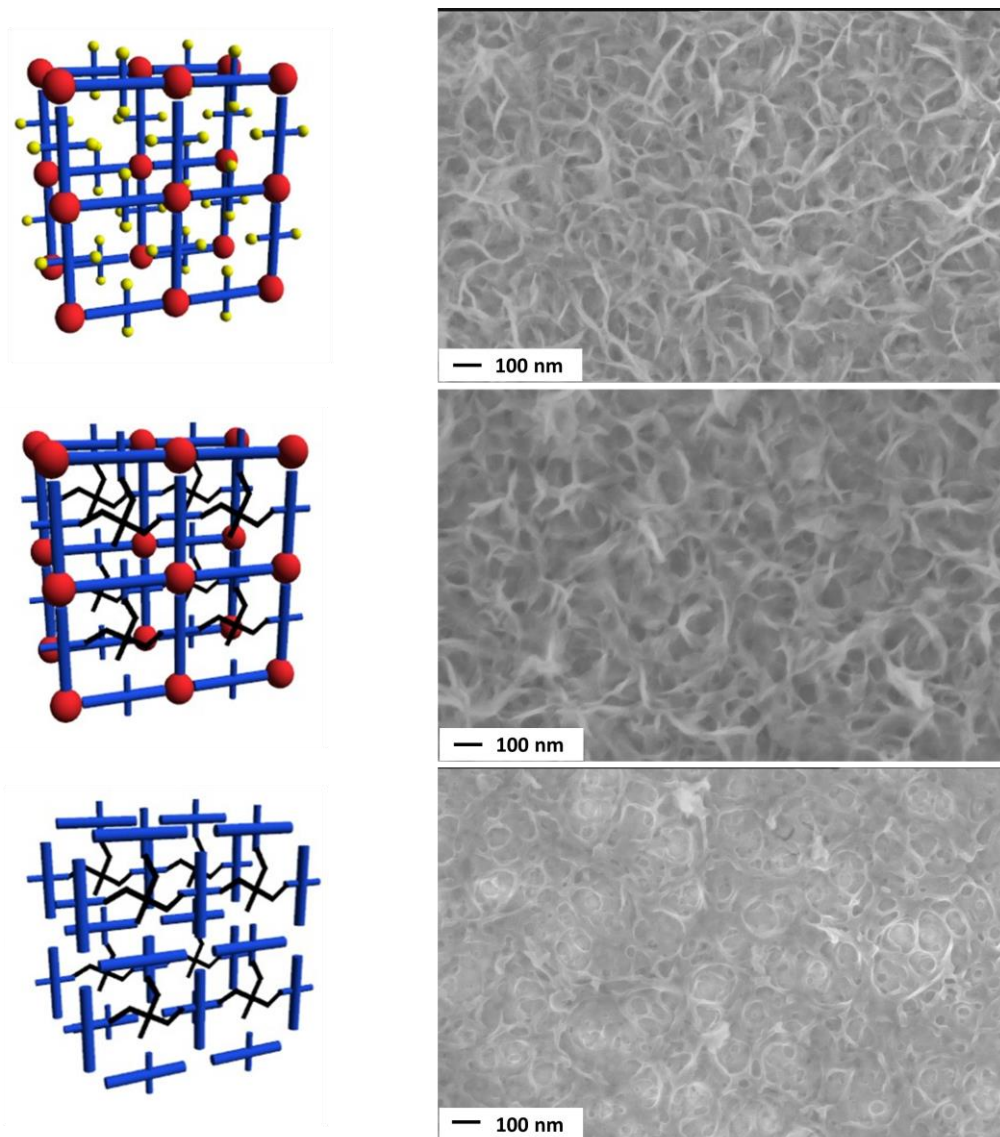
Figure 5.6 SEM images of the cross-linking process within the porphyrin SURMOF-2 structure before the cross-linking reaction (top), after the cross-linking (middle), and after treatment with EDTA for 30 min (bottom) (Frameworks taken from Ref.[104]).

To confirm the porphyrin-based compounds, UV-Vis spectroscopy is a useful characterization due to the conjugated structure. Thus, the N_3-porphyrin SURMOF growth on quartz glass was converted to SURGEL for the UV-Vis measurement. The UV-Vis spectra of N_3-porphyrin Zn-SURMOF 2 growth on quartz glass and the porphyrin SURGEL on quartz glass are displayed in Figure 5.7. The observation provides direct evidence of the existence of porphyrin in the SURGEL thin film. Compared with the N_3-porphyrin Zn-SURMOF 2, the Soret band of the

porphyrin SURGEL shifts 9 nm to the lower wavelength, which is due to the absence of coordination of the metal ions.
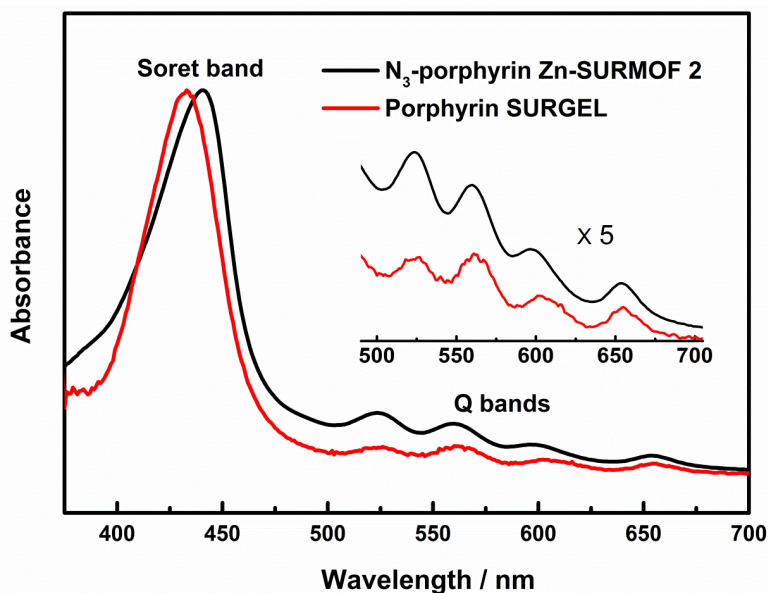
Figure 5.7 UV-Vis spectra of N₃-porphyrin Zn-SURMOF 2 (in black) and porphyrin SURGEL (in red) on quartz glass. Inset is 5 times magnification of the Q bands.

5.5 Summary

In this chapter, the porphyrin-organic linkers with azide functional groups were used to prepare the azido-porphyrin SURMOFs and the XRD results confirmed that the obtained structure was highly crystalline and grown in (001) orientation. The successful modification of the N₃-porphyrin SURMOF using SPAAC was also proved by XRD and IRRAS in this chapter, reaching a conversion yield of 75% after 12 h. This experiment offers a robust platform for attaching various types of functional units into the frameworks. In addition, porphyrin SURGEL was successfully prepared via cross-linking of N₃-porphyrin SURMOF using alkyne-azide click chemistry and further removing the metal ions by EDTA solution. The obtained SURGEL can be further functionalized since the alkyne moieties are still available for the post-synthetic modifications after the SURGEL formation,[106] which show great potential for additional applications, for example, to realize an electron donor-acceptor system for photovoltaic device.

6 Liquid- and gas-phase diffusion of ferrocene in SURMOFs

6.1 Background

One important application of MOFs is guest adsorption, the quantitative information of adsorption and diffusion of guest molecules within MOFs is crucial for exploring the mechanisms governing the migration of molecules through the voids of the porous structure.[206] Therefore, the mass transport of molecules inside MOFs, which is generally characterized by the diffusion coefficient, is an important evaluation among the performances of MOFs. Up to now, the gas diffusion of various molecules in different MOF structures has been intensively studied,[207-209] as well as a few liquid diffusion cases.[210,211] However, a comparison between the gas and liquid mass transfer properties in the MOF is lacking. Among the techniques reported for measuring diffusivity in MOFs,[206,210,212-214] QCM approach has been demonstrated to determine the diffusion constants as low as 10^{-19} m^2 s^{-1}, which is suited for MOFs.[206] Additionally, the SURMOF prepared in a well-defined layer-by-layer fashion is uniform and thickness controlled, which provides the opportunity for quantitative analyzing dynamic phenomena within MOFs.

In this chapter, the QCM method was applied to investigate the probe molecule uptake in SURMOF thin films. The probe molecule, ferrocene (Fc), was dispersed in a carrier gas or dissolved in ethanol or hexane for the gas- and liquid- phase diffusion, respectively. The diffusion of both the phases was carried out with the identical SURMOF sample of HKUST-1.

6.2 Gas- and liquid- phase adsorption of ferrocene in HKUST-1

The HKUST-1 (represented in Figure 1.3) SURMOFs were prepared on the MUD SAMs functionalized QCM sensors by the LPE spraying method (Chapter 3.6). The X-ray diffractogram of HKUST-1 SURMOF confirms crystalline oriented growth, as shown in Figure 6.1. The diffraction reflexes at 5.8 ° (111), 11.6 ° (222), 17.5 ° (333) and 23.3 ° (444) demonstrate the crystallinity of the HKUST-1 SURMOF as well as the oriented growth in [111] direction.
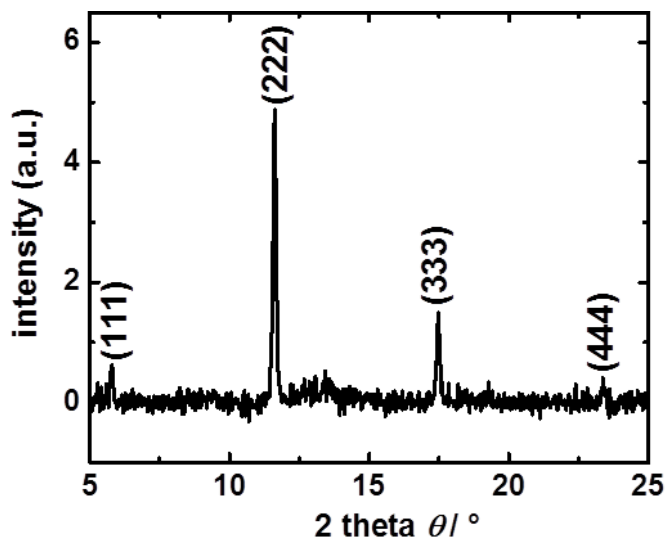
Figure 6.1 X-ray diffractogram of the HKUST-1 SURMOF.

The mass change of the sample on the QCM sensor can be determined by the Sauerbrey equation (Equation 2.4). The sample thickness was determined from the change of the resonance frequency f_1 of the QCM sensor before (4,952,150 Hz) and after (4,951,556 Hz) the SURMOF synthesis. A SURMOF mass of 10.5 μg cm^{-2} was determined, which corresponds to a SURMOF thickness of about 100 nm considering the known density of the achieved HKUST-1 is about 0.98 g cm^{-3}.

The uptake of ferrocene in the gas phase is performed by connecting a gas flow system to the QCM cell (Figure 6.2 (a)). A flow rate of 10 mL min^{-1} Ar flow was used as the carrier gas in the experiment. Before the adsorption of probe molecule, a stable baseline was achieved under Ar flow. The argon flow is firstly enriched with the vapor of the ferrocene by passing through the reservoir of the guest molecules. Ferrocene possesses a saturation vapor pressure of about 1 Pa at room temperature.[215] The enriched gas flow is then passed through the QCM cell, where the guest molecules diffused into the SURMOF permitting the uptake to be studied by the mass change of the SURMOF on the QCM sensor. It should be noted that the concentration of argon in MOFs of type HKUST-1 at room temperature and a pressure of about 1 bar is very small. Therefore, the argon molecules in the pores as well as the diffusion of argon during the uptake of the guest molecules can be neglected and the activated MOF pores can be considered as empty.

The ferrocene uptake in the liquid phase was investigated by pumping a ferrocene solution through the QCM cell (Figure 6.2 (b)). After the stable baseline being obtained by flow of pure solvent (ethanol or n-hexane), the ferrocene solution was injected into the QCM cell. The concentration of the ferrocene in both solvents were chosen which correspond to 90% of the saturation solubilities,[216] i.e. 90 mM ferrocene in ethanol and 155 mM ferrocene in n-hexane.

To ensure that the uptake by the SURMOF in both cases is controlled by diffusion in the nanopores and not by convection through the QCM cell, the flow rates of the gases and liquids through the QCM cell need to be set large enough. In this case, 10 mL min^{-1} is set for the gas flow and roughly 1 mL min^{-1} for the liquid phase. Switching from the pure gas flow, or pure solvent, to the enriched gas flow, or solution, results in the uptake of the guest molecules into HKUST-1 SURMOF. The mass changes are recorded by the QCM.
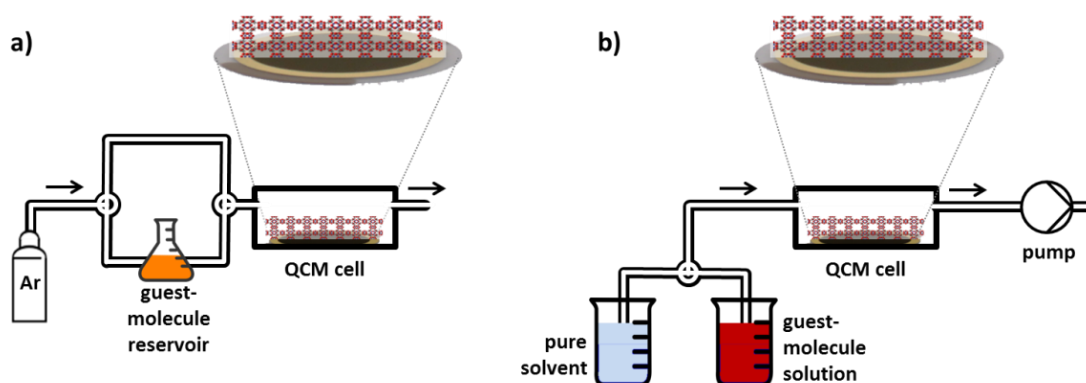
Figure 6.2 Setup of uptake experiments from the gas (a) and liquid (b) phase into HKUST-1.

The uptake of ferrocene was repeated several times to avoid the possible deviation. All experiments were performed at a temperature of 25 ℃. Before each experiment, the sample was activated in a flow of pure argon at 65 ℃ for several hours, to guarantee that no molecules, such as water, were adsorbed in the pores and to guarantee reproducible results.

6.3 Comparison of liquid- and gas-phase diffusion of ferrocene in HKUST-1

The uptake curves of ferrocene by the SURMOF recorded by QCM are shown in Figure 6.3. Figure 6.3 (a) (b) and (c) correspond to the ferrocene adsorption in Ar (gas phase), n-hexane (liquid phase), and ethanol (liquid phase), respectively. Additionally, in order to compare the

uptake kinetics, the normalized uptake by the SURMOF from in liquid and the gas phase is shown in Figure 6.3 (d).
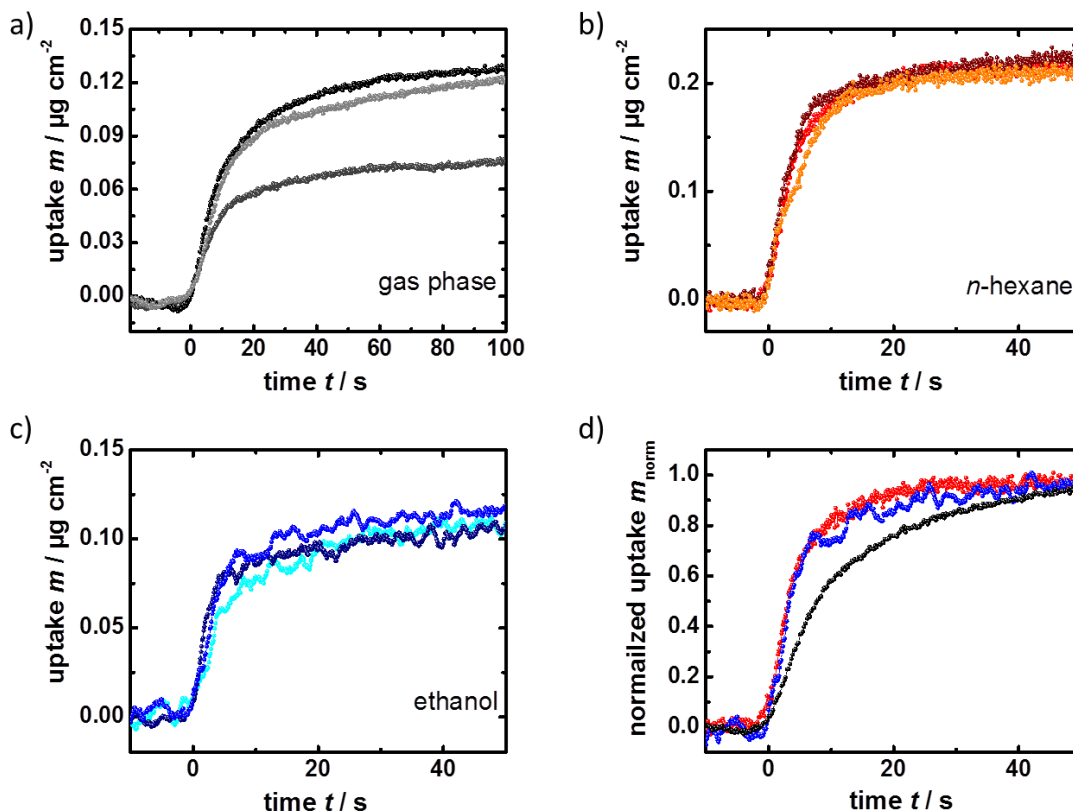
Figure 6.3 Ferrocene uptake by HKUST-1. The uptake curves of ferrocene vapor in argon carrier gas (a); of ferrocene in n-hexane (b); and of ferrocene in ethanol (c); are measured by QCM. For comparison of the uptake kinetics, the normalized uptake by the SURMOF from the liquid and the gas phase are shown in (d); black is the uptake of the ferrocene vapor, red of the n-hexanic ferrocene solution and blue of the ethanolic ferrocene solution.

The uptake curves recorded by the QCM enable an analysis of the equilibrium concentration and of the mass transfer parameter, i.e., the diffusion coefficient. Since the SURMOF pores which are activated in argon can be considered as empty, the QCM experiments allow a straightforward quantification of the uptake amount.[217,218] The ferrocene uptake is determined to be 0.11 ± 0.02 μg cm^{-2}, which corresponds to roughly 3/4 ferrocene compounds per HKUST-1 unit cell. Since ferrocene is a solid which slowly sublimates, it can be assumed that the obtained partial pressure of ferrocene is (significantly) smaller than the saturated vapor pressure of ferrocene, resulting in

an equilibrium concentration which is (much) smaller than the maximum ferrocene concentration in the MOF pores.

The uptake from the liquid phase is more complex. The pores are initially filled with the solvent. When the investigated guest molecules are diffusing into the pores, the solvent molecules are then displaced. Therefore, the determination of the uptake amount is not straightforward and requires the knowledge of the densities of the solvent in the MOF pores, with and without ferrocene. Due to the fact that the mass change is proportional to the ferrocene uptake, the recorded uptake curves can be used to investigate the kinetic properties and to determine the diffusion coefficient of the ferrocene compound in solution.

6.4 Calculation of diffusion coefficient

Approximately, the uptake by a thin film, $m(t)$, can be described by an exponential decay function:

$$m(t) = m_{eq}(1 - \exp(-\frac{t}{\tau}))$$
(6.1)

with a time constant of

$$\tau = \frac{l^2}{3D} + \frac{1}{\alpha}$$
(6.2)

where l denotes the film thickness, D is the (transport) diffusivity, α is the surface permeability, m_{eq} is the equilibrium loading and t is the time. It was demonstrated that the surface barriers, which can be described as a reduced thin layer with permeability covering the external crystal surface, are not an intrinsic feature of metal-organic frameworks as pristine films do not exhibit these limitations.[219] Thus, the surface barriers are neglected and the diffusion coefficient is expressed by[220]:

$$D = \frac{l^2}{3\tau}$$
(6.3)

It was determined from the uptake curves (Figure 6.3) that the ferrocene uptake from the gas phase proceeds with an average time constant τ of 13 ± 4 s, from the n-hexanic solution with a time constant of 4.9 ± 1.1 s and from the ethanolic solutions with a time constant of 5.8 ± 1.9 s. The error denotes the standard deviation of the experimental results. By using the equation 6.3

and using the determined SURMOF thickness l of about 100 nm, the diffusion coefficient D for ferrocene in the (initially) empty MOF, i.e., of ferrocene during the uptake from the gas phase, was determined to be $(2.5 \pm 0.7) \times 10^{-16}$ m^2 s^{-1}. For the uptake from the liquid phase, ferrocene diffusion coefficients of $(6.8 \pm 1.6) \times 10^{-16}$ m^2 s^{-1} in the n-hexanic solution and $(5.6 \pm 1.8) \times 10^{-16}$ m^2 s^{-1} in the ethanolic solution were calculated. These experimental findings were reproduced by an HKUST-1 SURMOF of 110 nm thickness (sample 2), where diffusion coefficients of $(1.6 \pm 0.5) \times 10^{-16}$ m^2 s^{-1} from the gas phase, $(6.0 \pm 0.5) \times 10^{-16}$ m^2 s^{-1} from the hexanic solution and $(7.5 \pm 3.1) \times 10^{-16}$ m^2 s^{-1} from the ethanolic solution were determined, see Figure 6.4.
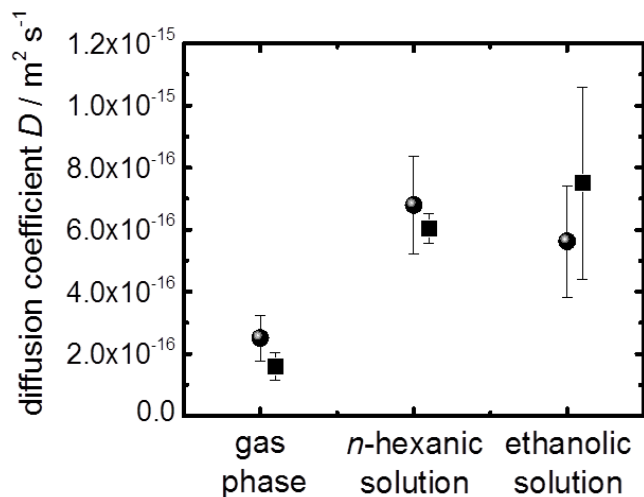
Figure 6.4 Diffusion coefficients of ferrocene in HKUST-1. The average diffusion coefficients with the respective standard deviation are shown for the ferrocene vapor in the argon carrier gas, for ferrocene in n-hexanic solution and for ferrocene in ethanolic solution. The results of both samples are shown; spheres: sample 1, squares: sample 2.

These results demonstrate that the uptake from the ferrocene solution by the solvent-filled HKUST-1 proceeds roughly 3-times faster than the uptake of the ferrocene vapor by the empty HKUST-1 framework. This is remarkable, since the solvent molecules have to leave the pores to allow the ferrocene to enter the solvent-filled MOF pores. It may be assumed that the fast diffusion in the solvent is caused by the interaction of the ethanol or n-hexane solvent molecules, which occupy attractive adsorption sites in the MOF framework. Thus, the ferrocene molecules are less strongly adsorbed in the pores and can diffuse faster through the framework. It can be assumed that the diffusion of small molecules like ethanol and n-hexane is much faster than that

of ferrocene. Therefore, the counter diffusion of the solvent molecules does not slow down the ferrocene uptake.

The pore windows of HKUST-1 have a diameter of roughly 0.9 nm, which is significantly larger than ferrocene with a kinetic diameter of about 0.66 nm.[221] The uptake of ferrocene by MOFs of type $Cu_2(ndc)_2(dabco)$ with pore window diameters of 0.57 nm was investigated.[206] There, the diffusion coefficient of ferrocene is three orders of magnitude smaller than in HKUST-1. This shows that the pore size has a dramatic impact of the diffusion properties, especially if the pore diameter and the guest molecules have a comparable size.

It should be noted that, due to the fact that the pristine samples were used directly after the synthesis, surface barriers,[222-224] which may hinder the uptake and release of the guest molecules, are neglected during the analysis of the data.[219]

6.5 Summary

The diffusion of ferrocene in MOFs of type HKUST-1 was investigated by using thin MOF films in combination with QCM. For the first time, the diffusion of the guest molecules in the gas phase, where the guest molecules are diffusing into an initially empty framework, and in the liquid phase, where the guest molecules are diffusing into a solvent-filled framework, are compared. It was found that in the MOF, the diffusion coefficient of ferrocene in the liquid- and in the gas-phase are in the same order of magnitude; with a ferrocene diffusion coefficient which is roughly 3-times smaller in the empty MOF (i.e., uptake from the gas phase) than in the liquid-filled MOF (i.e., uptake from the ferrocene solutions). It may be assumed that other liquids may have a larger impact on the diffusion and significantly slow down or accelerate the ferrocene uptake.[100]

Due to their general applicability, SURMOF films in combination with QCM show great potential for investigating the diffusion of guest molecules in MOFs. Not only the uptake from the gas and from the liquid phase can be investigated, but also guest-host systems with diffusion coefficients ranging over at least six orders of magnitude can be studied. So far, mass transfers with diffusion coefficients in the range of 6×10^{-19} m^2 s^{-1}[206] to 6×10^{-13} m^2 s^{-1}[219] have been investigated. It might be assumed that even slower or faster diffusion processes can be

investigated, for instance by fully utilizing the time resolution and by increasing or decreasing the SURMOF thickness.

7 Conclusions

A series of porphyrin-based SURMOFs were successfully produced on various substrates using liquid phase epitaxy (LPE) method in a layer-by-layer fashion. The prepared porphyrin-based SURMOFs were characterized by XRD and determined to be SURMOF 2 structure, with parallel 1D channels and layers perpendicular to the substrates. The photophysical properties of the highly oriented, crystalline, homogeneous thin films were investigated in detail.

Free base porphyrin and Pd metalized porphyrin SURMOF, which showed difference of the symmetry change of the porphyrin structure, were prepared on transparent and conductive FTO substrates, assembled into photovoltaic devices in a FTO/SURMOF/ (I^-/I_3^-)/Pt/FTO geometry. The free base porphyrin Zn-SURMOF 2 and Pd porphyrin Zn-SURMOF 2 exhibited the solar conversion efficiencies of 0.2% and 0.45%, respectively. The better performance of the Pd-system was attributed to the high charge carrier generation efficiency. Further calculations proved that the porphyrin SURMOF 2 structure should be classified as an indirect band-gap semiconductor. The indirect band-gap for the Pd porphyrin Zn-SURMOF 2 is substantially larger than the free base porphyrin Zn-SURMOF 2, which is consistent with the better photovoltaic performance.

Zn(II) porphyrin Zn-SURMOF 2 and DPA- Zn(II) porphyrin Zn-SURMOF 2 were deposited on conductive FTO substrates, which were assembled in an all solid photovoltaic device to avoid the corrosion of liquid electrolyte with an architecture "FTO/(DPA-) Zn(II)porphyrin Zn-SURMOF 2/PEDOT: PSS/Al". The efficiencies are relatively low, 0.006% for Zn(II) porphyrin Zn-SURMOF 2 and 0.017% for DPA- Zn(II) porphyrin Zn-SURMOF 2, respectively. The reason lies in the relatively low photocarrier mobility and recombination of light induced electrons and holes within the Zn(II) porphyrin SURMOF materials. However, the attachment of DPA groups to the porphyrin decreases the band gap and thus enhances the solar conversion efficiency. These findings will be helpful for further systematically increasing the energy conversion efficiency of MOF thin films based photovoltaic devices by designing new MOF thin film materials.

The C_{60}-fullerene loaded free base porphyrin SURMOF was prepared by a novel method during the synthesis by spraying the C_{60} and porphyrin linker in a mixed solution. The UV-Vis spectra

provided direct evidence of the presence of C_{60} in the porphyrin SURMOF material. The XRD data revealed that the C_{60}-loaded porphyrin SURMOFs are highly crystalline as well. But compared to the empty porphyrin SURMOF, the relative intensity of diffraction peak (001) and (002) decreases, which is due to a change of the form factor as a result from the additional big molecules (C_{60} with large number of atoms) in the unit cell. Experimental results also show that the introduction of C_{60} improves the photocurrent properties. The higher concentration of C_{60} loading in the framework, the larger the photocurrent was produced. This study provides a novel method for loading particles within the pores of MOFs and the enhancement of the photocurrent properties after loading with C_{60}-fullerene offers the opportunity to improve the photophysical properties by introduction of the acceptors.

Highly oriented and crystalline porphyrin SURMOFs with azide groups (N_3-porphyrin SURMOF) were prepared on -COOH functionalized gold surfaces. The obtained N_3-porphyrin SURMOF was functionalized using post-synthetic modification based on strain-promoted azido-alkyne cycloaddition (SPAAC), which was monitored using IRRAS and XRD measurements. A copper-free click reaction between N_3-porphyrin and trimethylolethane tripropiolate was carried out within the frameworks and following the removal of the metal ions from the frameworks by the treatment of EDTA, resulting in porphyrin SURGEL. The porphyrin SURGEL, exhibiting pronounced stability against water, offer a chance to be applied as photosensitizer in photodynamic therapy and the introduction of other functional groups into the pores of the gels also enables some potentials applications, for example photosensitive molecules for photo device application.

SURMOF films in combination with QCM technique show great potential for investigating the diffusion of guest molecules in MOFs. In this thesis, the diffusion of ferrocene in MOFs of type HKUST-1 was investigated. It is the first time to compare the diffusion of the guest molecules from gas phase and liquid phase in the same framework. The results show that the diffusion coefficient for ferrocene for the uptake from the gas phase is roughly 3-times smaller than during the uptake from ethanolic and hexanic solutions.

List of Abbreviations

ATR	Attenuated total reflectance
BTC	1,3,5-benzenetricarboxylic acid
CBM	Conduction band maximum
DFT	Density functional theory
DFTB	Density functional based tight-binding
DOS	Density of states
DPA	Dipenylamine
DSSC	Dye sensitized solar cell
FP-TRMC	Flash-photolysis time-resolved microwave conductivity
FC	Ferrocene
FTO	Fluorine doped tin oxide
GGA-DFT	Generalized gradient approximation density functional theory
HOMO	Highest occupied molecular orbital
IRMOFs	Isoreticular MOFs
IRRAS	Infrared reflection absorption spectroscopy
LAG	Liquid-assisted grinding
LB	Langmuir and Blodgett
LPE	Liquid-phase epitaxy
LUMO	Lowest unoccupied molecular orbital
HKUST-1	Hong-Kong University structure 1
MHDA	16-mecaptohexa-decanoic acid
MIL	Matériaux de l'Institut Lavoisier
MOF	Metal-organic framework
MUD	11-mercapto-1-undecanol
PCPs	Porous coordination polymers
PP1	(4-(4-pyridyl)phenyl)-methanethiol
PV	Photovoltaic
QCM	Quartz crystal microbalance

SAM	Self-assembled monolayer
SBUs	Secondary building units
SEM	Scanning electron microscopy
SURMOF	Surface-anchored metal-organic frameworks
SURMOF 2	2 dimensional surface-anchored metal-organic framework
TAS	Transient absorption spectroscopy
TD-DFT	Time-dependent density functional theory
UFF	Universal force field
UIO	University of Oslo
UV-Vis	Ultraviolet-visible
VBM	Valence band maximum
XPS	X-ray photoelectron spectroscopy
XRD	X-ray diffraction
ZIF	Zeolitic imidazolate framework

References

[1] Zhou, H.-C.; Long, J. R.; Yaghi, O. M. Introduction to Metal-Organic Frameworks. *Chem. Rev.* 2012, *112*, 673.

[2] Zhao, M.; Ou, S.; Wu, C.-D. Porous Metal-Organic Frameworks for Heterogeneous Biomimetic Catalysis. *Acc. Chem. Res.* 2014, *47*, 1199.

[3] Lu, W.; Wei, Z.; Gu, Z.-Y.; Liu, T.-F.; Park, J.; Park, J.; Tian, J.; Zhang, M.; Zhang, Q.; Gentle Iii, T.; Bosch, M.; Zhou, H.-C. Tuning the structure and function of metal-organic frameworks via linker design. *Chem. Soc. Rev.* 2014, *43*, 5561.

[4] Kinoshita, Y.; Matsubara, I.; Higuchi, T.; Saito, Y. The Crystal Structure of Bis(adiponitrilo)copper(I) Nitrate. *Bull. Chem. Soc. Jpn.* 1959, *32*, 1221.

[5] Hoskins, B. F.; Robson, R. Design and construction of a new class of scaffolding-like materials comprising infinite polymeric frameworks of 3D-linked molecular rods. A reappraisal of the zinc cyanide and cadmium cyanide structures and the synthesis and structure of the diamond-related frameworks $[N(CH_3)_4][Cu^I Zn^{II}(CN)_4]$ and $Cu^I[4,4',4'',4'''$-tetracyanotetraphenylmethane]$BF_4 \cdot xC_6H_5NO_2$. *J. Am. Chem. Soc.* 1990, *112*, 1546.

[6] Furukawa, H.; Cordova, K. E.; O'Keeffe, M.; Yaghi, O. M. The Chemistry and Applications of Metal-Organic Frameworks. *Science* 2013, *341*.

[7] Dhakshinamoorthy, A.; Garcia, H. Metal-organic frameworks as solid catalysts for the synthesis of nitrogen-containing heterocycles. *Chem. Soc. Rev.* 2014, *43*, 5750.

[8] Rowsell, J. L. C.; Spencer, E. C.; Eckert, J.; Howard, J. A. K.; Yaghi, O. M. Gas Adsorption Sites in a Large-Pore Metal-Organic Framework. *Science* 2005, *309*, 1350.

[9] Bourrelly, S.; Llewellyn, P. L.; Serre, C.; Millange, F.; Loiseau, T.; Férey, G. Different Adsorption Behaviors of Methane and Carbon Dioxide in the Isotypic Nanoporous Metal Terephthalates MIL-53 and MIL-47. *J. Am. Chem. Soc.* 2005, *127*, 13519.

[10] Haque, E.; Lee, J. E.; Jang, I. T.; Hwang, Y. K.; Chang, J.-S.; Jegal, J.; Jhung, S. H. Adsorptive removal of methyl orange from aqueous solution with metal-organic frameworks, porous chromium-benzenedicarboxylates. *J. Hazard. Mater.* 2010, *181*, 535.

[11] Haque, E.; Jun, J. W.; Jhung, S. H. Adsorptive removal of methyl orange and methylene blue from aqueous solution with a metal-organic framework material, iron terephthalate (MOF-235). *J. Hazard. Mater.* 2011, *185*, 507.

[12] Jhung, S. H.; Lee, J. H.; Yoon, J. W.; Serre, C.; Férey, G.; Chang, J. S. Microwave Synthesis of Chromium Terephthalate MIL-101 and Its Benzene Sorption Ability. *Adv. Mater.* 2007, *19*, 121.

[13] Achmann, S.; Hagen, G.; Kita, J.; Malkowsky, I.; Kiener, C.; Moos, R. Metal-Organic Frameworks for Sensing Applications in the Gas Phase. *Sensors* 2009, *9*, 1574.

[14] Bhattacharjee, S.; Yang, D.-A.; Ahn, W.-S. A new heterogeneous catalyst for epoxidation of alkenesvia one-step post-functionalization of IRMOF-3 with a manganese(ii) acetylacetonate complex. *Chem. Commun.* 2011, *47*, 3637.

[15] Kim, J.; Kim, S.-N.; Jang, H.-G.; Seo, G.; Ahn, W.-S. CO_2 cycloaddition of styrene oxide over MOF catalysts. *Appl. Catal., A* 2013, *453*, 175.

[16] Lee, J.; Farha, O. K.; Roberts, J.; Scheidt, K. A.; Nguyen, S. T.; Hupp, J. T. Metal-organic framework materials as catalysts. *Chem. Soc. Rev.* 2009, *38*, 1450.

[17] Huxford, R. C.; Della Rocca, J.; Lin, W. Metal-organic frameworks as potential drug carriers. *Curr. Opin. Chem. Biol.* 2010, *14*, 262.

[18] Tranchemontagne, D. J.; Mendoza-Cortes, J. L.; O'Keeffe, M.; Yaghi, O. M. Secondary building units, nets and bonding in the chemistry of metal-organic frameworks. *Chem. Soc. Rev.* 2009, *38*, 1257.

[19] Kuppler, R. J.; Timmons, D. J.; Fang, Q.-R.; Li, J.-R.; Makal, T. A.; Young, M. D.; Yuan, D.; Zhao, D.; Zhuang, W.; Zhou, H.-C. Potential applications of metal-organic frameworks. *Coord. Chem. Rev.* 2009, *253*, 3042.

[20] Zhao, Z.; Ma, X.; Li, Z.; Lin, Y. S. Synthesis, characterization and gas transport properties of MOF-5 membranes. *J. Membr. Sci.* 2011, *382*, 82.

[21] Chui, S. S.-Y.; Lo, S. M.-F.; Charmant, J. P. H.; Orpen, A. G.; Williams, I. D. A Chemically Functionalizable Nanoporous Material [Cu$_3$(TMA)$_2$(H$_2$O)$_3$]$_n$. *Science* 1999, *283*, 1148.

[22] Zhang, H. F.; Liu, D. F.; Yao, Y.; Zhang, B. Q.; Lin, Y. S. Stability of ZIF-8 membranes and crystalline powders in water at room temperature. *J. Membr. Sci.* 2015, *485*, 103.

[23] Biswas, S.; Couck, S.; Denysenko, D.; Bhunia, A.; Grzywa, M.; Denayer, J. F. M.; Volkmer, D.; Janiak, C.; Van Der Voort, P. Sorption and breathing properties of difluorinated MIL-47 and Al-MIL-53 frameworks. *Microporous Mesoporous Mater.* 2013, *181*, 175.

[24] Piscopo, C. G.; Polyzoidis, A.; Schwarzer, M.; Loebbecke, S. Stability of UiO-66 under acidic treatment: Opportunities and limitations for post-synthetic modifications. *Microporous Mesoporous Mater.* 2015, *208*, 30.

[25] Ortiz, A. U.; Freitas, A. P.; Boutin, A.; Fuchs, A. H.; Coudert, F.-X. What makes zeolitic imidazolate frameworks hydrophobic or hydrophilic? The impact of geometry and functionalization on water adsorption. *Phys. Chem. Chem. Phys.* 2014, *16*, 9940.

[26] Mason, J. A.; Veenstra, M.; Long, J. R. Evaluating metal-organic frameworks for natural gas storage. *Chem. Sci.* 2014, *5*, 32.

[27] Eddaoudi, M.; Kim, J.; Rosi, N.; Vodak, D.; Wachter, J.; O'Keeffe, M.; Yaghi, O. M. Systematic Design of Pore Size and Functionality in Isoreticular MOFs and Their Application in Methane Storage. *Science* 2002, *295*, 469.

[28] Biswas, S.; Ahnfeldt, T.; Stock, N. New Functionalized Flexible Al-MIL-53-X (X = -Cl, -Br, -CH$_3$, -NO$_2$, -(OH)$_2$) Solids: Syntheses, Characterization, Sorption, and Breathing Behavior. *Inorg. Chem.* 2011, *50*, 9518.

[29] Feng, X.; Chen, W.; Xiang, B. Hydrothermal Synthesis, Crystal Structure, and Luminescent Property of a Novel Zn(II)-Organic Framework With Tetranuclear [Zn$_4$(μ_3-OH)$_2$] Clusters Linked by an Unsymmetrical Pyridylbenzoate Ligand With Helical Chains. *Synth. React. Inorg. Met.-Org. Chem.* 2016, *46*, 453.

[30] McKinstry, C.; Cathcart, R. J.; Cussen, E. J.; Fletcher, A. J.; Patwardhan, S. V.; Sefcik, J. Scalable continuous solvothermal synthesis of metal organic framework (MOF-5) crystals. *Chem. Eng. J.* 2016, *285*, 718.

[31] Darago, L. E.; Aubrey, M. L.; Yu, C. J.; Gonzalez, M. I.; Long, J. R. Electronic Conductivity, Ferrimagnetic Ordering, and Reductive Insertion Mediated by Organic Mixed-Valence in a Ferric Semiquinoid Metal-Organic Framework. *J. Am. Chem. Soc.* 2015, *137*, 15703.

[32] Meek, S. T.; Greathouse, J. A.; Allendorf, M. D. Metal-Organic Frameworks: A Rapidly Growing Class of Versatile Nanoporous Materials. *Adv. Mater.* 2011, *23*, 249.

[33] Gedye, R.; Smith, F.; Westaway, K.; Ali, H.; Baldisera, L.; Laberge, L.; Rousell, J. The use of microwave ovens for rapid organic synthesis. *Tetrahedron Lett.* 1986, *27*, 279.

[34] Giguere, R. J.; Bray, T. L.; Duncan, S. M.; Majetich, G. Application of commercial microwave ovens to organic synthesis. *Tetrahedron Lett.* 1986, *27*, 4945.

[35] Kappe, C. O.; Dallinger, D. Controlled microwave heating in modern organic synthesis: highlights from the 2004-2008 literature. *Mol. Diversity* 2009, *13*, 71.

[36] Kappe, C. O. Controlled Microwave Heating in Modern Organic Synthesis. *Angew. Chem. Int. Ed.* 2004, *43*, 6250.

[37] Ni, Z.; Masel, R. I. Rapid Production of Metal-Organic Frameworks via Microwave-Assisted Solvothermal Synthesis. *J. Am. Chem. Soc.* 2006, *128*, 12394.

[38] Pichon, A.; Lazuen-Garay, A.; James, S. L. Solvent-free synthesis of a microporous metal-organic framework. *Crystengcomm* 2006, *8*, 211.

[39] Friscic, T.; Fabian, L. Mechanochemical conversion of a metal oxide into coordination polymers and porous frameworks using liquid-assisted grinding (LAG). *Crystengcomm* 2009, *11*, 743.

[40] Mueller, U.; Puetter, H.; Hesse, M.; Wessel, H. WO 2005/049892, 2005. *BASF Aktiengesellschaft* 2007.

[41] Martinez Joaristi, A.; Juan-Alcañiz, J.; Serra-Crespo, P.; Kapteijn, F.; Gascon, J. Electrochemical Synthesis of Some Archetypical Zn^{2+}, Cu^{2+}, and Al^{3+} Metal Organic Frameworks. *Cryst. Growth Des.* 2012, *12*, 3489.

[42] Stassen, I.; Styles, M.; Van Assche, T.; Campagnol, N.; Fransaer, J.; Denayer, J.; Tan, J.-C.; Falcaro, P.; De Vos, D.; Ameloot, R. Electrochemical Film Deposition of the Zirconium Metal–Organic Framework UiO-66 and Application in a Miniaturized Sorbent Trap. *Chem. Mater.* 2015, *27*, 1801.

[43] Al-Kutubi, H.; Gascon, J.; Sudhölter, E. J. R.; Rassaei, L. Electrosynthesis of Metal–Organic Frameworks: Challenges and Opportunities. *ChemElectroChem* 2015, *2*, 462.

[44] Ameloot, R.; Stappers, L.; Fransaer, J.; Alaerts, L.; Sels, B. F.; De Vos, D. E. Patterned Growth of Metal-Organic Framework Coatings by Electrochemical Synthesis. *Chem. Mater.* 2009, *21*, 2580.

[45] Hartmann, M.; Kunz, S.; Himsl, D.; Tangermann, O.; Ernst, S.; Wagener, A. Adsorptive Separation of Isobutene and Isobutane on $Cu_3(BTC)_2$. *Langmuir* 2008, *24*, 8634.

[46] Senthil Kumar, R.; Senthil Kumar, S.; Anbu Kulandainathan, M. Efficient electrosynthesis of highly active $Cu_3(BTC)_2$-MOF and its catalytic application to chemical reduction. *Microporous Mesoporous Mater.* 2013, *168*, 57.

[47] Van Assche, T. R. C.; Desmet, G.; Ameloot, R.; De Vos, D. E.; Terryn, H.; Denayer, J. F. M. Electrochemical synthesis of thin HKUST-1 layers on copper mesh. *Microporous Mesoporous Mater.* 2012, *158*, 209.

[48] Campagnol, N.; Van Assche, T.; Boudewijns, T.; Denayer, J.; Binnemans, K.; De Vos, D.; Fransaer, J. High pressure, high temperature electrochemical synthesis of metal-organic frameworks: films of MIL-100 (Fe) and HKUST-1 in different morphologies. *J. Mater. Chem. A* 2013, *1*, 5827.

[49] Carson, C. G.; Brown, A. J.; Sholl, D. S.; Nair, S. Sonochemical Synthesis and Characterization of Submicrometer Crystals of the Metal-Organic Framework $Cu[(hfipbb)(H_2hfipbb)_{0.5}]$. *Cryst. Growth Des.* 2011, *11*, 4505.

[50] Goto, Y.; Sato, H.; Shinkai, S.; Sada, K. "Clickable" Metal-Organic Framework. *J. Am. Chem. Soc.* 2008, *130*, 14354.

[51] Shekhah, O.; Wang, H.; Paradinas, M.; Ocal, C.; Schupbach, B.; Terfort, A.; Zacher, D.; Fischer, R. A.; Wöll, C. Controlling interpenetration in metal-organic frameworks by liquid-phase epitaxy. *Nat. Mater.* 2009, *8*, 481.

[52] Fischer, R. A.; Wöll, C. Layer-by-Layer Liquid-Phase Epitaxy of Crystalline Coordination Polymers at Surfaces. *Angew. Chem. Int. Ed.* 2009, *48*, 6205.

[53] Rosi, N. L.; Eckert, J.; Eddaoudi, M.; Vodak, D. T.; Kim, J.; O'Keeffe, M.; Yaghi, O. M. Hydrogen Storage in Microporous Metal-Organic Frameworks. *Science* 2003, *300*, 1127.

[54] Latroche, M.; Surblé, S.; Serre, C.; Mellot-Draznieks, C.; Llewellyn, P. L.; Lee, J.-H.; Chang, J.-S.; Jhung, S. H.; Férey, G. Hydrogen Storage in the Giant-Pore Metal-Organic Frameworks MIL-100 and MIL-101. *Angew. Chem. Int. Ed.* 2006, *45*, 8227.

[55] Park, K. S.; Ni, Z.; Côté, A. P.; Choi, J. Y.; Huang, R.; Uribe-Romo, F. J.; Chae, H. K.; O'Keeffe, M.; Yaghi, O. M. Exceptional chemical and thermal stability of zeolitic imidazolate frameworks. *Proc. Natl. Acad. Sci.* 2006, *103*, 10186.

[56] Klein, N.; Senkovska, I.; Gedrich, K.; Stoeck, U.; Henschel, A.; Mueller, U.; Kaskel, S. A Mesoporous Metal-Organic Framework. *Angew. Chem. Int. Ed.* 2009, *48*, 9954.

[57] Lin, X.; Telepeni, I.; Blake, A. J.; Dailly, A.; Brown, C. M.; Simmons, J. M.; Zoppi, M.; Walker, G. S.; Thomas, K. M.; Mays, T. J.; Hubberstey, P.; Champness, N. R.; Schröder, M. High Capacity Hydrogen Adsorption in Cu(II) Tetracarboxylate Framework Materials: The Role of Pore Size, Ligand Functionalization, and Exposed Metal Sites. *J. Am. Chem. Soc.* 2009, *131*, 2159.

[58] Ma, S.; Eckert, J.; Forster, P. M.; Yoon, J. W.; Hwang, Y. K.; Chang, J.-S.; Collier, C. D.; Parise, J. B.; Zhou, H.-C. Further Investigation of the Effect of Framework Catenation on Hydrogen Uptake in Metal-Organic Frameworks. *J. Am. Chem. Soc.* 2008, *130*, 15896.

[59] Lee, Y.-G.; Moon, H. R.; Cheon, Y. E.; Suh, M. P. A Comparison of the H_2 Sorption Capacities of Isostructural Metal-Organic Frameworks With and Without Accessible Metal Sites:

[{Zn$_2$(abtc)(dmf)$_2$}$_3$] and [{Cu$_2$(abtc)(dmf)$_2$}$_3$] versus [{Cu$_2$(abtc)}$_3$]. *Angew. Chem. Int. Ed.* 2008, *47*, 7741.

[60] Chen, B.; Zhao, X.; Putkham, A.; Hong, K.; Lobkovsky, E. B.; Hurtado, E. J.; Fletcher, A. J.; Thomas, K. M. Surface Interactions and Quantum Kinetic Molecular Sieving for H$_2$ and D$_2$ Adsorption on a Mixed Metal-Organic Framework Material. *J. Am. Chem. Soc.* 2008, *130*, 6411.

[61] Farha, O. K.; Özgür Yazaydın, A.; Eryazici, I.; Malliakas, C. D.; Hauser, B. G.; Kanatzidis, M. G.; Nguyen, S. T.; Snurr, R. Q.; Hupp, J. T. De novo synthesis of a metal-organic framework material featuring ultrahigh surface area and gas storage capacities. *Nat Chem* 2010, *2*, 944.

[62] Kondo, M.; Yoshitomi, T.; Matsuzaka, H.; Kitagawa, S.; Seki, K. Three-Dimensional Framework with Channeling Cavities for Small Molecules: {[M$_2$(4, 4$'$-bpy)$_3$(NO$_3$)$_4$] • xH$_2$O}n (M=Co, Ni, Zn). *Angew. Chem. Int. Ed. Engl.* 1997, *36*, 1725.

[63] Furukawa, H.; Ko, N.; Go, Y. B.; Aratani, N.; Choi, S. B.; Choi, E.; Yazaydin, A. Ö.; Snurr, R. Q.; O'Keeffe, M.; Kim, J.; Yaghi, O. M. Ultrahigh Porosity in Metal-Organic Frameworks. *Science* 2010, *329*, 424.

[64] Llewellyn, P. L.; Bourrelly, S.; Serre, C.; Vimont, A.; Daturi, M.; Hamon, L.; De Weireld, G.; Chang, J.-S.; Hong, D.-Y.; Kyu Hwang, Y.; Hwa Jhung, S.; Férey, G. High Uptakes of CO$_2$ and CH$_4$ in Mesoporous Metal-Organic Frameworks MIL-100 and MIL-101. *Langmuir* 2008, *24*, 7245.

[65] Gascon, J.; Corma, A.; Kapteijn, F.; Llabrés i Xamena, F. X. Metal Organic Framework Catalysis: Quo vadis? *ACS Catal.* 2014, *4*, 361.

[66] Silva, P.; Vilela, S. M. F.; Tome, J. P. C.; Almeida Paz, F. A. Multifunctional metal-organic frameworks: from academia to industrial applications. *Chem. Soc. Rev.* 2015, *44*, 6774.

[67] Fei, H.; Shin, J.; Meng, Y. S.; Adelhardt, M.; Sutter, J.; Meyer, K.; Cohen, S. M. Reusable Oxidation Catalysis Using Metal-Monocatecholato Species in a Robust Metal-Organic Framework. *J. Am. Chem. Soc.* 2014, *136*, 4965.

[68] Lei, J.; Qian, R.; Ling, P.; Cui, L.; Ju, H. Design and sensing applications of metal-organic framework composites. *TrAC, Trends Anal. Chem.* 2014, *58*, 71.

[69] Ma, W.; Jiang, Q.; Yu, P.; Yang, L.; Mao, L. Zeolitic Imidazolate Framework-Based Electrochemical Biosensor for in Vivo Electrochemical Measurements. *Anal. Chem.* 2013, *85*, 7550.

[70] Horcajada, P.; Serre, C.; Vallet-Regí, M.; Sebban, M.; Taulelle, F.; Férey, G. Metal–Organic Frameworks as Efficient Materials for Drug Delivery. *Angew. Chem.* 2006, *118*, 6120.

[71] Bae, T.-H.; Lee, J. S.; Qiu, W.; Koros, W. J.; Jones, C. W.; Nair, S. A High-Performance Gas-Separation Membrane Containing Submicrometer-Sized Metal-Organic Framework Crystals. *Angew. Chem. Int. Ed.* 2010, *49*, 9863.

[72] Talin, A. A.; Centrone, A.; Ford, A. C.; Foster, M. E.; Stavila, V.; Haney, P.; Kinney, R. A.; Szalai, V.; El Gabaly, F.; Yoon, H. P.; Léonard, F.; Allendorf, M. D. Tunable Electrical Conductivity in Metal-Organic Framework Thin-Film Devices. *Science* 2014, *343*, 66.

[73] Kreno, L. E.; Hupp, J. T.; Van Duyne, R. P. Metal-Organic Framework Thin Film for Enhanced Localized Surface Plasmon Resonance Gas Sensing. *Anal. Chem.* 2010, *82*, 8042.

[74] Bétard, A.; Fischer, R. A. Metal-Organic Framework Thin Films: From Fundamentals to Applications. *Chem. Rev.* 2012, *112*, 1055.

[75] Wade, C. R.; Li, M.; Dincă, M. Facile Deposition of Multicolored Electrochromic Metal–Organic Framework Thin Films. *Angew. Chem.* 2013, *125*, 13619.

[76] Hermes, S.; Schröder, F.; Chelmowski, R.; Wöll, C.; Fischer, R. A. Selective Nucleation and Growth of Metal-Organic Open Framework Thin Films on Patterned COOH/CF$_3$-Terminated Self-Assembled Monolayers on Au(111). *J. Am. Chem. Soc.* 2005, *127*, 13744.

[77] Gascon, J.; Aguado, S.; Kapteijn, F. Manufacture of dense coatings of Cu$_3$(BTC)$_2$ (HKUST-1) on α-alumina. *Microporous Mesoporous Mater.* 2008, *113*, 132.

[78] Guerrero, V. V.; Yoo, Y.; McCarthy, M. C.; Jeong, H.-K. HKUST-1 membranes on porous supports using secondary growth. *J. Mater. Chem.* 2010, *20*, 3938.

[79] Mueller, U.; Schubert, M.; Teich, F.; Puetter, H.; Schierle-Arndt, K.; Pastre, J. Metal-organic frameworks-prospective industrial applications. *J. Mater. Chem.* 2006, *16*, 626.

[80] Makiura, R.; Motoyama, S.; Umemura, Y.; Yamanaka, H.; Sakata, O.; Kitagawa, H. Surface nano-architecture of a metal-organic framework. *Nat. Mater.* 2010, *9*, 565.

[81] Shekhah, O.; Wang, H.; Kowarik, S.; Schreiber, F.; Paulus, M.; Tolan, M.; Sternemann, C.; Evers, F.; Zacher, D.; Fischer, R. A.; Wöll, C. Step-by-Step Route for the Synthesis of Metal-Organic Frameworks. *J. Am. Chem. Soc.* 2007, *129*, 15118.

[82] Shekhah, O.; Wang, H.; Strunskus, T.; Cyganik, P.; Zacher, D.; Fischer, R.; Wöll, C. Layer-by-Layer Growth of Oriented Metal Organic Polymers on a Functionalized Organic Surface. *Langmuir* 2007, *23*, 7440.

[83] Love, J. C.; Estroff, L. A.; Kriebel, J. K.; Nuzzo, R. G.; Whitesides, G. M. Self-Assembled Monolayers of Thiolates on Metals as a Form of Nanotechnology. *Chem. Rev.* 2005, *105*, 1103.

[84] Bradshaw, D.; Garai, A.; Huo, J. Metal-organic framework growth at functional interfaces: thin films and composites for diverse applications. *Chem. Soc. Rev.* 2012, *41*, 2344.

[85] Arnold, R.; Azzam, W.; Terfort, A.; Wöll, C. Preparation, Modification, and Crystallinity of Aliphatic and Aromatic Carboxylic Acid Terminated Self-Assembled Monolayers. *Langmuir* 2002, *18*, 3980.

[86] Liu, J.; Schupbach, B.; Bashir, A.; Shekhah, O.; Nefedov, A.; Kind, M.; Terfort, A.; Wöll, C. Structural characterization of self-assembled monolayers of pyridine-terminated thiolates on gold. *Phys. Chem. Chem. Phys.* 2010, *12*, 4459.

[87] Heinke, L.; Tu, M.; Wannapaiboon, S.; Fischer, R. A.; Wöll, C. Surface-mounted metal-organic frameworks for applications in sensing and separation. *Microporous Mesoporous Mater.* 2015, *216*, 200.

[88] Velamakanni, A.; Torres, J. R.; Ganesh, K. J.; Ferreira, P. J.; Major, J. S. Controlled Assembly of Silane-Based Polymers: Chemically Robust Thin-Films. *Langmuir* 2010, *26*, 15295.

[89] Decher, G. Fuzzy Nanoassemblies: Toward Layered Polymeric Multicomposites. *Science* 1997, *277*, 1232.

[90] Bell, C. M.; Arendt, M. F.; Gomez, L.; Schmehl, R. H.; Mallouk, T. E. Growth of lamellar Hofmann clathrate films by sequential ligand exchange reactions: assembling a coordination solid one layer at a time. *J. Am. Chem. Soc.* 1994, *116*, 8374.

[91] Arslan, H. K.; Shekhah, O.; Wohlgemuth, J.; Franzreb, M.; Fischer, R. A.; Wöll, C. High-Throughput Fabrication of Uniform and Homogenous MOF Coatings. *Adv. Funct. Mater.* 2011, *21*, 4228.

[92] Munuera, C.; Shekhah, O.; Wang, H.; Wöll, C.; Ocal, C. The controlled growth of oriented metal-organic frameworks on functionalized surfaces as followed by scanning force microscopy. *Phys. Chem. Chem. Phys.* 2008, *10*, 7257.

[93] Gu, Z.-G.; Pfriem, A.; Hamsch, S.; Breitwieser, H.; Wohlgemuth, J.; Heinke, L.; Gliemann, H.; Wöll, C. Transparent films of metal-organic frameworks for optical applications. *Microporous Mesoporous Mater.* 2015, *211*, 82.

[94] Arslan, H. K.; Shekhah, O.; Wieland, D. C. F.; Paulus, M.; Sternemann, C.; Schroer, M. A.; Tiemeyer, S.; Tolan, M.; Fischer, R. A.; Wöll, C. Intercalation in Layered Meta-Organic Frameworks: Reversible Inclusion of an Extended π-System. *J. Am. Chem. Soc.* 2011, *133*, 8158.

[95] Shekhah, O.; Wang, H.; Zacher, D.; Fischer, R. A.; Wöll, C. Growth Mechanism of Metal-Organic Frameworks: Insights into the Nucleation by Employing a Step-by-Step Route. *Angew. Chem. Int. Ed.* 2009, *48*, 5038.

[96] Silvestre, M. E.; Franzreb, M.; Weidler, P. G.; Shekhah, O.; Wöll, C. Magnetic Cores with Porous Coatings: Growth of Metal-Organic Frameworks on Particles Using Liquid Phase Epitaxy. *Adv. Funct. Mater.* 2013, *23*, 1210.

[97] Venkatasubramanian, A.; Navaei, M.; Bagnall, K. R.; McCarley, K. C.; Nair, S.; Hesketh, P. J. Gas Adsorption Characteristics of Metal-Organic Frameworks via Quartz Crystal Microbalance Techniques. *J. Phys. Chem. C* 2012, *116*, 15313.

[98] Stavila, V.; Volponi, J.; Katzenmeyer, A. M.; Dixon, M. C.; Allendorf, M. D. Kinetics and mechanism of metal-organic framework thin film growth: systematic investigation of HKUST-1 deposition on QCM electrodes. *Chem. Sci.* 2012, *3*, 1531.

[99] St. Petkov, P.; Vayssilov, G. N.; Liu, J.; Shekhah, O.; Wang, Y.; Wöll, C.; Heine, T. Defects in MOFs: A Thorough Characterization. *Chemphyschem* 2012, *13*, 2025.

[100] Zhou, W.; Wöll, C.; Heinke, L. Liquid- and Gas-Phase Diffusion of Ferrocene in Thin Films of Metal-Organic Frameworks. *Materials* 2015, *8*, 3767.

[101] Zybaylo, O.; Shekhah, O.; Wang, H.; Tafipolsky, M.; Schmid, R.; Johannsmann, D.; Wöll, C. A novel method to measure diffusion coefficients in porous metal-organic frameworks. *Phys. Chem. Chem. Phys.* 2010, *12*, 8093.

[102] Wang, Z.; Cohen, S. M. Postsynthetic modification of metal-organic frameworks. *Chem. Soc. Rev.* 2009, *38*, 1315.

[103] Wang, Z.; Liu, J.; Arslan, H. K.; Grosjean, S.; Hagendorn, T.; Gliemann, H.; Bräse, S.; Wöll, C. Post-Synthetic Modification of Metal-Organic Framework Thin Films Using Click Chemistry: The Importance of Strained C-C Triple Bonds. *Langmuir* 2013, *29*, 15958.

[104] Tsotsalas, M.; Liu, J.; Tettmann, B.; Grosjean, S.; Shahnas, A.; Wang, Z.; Azucena, C.; Addicoat, M.; Heine, T.; Lahann, J.; Overhage, J.; Bräse, S.; Gliemann, H.; Wöll, C. Fabrication of highly uniform gel coatings by the conversion of surface-anchored metal-organic frameworks. *J. Am. Chem. Soc.* 2014, *136*, 8.

[105] Schmitt, S.; Silvestre, M.; Tsotsalas, M.; Winkler, A.-L.; Shahnas, A.; Grosjean, S.; Laye, F.; Gliemann, H.; Lahann, J.; Bräse, S.; Franzreb, M.; Wöll, C. Hierarchically functionalized magnetic core/multishell particles and their postsynthetic conversion to polymer capsules. *Acs Nano* 2015, *9*, 4219.

[106] Mugnaini, V.; Tsotsalas, M.; Bebensee, F.; Grosjean, S.; Shahnas, A.; Brase, S.; Lahann, J.; Buck, M.; Wöll, C. Electrochemical investigation of covalently post-synthetic modified SURGEL coatings. *Chem. Commun.* 2014, *50*, 11129.

[107] Biesaga, M.; Pyrzyńska, K.; Trojanowicz, M. Porphyrins in analytical chemistry. A review. *Talanta* 2000, *51*, 209.

[108] Milgrom, L. R. The colours of life : an introduction to the chemistry of porphyrins and related compounds; Oxford University Press: Oxford [etc.], 1997.

[109] Anson, M. L.; Mirsky, A. E. Hemoglobin, the heme pigments, and cellular respiration. *Physiol. Rev.* 1930, *10*, 506.

[110] Willstätter, R.; Benz, M. Zur Kenntniss der Azophenole. *Ber. Dtsch. Chem. Ges.* 1906, *39*, 3492.

[111] SMITH, K. M. Syntheses and chemistry of porphyrins. *J. Porphyrins Phthalocyanines* 2000, *04*, 319.

[112] Arsenault, G. P.; Bullock, E.; MacDonald, S. F. Pyrromethanes and Porphyrins Therefrom1. *J. Am. Chem. Soc.* 1960, *82*, 4384.

[113] Lash, T. D. Porphyrin synthesis by the "3+1" approach: new applications for an old methodology. *Chem. Eur. J.* 1996, *2*, 1197.

[114] Vicente, M. G. H.; Smith, K. M. Porphyrins and Derivatives Synthetic Strategies and Reactivity Profiles. *Curr. Org. Chem.* 2000, *4*, 139.

[115] Rebelo, S. L. H.; Linhares, M.; Simões, M. M. Q.; Silva, A. M. S.; Neves, M. G. P. M. S.; Cavaleiro, J. A. S.; Freire, C. Indigo dye production by enzymatic mimicking based on an iron(III)porphyrin. *J. Catal.* 2014, *315*, 33.

[116] Xie, Y.; Hill, J. P.; Charvet, R.; Ariga, K. Porphyrin Colorimetric Indicators in Molecular and Nano-Architectures. *J. Nanosci. Nanotechnol.* 2007, *7*, 2969.

[117] Di Natale, C.; Monti, D.; Paolesse, R. Chemical sensitivity of porphyrin assemblies. *Mater. Today* 2010, *13*, 46.

[118] Ethirajan, M.; Chen, Y.; Joshi, P.; Pandey, R. K. The role of porphyrin chemistry in tumor imaging and photodynamic therapy. *Chem. Soc. Rev.* 2011, *40*, 340.

[119] O'Connor, A. E.; Gallagher, W. M.; Byrne, A. T. Porphyrin and Nonporphyrin Photosensitizers in Oncology: Preclinical and Clinical Advances in Photodynamic Therapy. *Photochem. Photobiol.* 2009, *85*, 1053.

[120] Kim, D.; Osuka, A. Photophysical Properties of Directly Linked Linear Porphyrin Arrays. *J. Phys. Chem. A* 2003, *107*, 8791.

[121] Hsieh, C.-P.; Lu, H.-P.; Chiu, C.-L.; Lee, C.-W.; Chuang, S.-H.; Mai, C.-L.; Yen, W.-N.; Hsu, S.-J.; Diau, E. W.-G.; Yeh, C.-Y. Synthesis and characterization of porphyrin sensitizers with various electron-donating substituents for highly efficient dye-sensitized solar cells. *J. Mater. Chem.* 2010, *20*, 1127.

[122] Mathew, S.; Yella, A.; Gao, P.; Humphry-Baker, R.; CurchodBasile, F. E.; Ashari-Astani, N.; Tavernelli, I.; Rothlisberger, U.; NazeeruddinMd, K.; Grätzel, M. Dye-sensitized solar cells with 13% efficiency achieved through the molecular engineering of porphyrin sensitizers. *Nat Chem* 2014, *6*, 242.

[123] Tillekaratne, A. D.; de Silva, R. M.; Nalin de Silva, K. M. Push-pull porphyrins as non-linear optical materials: ab initio quantum chemical calculations. *J. Mol. Struc.-THEOCHEM* 2003, *638*, 169.

[124] Guo, C.-C.; Ren, T.-G.; Song, J.-X.; Liu, Q.; Luo, K.; Lin, W.-Y.; Jiang, G.-F. Substituted tetrapyrazolylporphyrins: application in organic light-emitting diodes. *J. Porphyrins Phthalocyanines* 2005, *09*, 830.

[125] Liang, X.; Li, X.; Jing, L.; Yue, X.; Dai, Z. Theranostic porphyrin dyad nanoparticles for magnetic resonance imaging guided photodynamic therapy. *Biomaterials* 2014, *35*, 6379.

[126] Gao, W.-Y.; Chrzanowski, M.; Ma, S. Metal-metalloporphyrin frameworks: a resurging class of functional materials. *Chem. Soc. Rev.* 2014, *43*, 5841.

[127] Abrahams, B. F.; Hoskins, B. F.; Robson, R. A new type of infinite 3D polymeric network containing 4-connected, peripherally-linked metalloporphyrin building blocks. *J. Am. Chem. Soc.* 1991, *113*, 3606.

[128] Ohmura, T.; Usuki, A.; Fukumori, K.; Ohta, T.; Ito, M.; Tatsumi, K. New porphyrin-based metal-organic framework with high porosity: 2D infinite 22.2Å square-grid coordination network. *Inorg. Chem.* 2006, *45*, 7988.

[129] Shultz, A. M.; Farha, O. K.; Hupp, J. T.; Nguyen, S. T. A Catalytically Active, Permanently Microporous MOF with Metalloporphyrin Struts. *J. Am. Chem. Soc.* 2009, *131*, 4204.

[130] Lee, C. Y.; Farha, O. K.; Hong, B. J.; Sarjeant, A. A.; Nguyen, S. T.; Hupp, J. T. Light-Harvesting Metal-Organic Frameworks (MOFs): Efficient Strut-to-Strut Energy Transfer in Bodipy and Porphyrin-Based MOFs. *J. Am. Chem. Soc.* 2011, *133*, 15858.

[131] Motoyama, S.; Makiura, R.; Sakata, O.; Kitagawa, H. Highly Crystalline Nanofilm by Layering of Porphyrin Metal-Organic Framework Sheets. *J. Am. Chem. Soc.* 2011, *133*, 5640.

[132] Feng, D.; Gu, Z.-Y.; Li, J.-R.; Jiang, H.-L.; Wei, Z.; Zhou, H.-C. Zirconium-Metalloporphyrin PCN-222: Mesoporous Metal-Organic Frameworks with Ultrahigh Stability as Biomimetic Catalysts. *Angew. Chem.* 2012, *124*, 10453.

[133] So, M. C.; Jin, S.; Son, H.-J.; Wiederrecht, G. P.; Farha, O. K.; Hupp, J. T. Layer-by-Layer Fabrication of Oriented Porous Thin Films Based on Porphyrin-Containing Metal-Organic Frameworks. *J. Am. Chem. Soc.* 2013, *135*, 15698.

[134] D'Souza, F.; Chitta, R.; Gadde, S.; Zandler, M. E.; McCarty, A. L.; Sandanayaka, A. S. D.; Araki, Y.; Ito, O. Potassium Ion Controlled Switching of Intra- to Intermolecular Electron Transfer in Crown Ether Appended Free-Base Porphyrin-Fullerene Donor-Acceptor Systems. *J. Phys. Chem. A* 2006, *110*, 4338.

[135] http://media.rsc.org/Modern%20chemical%20techniques/MCT4%20UV%20and%20visible%20spec.pdf. *Taken on 04/05/2016.*

[136] http://www.kinetics.nsc.ru/chichinin/books/spectroscopy/Stuart04.pdf. *Taken on 04/05/2016.*

[137] Mojet, B. L.; Ebbesen, S. D.; Lefferts, L. Light at the interface: the potential of attenuated total reflection infrared spectroscopy for understanding heterogeneous catalysis in water. *Chem. Soc. Rev.* 2010, *39*, 4643.

[138] Greenler, R. G. Infrared Study of Adsorbed Molecules on Metal Surfaces by Reflection Techniques. *J. Chem. Phys.* 1966, *44*, 310.

[139] Francis, S. A.; Ellison, A. H. Infrared Spectra of Monolayers on Metal Mirrors. *J. Opt. Soc. Am.* 1959, *49*, 131.

[140] Hoffmann, F. M. Infrared reflection-absorption spectroscopy of adsorbed molecules. *Surf. Sci. Rep.* 1983, *3*, 107.

[141] Goldstein, J.; Newbury, D. E.; Echlin, P.; Joy, D. C.; Romig, A. D.; Lyman, C. E.; Fiori, C.; Lifshin, E. *Scanning Electron Microscopy and X-Ray Microanalysis: A Text for Biologists, Materials Scientists, and Geologists*; Springer US, 2012.

[142] Zhou, W.; Apkarian, R.; Wang, Z. L.; Joy, D. In *Scanning Microscopy for Nanotechnology: Techniques and Applications*; Zhou, W., Wang, Z. L., Eds.; Springer New York: New York, NY, 2007, p 1.

[143] https://en.wikipedia.org/wiki/Scanning_electron_microscope. *Taken on 04/05/2016.*

[144] Swartz, W. E. X-ray photoelectron spectroscopy. *Anal. Chem.* 1973, *45*, 788A.

[145] Watts, J. F. X-ray photoelectron spectroscopy. *Vacuum* 1994, *45*, 653.

[146]http://images.google.de/imgres?imgurl=http%3A%2F%2Fwww.texample.net%2Fmedia%2Ftikz%2Fexamples%2FPNG%2Fprinciple-of-x-ray-photoelectron-spectroscopy-xps.png&imgrefurl=http%3A%2F%2Fwww.texample.net%2Ftikz%2Fexamples%2Fprinciple-of-x-ray-photoelectron-spectroscopy-xps%2F&h=500&w=481&tbnid=XGEwMSUiXtcWpM%3A&docid=mFoZPNmUOp1jbM&ei=1x4jV8HvCMWHU5jPhtgK&tbm=isch&iact=rc&uact=3&dur=675&page=1&start=0&ndsp=20&ved=0ahUKEwiBt9mqurPMAhXFwxQKHZinAasQMwgjKAIwAg&bih=899&biw=1280. *Taken on 04/05/2016.*

[147] Marx, K. A. Quartz Crystal Microbalance: A Useful Tool for Studying Thin Polymer Films and Complex Biomolecular Systems at the Solution-Surface Interface. *Biomacromolecules* 2003, *4*, 1099.

[148] O'Sullivan, C. K.; Guilbault, G. G. Commercial quartz crystal microbalances- theory and applications. *Biosens. Bioelectron.* 1999, *14*, 663.

[149] Rodahl, M.; Höök, F.; Krozer, A.; Brzezinski, P.; Kasemo, B. Quartz crystal microbalance setup for frequency and Q‐factor measurements in gaseous and liquid environments. *Rev. Sci. Instrum.* 1995, *66*, 3924.

[150] Sauerbrey, G. Use of vibrating quartz for thin film weighing and microweighing. *Z. Phys* 1959, *155*, 206.

[151] Reviakine, I.; Johannsmann, D.; Richter, R. P. Hearing What You Cannot See and Visualizing What You Hear: Interpreting Quartz Crystal Microbalance Data from Solvated Interfaces. *Anal. Chem.* 2011, *83*, 8838.

[152] Beck, R.; Pittermann, U.; Weil, K. G. Impedance Analysis of Quartz Oscillators, Contacted on One Side with a Liquid. *Berichte der Bunsengesellschaft für physikalische Chemie* 1988, *92*, 1363.

[153] Johannsmann, D. Viscoelastic, mechanical, and dielectric measurements on complex samples with the quartz crystal microbalance. *Phys. Chem. Chem. Phys.* 2008, *10*, 4516.

[154] Marrazza, G. Piezoelectric Biosensors for Organophosphate and Carbamate Pesticides: A Review. *Biosensors* 2014, *4*, 301.

[155] Lichtman, J. W.; Conchello, J.-A. Fluorescence microscopy. *Nat Meth* 2005, *2*, 910.

[156] Heine, J.; Muller-Buschbaum, K. Engineering metal-based luminescence in coordination polymers and metal-organic frameworks. *Chem. Soc. Rev.* 2013, *42*, 9232.

[157] Chen, Y.; Periasamy, A. Characterization of two-photon excitation fluorescence lifetime imaging microscopy for protein localization. *Microsc. Res. Tech.* 2004, *63*, 72.

[158] Berezin, M. Y.; Achilefu, S. Fluorescence Lifetime Measurements and Biological Imaging. *Chem. Rev.* 2010, *110*, 2641.

[159] Bastiaens, P. I. H.; Squire, A. Fluorescence lifetime imaging microscopy: spatial resolution of biochemical processes in the cell. *Trends Cell. Biol.* 1999, *9*, 48.

[160] Lakowicz, J. R.; Maliwal, B. P. Construction and performance of a variable-frequency phase-modulation fluorometer. *Biophys. Chem.* 1985, *21*, 61.

[161] Gratton, E.; Limkeman, M. A continuously variable frequency cross-correlation phase fluorometer with picosecond resolution. *Biophys. J.* 1983, *44*, 315.

[162] Berera, R.; Grondelle, R.; Kennis, J. T. M. Ultrafast transient absorption spectroscopy: principles and application to photosynthetic systems. *Photosynth. Res.* 2009, *101*, 105.

[163] Lorenc, M.; Ziolek, M.; Naskrecki, R.; Karolczak, J.; Kubicki, J.; Maciejewski, A. Artifacts in femtosecond transient absorption spectroscopy. *Appl. Phys. B 74*, 19.

[164] Kroeze, J. E.; Savenije, T. J.; Warman, J. M. Electrodeless Determination of the Trap Density, Decay Kinetics, and Charge Separation Efficiency of Dye-Sensitized Nanocrystalline TiO2. *J. Am. Chem. Soc.* 2004, *126*, 7608.

[165] Dayal, S.; Kopidakis, N.; Rumbles, G. Photoinduced electron transfer in composites of conjugated polymers and dendrimers with branched colloidal nanoparticles. *Faraday Discuss.* 2012, *155*, 323.

[166] Saeki, A.; Seki, S.; Sunagawa, T.; Ushida, K.; Tagawa, S. Charge-carrier dynamics in polythiophene films studied by in-situ measurement of flash-photolysis time-resolved microwave conductivity (FP-TRMC) and transient optical spectroscopy (TOS). *Philos. Mag.* 2006, *86*, 1261.

[167] Son, H.-J.; Jin, S.; Patwardhan, S.; Wezenberg, S. J.; Jeong, N. C.; So, M.; Wilmer, C. E.; Sarjeant, A. A.; Schatz, G. C.; Snurr, R. Q.; Farha, O. K.; Wiederrecht, G. P.; Hupp, J. T. Light-Harvesting and Ultrafast Energy Migration in Porphyrin-Based Metal-Organic Frameworks. *J. Am. Chem. Soc.* 2013, *135*, 862.

[168] Deacon, G. B.; Phillips, R. J. Relationships between the carbon-oxygen stretching frequencies of carboxylato complexes and the type of carboxylate coordination. *Coord. Chem. Rev.* 1980, *33*, 227.

[169] Costas, M.; Cady, C. W.; Kryatov, S. V.; Ray, M.; Ryan, M. J.; Rybak-Akimova, E. V.; Que, L. Role of Carboxylate Bridges in Modulating Nonheme Diiron(II)/O_2 Reactivity. *Inorg. Chem.* 2003, *42*, 7519.

[170] de Miguel, G.; Hosomizu, K.; Umeyama, T.; Matano, Y.; Imahori, H.; Mart ń-Romero, M. T.; Camacho, L. Tunable Soret-Band Splitting of an Amphiphilic Porphyrin by Surface Pressure. *Chemphyschem* 2008, *9*, 1511.

[171] Matsunaga, S.; Endo, N.; Mori, W. A New Metal Carboxylate Framework Based on Porphyrin with Extended π-Conjugation. *Eur. J. Inorg. Chem.* 2011, *2011*, 4550.

[172] Karweik, D. H.; Winograd, N. Nitrogen charge distributions in free-base porphyrins, metalloporphyrins, and their reduced analogs observed by x-ray photoelectron spectroscopy. *Inorg. Chem.* 1976, *15*, 2336.

[173] Narayan, T. C.; Miyakai, T.; Seki, S.; Dincă, M. High Charge Mobility in a Tetrathiafulvalene-Based Microporous Metal-Organic Framework. *J. Am. Chem. Soc.* 2012, *134*, 12932.

[174] Feng, X.; Liu, L.; Honsho, Y.; Saeki, A.; Seki, S.; Irle, S.; Dong, Y.; Nagai, A.; Jiang, D. High-Rate Charge-Carrier Transport in Porphyrin Covalent Organic Frameworks: Switching from Hole to Electron to Ambipolar Conduction. *Angew. Chem. Int. Ed.* 2012, *51*, 2618.

[175] Kira, A.; Umeyama, T.; Matano, Y.; Yoshida, K.; Isoda, S.; Park, J. K.; Kim, D.; Imahori, H. Supramolecular Donor-Acceptor Heterojunctions by Vectorial Stepwise Assembly of Porphyrins and Coordination-Bonded Fullerene Arrays for Photocurrent Generation. *J. Am. Chem. Soc.* 2009, *131*, 3198.

[176] Nasalevich, M. A.; Goesten, M. G.; Savenije, T. J.; Kapteijn, F.; Gascon, J. Enhancing optical absorption of metal-organic frameworks for improved visible light photocatalysis. *Chem. Commun.* 2013, *49*, 10575.

[177] Huijser, A.; Suijkerbuijk, B. M. J. M.; Klein Gebbink, R. J. M.; Savenije, T. J.; Siebbeles Efficient Exciton Transport in Layers of Self-Assembled Porphyrin Derivatives. *J. Am. Chem. Soc.* 2008, *130*, 2485.

[178] Boschloo, G.; Hagfeldt, A. Characteristics of the Iodide/Triiodide Redox Mediator in Dye-Sensitized Solar Cells. *Acc. Chem. Res.* 2009, *42*, 1819.

[179] Serpone, N.; Jamieson, M. A. Picosecond spectroscopy of transition metal complexes. *Coord. Chem. Rev.* 1989, *93*, 87.

[180] Najafov, H.; Lee, B.; Zhou, Q.; Feldman, L. C.; Podzorov, V. Observation of long-range exciton diffusion in highly ordered organic semiconductors. *Nat. Mater.* 2010, *9*, 938.

[181] Turrión, M.; Bisquert, J.; Salvador, P. Flatband Potential of F:SnO$_2$ in a TiO$_2$ Dye-Sensitized Solar Cell: An Interference Reflection Study. *J. Phys. Chem. B* 2003, *107*, 9397.

[182] Klein, A.; Körber, C.; Wachau, A.; Säuberlich, F.; Gassenbauer, Y.; Harvey, S. P.; Proffit, D. E.; Mason, T. O. Transparent Conducting Oxides for Photovoltaics: Manipulation of Fermi Level, Work Function and Energy Band Alignment. *Materials* 2010, *3*, 4892.

[183] Rappe, A. K.; Casewit, C. J.; Colwell, K. S.; Goddard, W. A.; Skiff, W. M. UFF, a full periodic table force field for molecular mechanics and molecular dynamics simulations. *J. Am. Chem. Soc.* 1992, *114*, 10024.

[184] Gale Julian, D. In Zeitschrift für Kristallographie - Crystalline Materials 2005; Vol. 220, p 552.

[185] Gale, J. D.; Rohl, A. L. The General Utility Lattice Program (GULP). *Molecular Simulation* 2003, *29*, 291.

[186] Wahiduzzaman, M.; Oliveira, A. F.; Philipsen, P.; Zhechkov, L.; van Lenthe, E.; Witek, H. A.; Heine, T. DFTB Parameters for the Periodic Table: Part 1, Electronic Structure. *J. Chem. Theory Comput.* 2013, *9*, 4006.

[187] Frisch, M.; Trucks, G.; Schlegel, H. B.; Scuseria, G.; Robb, M.; Cheeseman, J.; Scalmani, G.; Barone, V.; Mennucci, B.; Petersson, G. e.; Gaussian, Inc. Wallingford, CT: 2009.

[188] Perdew, J. P.; Burke, K.; Ernzerhof, M. Generalized Gradient Approximation Made Simple. *Phys. Rev. Lett.* 1996, *77*, 3865.

[189] Dovesi, R.; Saunders, V.; Roetti, C.; Orlando, R.; Zicovich-Wilson, C.; Pascale, F.; Civalleri, B.; Doll, K.; Harrison, N.; Bush, I. CRYSTAL09 (CRYSTAL09 user's manual). *University of Torino, Torino* 2009.

[190] Peintinger, M. F.; Oliveira, D. V.; Bredow, T. Consistent Gaussian basis sets of triple-zeta valence with polarization quality for solid-state calculations. *J. Comput. Chem.* 2013, *34*, 451.

[191] Hofmann, P. *Solid state physics: an introduction*; John Wiley & Sons, 2015.

[192] Liu, J.; Zhou, W.; Liu, J.; Howard, I.; Kilibarda, G.; Schlabach, S.; Coupry, D.; Addicoat, M.; Yoneda, S.; Tsutsui, Y.; Sakurai, T.; Seki, S.; Wang, Z.; Lindemann, P.; Redel, E.; Heine, T.; Wöll, C. Photoinduced Charge-Carrier Generation in Epitaxial MOF Thin Films: High Efficiency as a Result of an Indirect Electronic Band Gap? *Angew. Chem. Int. Ed.* 2015, *54*, 7441.

[193] Chen, L.-M.; Hong, Z.; Li, G.; Yang, Y. Recent Progress in Polymer Solar Cells: Manipulation of Polymer:Fullerene Morphology and the Formation of Efficient Inverted Polymer Solar Cells. *Adv. Mater.* 2009, *21*, 1434.

[194] McCarthy, B. D.; Hontz, E. R.; Yost, S. R.; Van Voorhis, T.; Dincă, M. Charge Transfer or J-Coupling? Assignment of an Unexpected Red-Shifted Absorption Band in a Naphthalenediimide-Based Metal-Organic Framework. *J. Phys. Chem. Lett.* 2013, *4*, 453.

[195] Wan, S.; Gándara, F.; Asano, A.; Furukawa, H.; Saeki, A.; Dey, S. K.; Liao, L.; Ambrogio, M. W.; Botros, Y. Y.; Duan, X.; Seki, S.; Stoddart, J. F.; Yaghi, O. M. Covalent Organic Frameworks with High Charge Carrier Mobility. *Chem. Mater.* 2011, *23*, 4094.

[196] Wróbel, D.; Lewandowska, K. Covalent dyads of porphyrin-fullerene and perylene-fullerene for organic photovoltaics: Spectroscopic and photocurrent studies. *Opt. Mater.* 2011, *33*, 1424.

[197] Hayashi, H.; Kira, A.; Umeyama, T.; Matano, Y.; Charoensirithavorn, P.; Sagawa, T.; Yoshikawa, S.; Tkachenko, N. V.; Lemmetyinen, H.; Imahori, H. Effects of Electrode Structure on Photoelectrochemical Properties of ZnO Electrodes Modified with Porphyrin-Fullerene Composite Layers with an Intervening Fullerene Monolayer. *J. Phys. Chem. C* 2009, *113*, 10819.

[198] Łapiński, A.; Graja, A.; Olejniczak, I.; Bogucki, A.; Imahori, H. Supramolecular porphyrin/fullerene interactions studied by spectral methods. *Chem. Phys.* 2004, *305*, 277.

[199] Vail, S. A.; Krawczuk, P. J.; Guldi, D. M.; Palkar, A.; Echegoyen, L.; Tomé, J. P. C.; Fazio, M. A.; Schuster, D. I. Energy and Electron Transfer in Polyacetylene-Linked Zinc-Porphyrin-[60]Fullerene Molecular Wires. *Chem. Eur. J.* 2005, *11*, 3375.

[200] Meilikhov, M.; Yusenko, K.; Esken, D.; Turner, S.; Van Tendeloo, G.; Fischer, R. A. Metals@MOFs - Loading MOFs with Metal Nanoparticles for Hybrid Functions. *Eur. J. Inorg. Chem.* 2010, *2010*, 3701.

[201] Jiang, H.-L.; Feng, D.; Liu, T.-F.; Li, J.-R.; Zhou, H.-C. Pore Surface Engineering with Controlled Loadings of Functional Groups via Click Chemistry in Highly Stable Metal-Organic Frameworks. *J. Am. Chem. Soc.* 2012, *134*, 14690.

[202] Guo, W.; Liu, J.; Weidler, P. G.; Liu, J.; Neumann, T.; Danilov, D.; Wenzel, W.; Feldmann, C.; Wöll, C. Loading of ionic compounds into metal-organic frameworks: a joint theoretical and experimental study for the case of La^{3+}. *Phys. Chem. Chem. Phys.* 2014, *16*, 17918.

[203] Guo, W.; Chen, Z.; Yang, C.; Neumann, T.; Kubel, C.; Wenzel, W.; Welle, A.; Pfleging, W.; Shekhah, O.; Wöll, C.; Redel, E. Bi_2O_3 nanoparticles encapsulated in surface mounted metal-organic framework thin films. *Nanoscale* 2016, *8*, 6468.

[204] Guillerm, V.; Kim, D.; Eubank, J. F.; Luebke, R.; Liu, X.; Adil, K.; Lah, M. S.; Eddaoudi, M. A supermolecular building approach for the design and construction of metal-organic frameworks. *Chem. Soc. Rev.* 2014, *43*, 6141.

[205] Rostovtsev, V. V.; Green, L. G.; Fokin, V. V.; Sharpless, K. B. A Stepwise Huisgen Cycloaddition Process: Copper(I)-Catalyzed Regioselective "Ligation" of Azides and Terminal Alkynes. *Angew. Chem.* 2002, *114*, 2708.

[206] Heinke, L.; Wöll, C. Adsorption and diffusion in thin films of nanoporous metal-organic frameworks: ferrocene in SURMOF $Cu_2(ndc)_2(dabco)$. *Phys. Chem. Chem. Phys.* 2013, *15*, 9295.

[207] Karger, J.; Binder, T.; Chmelik, C.; Hibbe, F.; Krautscheid, H.; Krishna, R.; Weitkamp, J. Microimaging of transient guest profiles to monitor mass transfer in nanoporous materials. *Nat. Mater.* 2014, *13*, 333.

[208] Najafi Nobar, S.; Farooq, S. Experimental and modeling study of adsorption and diffusion of gases in Cu-BTC. *Chem. Eng. Sci.* 2012, *84*, 801.

[209] Li, J.-R.; Kuppler, R. J.; Zhou, H.-C. Selective gas adsorption and separation in metal-organic frameworks. *Chem. Soc. Rev.* 2009, *38*, 1477.

[210] Stallmach, F.; Gröger, S.; Künzel, V.; Kärger, J.; Yaghi, O. M.; Hesse, M.; Müller, U. NMR Studies on the Diffusion of Hydrocarbons on the Metal-Organic Framework Material MOF-5. *Angew. Chem. Int. Ed.* 2006, *45*, 2123.

[211] Wang, C.; Lin, W. Diffusion-Controlled Luminescence Quenching in Metal-Organic Frameworks. *J. Am. Chem. Soc.* 2011, *133*, 4232.

[212] Salles, F.; Jobic, H.; Maurin, G.; Koza, M. M.; Llewellyn, P. L.; Devic, T.; Serre, C.; Ferey, G. Experimental Evidence Supported by Simulations of a Very High H_2 Diffusion in Metal Organic Framework Materials. *Phys. Rev. Lett.* 2008, *100*, 245901.

[213] Kortunov, P. V.; Heinke, L.; Arnold, M.; Nedellec, Y.; Jones, D. J.; Caro, J.; Kärger, J. Intracrystalline Diffusivities and Surface Permeabilities Deduced from Transient Concentration Profiles: Methanol in MOF Manganese Formate. *J. Am. Chem. Soc.* 2007, *129*, 8041.

[214] Chmelik, C.; Kärger, J.; Wiebcke, M.; Caro, J.; van Baten, J. M.; Krishna, R. Adsorption and diffusion of alkanes in CuBTC crystals investigated using infra-red microscopy and molecular simulations. *Microporous Mesoporous Mater.* 2009, *117*, 22.

[215] Monte, M. J. S.; Santos, L. M. N. B. F.; Fulem, M.; Fonseca, J. M. S.; Sousa, C. A. D. New Static Apparatus and Vapor Pressure of Reference Materials: Naphthalene, Benzoic Acid, Benzophenone, and Ferrocene. *J. Chem. Eng. Data* 2006, *51*, 757.

[216] De Fina, K. M.; Ezell, C.; Acree, W. E. Solubility of Ferrocene in Organic Nonelectrolyte Solvents. Comparison of Observed Versus Predicted Values Based Upon Mobile Order Theory. *Phys. Chem. Liq.* 2001, *39*, 699.

[217] Cakici, M.; Gu, Z.-G.; Nieger, M.; Burck, J.; Heinke, L.; Brase, S. Planar-chiral building blocks for metal-organic frameworks. *Chem. Commun.* 2015, *51*, 4796.

[218] Gu, Z.-G.; Grosjean, S.; Brase, S.; Wöll, C.; Heinke, L. Enantioselective adsorption in homochiral metal-organic frameworks: the pore size influence. *Chem. Commun.* 2015, *51*, 8998.

[219] Heinke, L.; Gu, Z.; Wöll, C. The surface barrier phenomenon at the loading of metal-organic frameworks. *Nature Communications* 2014, *5*.

[220] Kärger, J.; Chmelik, C.; Heinke, L.; Valiullin, R. A new view of diffusion in nanoporous materials. *Chem. Ing. Tech.* 2010, *82*, 779.

[221] Chidsey, C. E. D.; Bertozzi, C. R.; Putvinski, T. M.; Mujsce, A. M. Coadsorption of ferrocene-terminated and unsubstituted alkanethiols on gold: electroactive self-assembled monolayers. *J. Am. Chem. Soc.* 1990, *112*, 4301.

[222] Heinke, L.; Kärger, J. Correlating Surface Permeability with Intracrystalline Diffusivity in Nanoporous Solids. *Phys. Rev. Lett.* 2011, *106*, 074501.

[223] Kärger, J. In-depth study of surface resistances in nanoporous materials by microscopic diffusion measurement. *Microporous Mesoporous Mater.* 2014, *189*, 126.

[224] Heinke, L.; Kortunov, P.; Tzoulaki, D.; Kärger, J. Exchange Dynamics at the Interface of Nanoporous Materials with their Surroundings. *Phys. Rev. Lett.* 2007, *99*, 228301.

Publications

1. Liu, J.; **Zhou, W.**; Liu, J.; Fujimori, Y.; Higashino, T:, Imahori, H.; Jiang, X.; Zhao, J:, Sakurai, Y.; Hattori, Y.; Matsuda, W.; Seki, S.; Garlapati, S.; Dasgupta, S.; Redel, E.; Sun, L.; Wöll, C. A new class of epitaxial porphyrin metal-organic framework thin films with extremely high photocarrier generation efficiency: promising materials for all-solid-state solar cell. *Journal of Materials Chemistry A (accepted)*

2. Liu, J.; **Zhou, W.**; Liu, J.; Howard, I.; Kilibarda, G.; Schlabach, S.; Coupry, D.; Addicoat, M.; Yoneda, S.; Tsutsui, Y.; Sakurai, T.; Seki, S.; Wang, Z.; Lindemann, P.; Redel, E.; Heine, T.; Wöll, C. Photoinduced Charge-Carrier Generation in Epitaxial MOF Thin Films: High Efficiency as a Result of an Indirect Electronic Band Gap? *Angewandte Chemie International Edition* **2015**, 54, 7441.

3. **Zhou, W.**; Wöll, C.; Heinke, L. Liquid- and Gas-Phase Diffusion of Ferrocene in Thin Films of Metal-Organic Frameworks. *Materials* **2015**, *8*, 3767.

4. Liu, J.*; **Zhou, W.***; Walheim, S.; Wang, Z.; Lindemann, P.; Heissler, S.; Liu, J.; Weidler, P. G.; Schimmel, T.; Wöll, C.; Redel, E. Electrochromic switching of monolithic Prussian blue thin film devices. *Opt Express* **2015**, 23, 13725. (* *Both authors contributed equally*)

Acknowledgements

First of all, I would like to extend my sincere gratitude to my supervisor, Prof. Dr. Christof Wöll, for offering the opportunity to study abroad, for his support, encouragement and instructive advice during my PhD study. Without his supervision and kind help, I could not finish this thesis. I am deeply grateful of his help in the completion of this thesis.

I would like to thank Prof. Dr. Stefan Bräse for the co-referee in my thesis and appreciate the time he dedicated for reviewing my thesis.

I am sincerely thankful to Dr. Jinxuan Liu who is now working in Dalian University of Technology for his continuously guidance and introduction of experiment during my experiments, especially in the first two years. He paid a lot of efforts in my thesis and I do appreciate him. Grateful acknowledgement is also made to PD Dr. Lars Heinke and Dr. Zhengbang Wang, who gave me continuously guidance and considerable help by means of suggestion, comments and discussion.

I gratefully appreciate Dr. Hartmut Gliemann and Dr. Peter G. Weidler for valuable suggestions, constructive discussions and also constant help in the technical issues and thesis during my period of work. I would also like to thank my other colleagues: Dr. Alexander Welle, Dr. Engelbert Redel, Dr. Manuel Tsotsalas, Peter Krolla-Sidenstein, Stefan Heissler, Dr. Jianxi Liu. Dr. Zhigang Gu, Dr. Wei Guo, Chengwu Yang, Dr. Sophia Schmitt, Dr. Peter Lindemann, Dr. Alexei Nefedov, Dr. Tawheed Mohamed, Dr. Ritesh Haldar, Qi An, Kai Müller, Jonas Wohlgemuth, Dr. Angela Weiss, Stefanie Sellheim-Ret and Astrid Biedermann for their kind help during my study in IFG and I am very appreciative to have opportunity to work together with them.

Thanks to the cooperative groups: Prof. Dr. Stefan Bräse and Prof. Hiroshi Imahori from Kyoto University (Japan) for providing the organic ligands, Prof. Shu Seki from Osaka University (Japan), Dr. Ian Howard from Institute of Microstructure Technology (IMT), Dr. Goran Kilibarda and Dr. Sabine Schlabach from Institute for Applied Materials (IAM), Wenshan Li and Suresh Kumar Garlapati from the Institute of Nanotechnology (INT) for the measurements, Prof. Thomas Heine from Jacobs University Bremen for the supports of theoretical calculations.

I give my heartfelt thanks to my family for their endless love and support throughout my entire life, as well as my friends who always encourage me and accompany with me when I was in depression. You are my spiritual support.